Title
Orientation Dependence of the Anomalous Hall Effect in 3d-Ferromagnets

Author
Roman, Eric Shawn

Publication Date
2010

Peer reviewed|Thesis/dissertation

Orientation Dependence of the Anomalous Hall Effect in 3d-Ferromagnets

by

Eric Shawn Roman

A dissertation submitted in partial satisfaction of the

requirements for the degree of

Doctor of Philosophy

in

Physics

in the

Graduate Division

of the

University of California, Berkeley

Committee in charge:

Professor Ivo Souza, Chair

Professor Yuri Suzuki

Professor Xi Qiu

Fall 2010

Orientation Dependence of the Anomalous Hall Effect in 3d-Ferromagnets

Abstract

Orientation Dependence of the Anomalous Hall Effect in 3d-Ferromagnets

by

Eric Shawn Roman

Doctor of Philosophy in Physics

University of California, Berkeley

Professor Ivo Souza, Chair

This dissertation describes calculations of the magnetization dependence of the intrinsic Hall conductivity in three elemental ferromagnets: iron, cobalt and nickel. We compare our calculations with experimental measurements of these anomalous Hall coefficients, and we show that *ab initio* calculations of the anomalous Hall conductivity from the Karplus-Luttinger theory explain the observed changes in the anomalous Hall coefficients of these metals as the magnetization direction is varied.

To Laura.

Contents

List of Figures

List of Tables

Acknowledgments

I would like to thank my advisor, Ivo Souza, for his guidance. He sets a fine standard as a role model by staying actively involved in research, publishing consistently excellent work, and adhering to high standards.

This dissertation would not have been possible without the support of the Employee Development and Training program at Lawrence Berkeley National Laboratory. Without the patronage of Berkeley Lab, I would not have been able to complete graduate school. I would like to thank Bob Lucas for his advice, especially for encouraging me to enroll in a Ph.D. program. I am especially grateful to Brent Gorda, Kathy Yelick, David Bailey, Erich Strohmaier, and Juan Meza for providing their approval. Paul Hargrove has supported me at each step of my graduate career.

Jonathan Yates, Yuriy Mokrousov, and Miguel Pruneda all provided valuable insight, discussions, and feedback. Anne Takizawa, for all her help over the past several years, from preparing for the preliminary exams, to scheduling the qualifying exam, to helping with filing for the degree, deserves special praise. Guy Tyler encouraged me to pursue my interest in computing, and Carl Krolik stimulated my earliest interests in physics. Yuefan Deng helped me to begin my research career.

My family has helped support and encourage me. Thanks to my parents Hector and Cynthia Roman, my brother Jeremy, and my sister Melanie. I also thank my friends Todd Johnson and Noël Gregorwich.

Parts of this work were supported by NSF Grant No. DMR 0706493. This research used the Lawrencium computational cluster resource provided by Lawrence Berkeley National Laboratory, and resources of the National Energy Research Scientific Computing Center, which are supported by the Office of Science of the U.S. Department of Energy under Contract No. DE-AC02-05CH11231.

Chapter 1

The Hall Effect in Ferromagnets

The Hall effect in normal nonmagnetic metals is proportional only to the internal magnetic field **B**, but in a ferromagnet the Hall effect has an additional part, proportional to the magnetization **M**. The dependence of the Hall field $\mathbf{E}_H$ on the magnetization **M** can result in anisotropy of the Hall effect. In recent years, Karplus and Luttinger's theory of the intrinsic part of the anomalous Hall effect has been used to perform *ab initio* calculations of the Hall conductivity in some materials, with fair quantitative agreement with experiments. In previous work, the variation of the intrinsic Hall conductivity with the direction of the magnetization has not been considered.

The study of the magnetization dependence is interesting for several reasons. A recent review of the anomalous Hall effect expresses a need for further study of the microscopic mechanisms of the anomalous Hall effect [1]. The intrinsic Karplus-Luttinger mechanism is one of the various contributions to the anomalous Hall conductivity. Calculations of this contribution from first principles, combined with measurements of the Hall coefficients, allow us to estimate the size of the remaining side-jump and skew scattering contributions. Interest also arises from more fundamental considerations, since the intrinsic conductivity is a macroscopic manifestation of a geometric property, the Berry curvature, of the electron band structure. The geometric effects are sensitive to the fine details of the electronic structure. Early theoretical efforts were hampered due to the lack of sufficient accuracy in the wave functions. The accurate Hamiltonians available in a first principles calculation allows us to gain insight as to how the anomalous Hall effects behave in realistic systems, and serve as a complement to model Hamiltonians using simplified descriptions of these materials. A final goal of this work is to serve as a starting point for future studies of the magnetization-dependent anomalous Hall conductivity. The magnetic field orientation is one of the few parameters that can be easily adjusted by both experiments and in theoretical calculations, and this allows detailed comparisons to be made between *ab initio* theory and experiments. Therefore, this work is expected to be of interest to future theorists calculating the side-jump and skew scattering contributions, and also to experimentalists studying anisotropic transport.

This dissertation contains calculations of the intrinsic Hall conductivity in the anisotropic

case. We calculate the anisotropy in the intrinsic Hall conductivity for three elemental ferromagnets: iron, cobalt and nickel. The anisotropic Hall effect in these materials has been studied experimentally, so they are good candidates for a theoretical study. Each material shows different aspects of anisotropy. Hexagonal cobalt, because it is a uniaxial crystal, shows strong first-order anisotropy in the anomalous Hall conductivity. In cubic crystals, anisotropy appears at third-order in the magnetization, and this is seen clearly in bcc iron, where the anomalous Hall effect is nearly isotropic, but not in fcc nickel, where the anisotropy is significant. We compare our calculations with experimental measurements of these anomalous Hall coefficients. We show that *ab initio* calculations of the anomalous Hall conductivity from the Karplus-Luttinger theory explain the observed changes in the anomalous Hall coefficients of these three transition metals when the magnetization direction is varied.

The dissertation is organized as follows. In Chapter 1 we discuss the history and phenomenology of the anomalous Hall effect (AHE), and describe how to calculate the anomalous Hall coefficient R_s in a conventional *ab initio* framework. Chapter 2 describes the anisotropy of the anomalous Hall effect in cobalt crystals, showing how first order anisotropy manifests itself in hcp cobalt. Chapter 3 describes the AHE in bcc iron, where it is shown that the theoretical anisotropy is small, explaining why anisotropy of the AHC has never been observed in bcc Fe. Chapter 4 describes the AHE in Ni, where the intrinsic part of the AHE accounts for much, but not all, of the variations measured experimentally. We show that in nickel about half of the discrepancy between previous calculations and measurements of the AHE arise from a theoretical error in decribing the exchange splitting of the *d*-bands. We argue that the remainder of the discrepancy between the AHE predicted by *ab initio* theory and that observed experimentally is due to impurity scattering terms which are out of the scope of the Karplus-Luttinger theory. Chapter 5 summarizes our conclusions and suggests directions for future work.

1.1 Background

In 1879, Hall showed that a nonmagnetic wire carrying a current in a magnetic field induces a voltage transverse to that field [2]. This phenomenon is known as the (ordinary) *Hall effect*. Hall subsequently found that in ferromagnets, the effect is almost an order of magnitude larger. The effect in ferromagnets later became known as the *anomalous Hall effect* (or extraordinary Hall effect) [3]. The origin of the ordinary Hall effect has been known to be a consequence of the Lorentz force, but the origin of the anomalous Hall effect has been controversial.

A theory of the anomalous Hall effect (AHE) was put forth by Karplus and Luttinger [4], who showed that a Hall current perpendicular to the electric field and odd under magnetization reversal is established in a ferromagnetic crystal as a result of the spin-orbit interaction (SOI). The relationship between the AHE and the SOI became understood, but a long debate ensued on whether the relevant SOI is associated with the crystalline po-

tential (intrinsic) or with impurity atoms (extrinsic). The asymmetric impurity scattering of the spin-polarized charge carriers (skew-scattering) leads to a linear dependence of the (transverse) anomalous Hall resistivity $\rho_H = E_y/j_x$ on the longitudinal resistivity ρ_{xx}; an additional scattering process, side-jump, yields the same scaling $\rho_H \propto \rho_{xx}^2$ as the intrinsic Karplus-Luttinger mechanism. For a review see Ref. [1].

Unlike the extrinsic contributions, which depend on the details of the impurity potential, the Karplus-Luttinger anomalous Hall conductivity (AHC) can be evaluated from the crystal band structure as a Brillouin zone integral [5]:

$$\sigma_{ij}^a = -\frac{e^2}{\hbar}\int_{\mathrm{BZ}} \frac{d^3k}{(2\pi)^3} \sum_n f_{n\mathbf{k}}\Omega_{n\mathbf{k},ij}, \tag{1.1}$$

where $f_{n\mathbf{k}}$ is the Fermi-Dirac distribution function and $\Omega_{n,ij}(\mathbf{k})$ is the Berry curvature tensor (defined in section 1.4.1). of each cell-periodic spinor Bloch state $|u_{n\mathbf{k}}\rangle$ First-principles calculations for Fe, Co, Ni [5, 6, 7], $SrRuO_3$ [8] and Mn_5Ge_3[9] have consistently found good agreement with room-temperature experiments, establishing the importance of the intrinsic mechanism.

Recent experiments have focused on isolating the different contributions to the AHE [10, 9, 11]. Skew-scattering can be separated from the other two terms by fitting the measured anomalous Hall resistivity to the form

$$\rho_H = a\rho_{xx} + b\rho_{xx}^2, \tag{1.2}$$

where $b = \sigma_{xy}^a + b^{\mathrm{SJ}}$. The coefficients a (skew-scattering) and b (intrinsic plus side-jump) can be read off a plot of ρ_H/ρ_{xx} versus ρ_{xx}, where ρ_{xx} is varied through doping or temperature changes. Recent experimental work by Tian has improved on the scaling relationship (1.2) [11]. Tian varies the diagonal resistivity independently of the temperature and found the relationship $\rho_H = \alpha\rho_{xx0} + \beta\rho_{xx0}^2 + b\rho_{xx}^2$. Recent theoretical work has more rigorously related the microscopic scattering mechanisms to the conductivity to different orders in the scattering lifetime, thus providing a better understanding of the coefficients a and b in (1.2) [1, 12].

1.2 The Anomalous Hall Effect

In a magnetic field **H** and magnetization **M** the electric field **E** is of a conducting material is related to the current density **J** by a generalized Ohm's law [13]

$$E_i = \rho_{ij}(\mathbf{H},\mathbf{M})J_j. \tag{1.3}$$

The antisymmetric part of ρ defines the *Hall resistivity*. In a crystal with cubic symmetry, taking $\mathbf{J} = J_x\hat{\mathbf{x}}$, and $\mathbf{B} = B\hat{\mathbf{z}}$, eq. (1.4) reduces to

$$E_y = \rho_H J_x, \tag{1.4}$$

where ρ_H is known as the *Hall resistivity*.

The Hall resistivity ρ_H of a ferromagnetic material follows an empirical relationship [13]

$$\rho_H = R_0\mu_0 H + R_1\mu_0 M \tag{1.5}$$

in SI units, where H is the macroscopic magnetic field (in A/m) inside the sample, M is the sample magnetization (A/m), R_0 is the *ordinary Hall coefficient*, and R_1 is the *extraordinary Hall coefficient* (R_0 and R_1 in Ω m/T). Using the constitutive relationship $B = \mu_0(H+M)$ (1.5) can be written

$$\rho_H = R_0 B + R_s\mu_0 M \tag{1.6}$$

where R_s is the *anomalous Hall coefficient* given by

$$R_s = R_1 - R_0, \tag{1.7}$$

and B is the magnetic flux density inside the material.

The behavior of ρ_H as B is increased is shown in figure 1.2. If B is large ($B \gg \mu_0 M_s$), the magnetization approaches the saturation limit $\mu_0 M_s$, and from (1.6) we find:

$$\rho_H = R_0 B + R_s\mu_0 M_s \quad (B \gg \mu_0 M_s). \tag{1.8}$$

This equation describes a line of slope R_0 and intercept $R_s M_s$, and provides us with a way to extract the anomalous Hall coefficient from a measurement of ρ_H in large fields. In the low B limit ($B \ll \mu_0 M_s$), using the relative magnetic permeability μ_r, then we may write $\mu_0 M = (1 - 1/\mu_r)B$, so that $\rho_H = [R_0 + (1-1/\mu_r)R_s]B$. In a ferromagnet, μ_r is large in small fields, so that

$$\rho_H = (R_0 + R_s)B \quad (B \ll \mu_0 M_s). \tag{1.9}$$

We see that for small fields, we have a line of slope $R_0 + R_s$.

1.3 Phenomenological description

Before discussing the origins of the anomalous Hall conductivity, we review the phenomenology [14, 15]. Electrical conduction in ferromagnets is described by a magnetization-dependent conductivity tensor:

$$J_i = \sigma_{ij}(\mathbf{H}, \mathbf{M})E_j. \tag{1.10}$$

We assume that the conductivity tensor components σ_{ij} can be approximated by a polynomial in M_i

$$\sigma_{ij}(\mathbf{M}) = \sigma_{ij}^{(0)} + \sigma_{ijp}^{(1)}M_p + \sigma_{ijpq}^{(2)}M_p M_q + \ldots, \tag{1.11}$$

We have ignored the terms in $\mathbf{H}$, since these describe the orientation dependence of the ordinary Hall conductivity. In 1.4.2, we discuss the justification for using this expansion in more detail. When we speak of nth-order anisotropy, we mean that the expansion in (1.11) over M_p has been carried out to n-th order.

Figure 1.1: The Hall resistivity ρ_H in a ferromagnet is not linear in the magnetic field strength B, but also depends on the magnetization M. For small fields ($B \ll \mu_0 M_s$), $\rho_H \approx R_0 + R_s B$. In large fields ($B \gg \mu_0 M_s$) the magnetization saturates and $\rho_H \approx R_s \mu_0 M_s + R_0 B$.

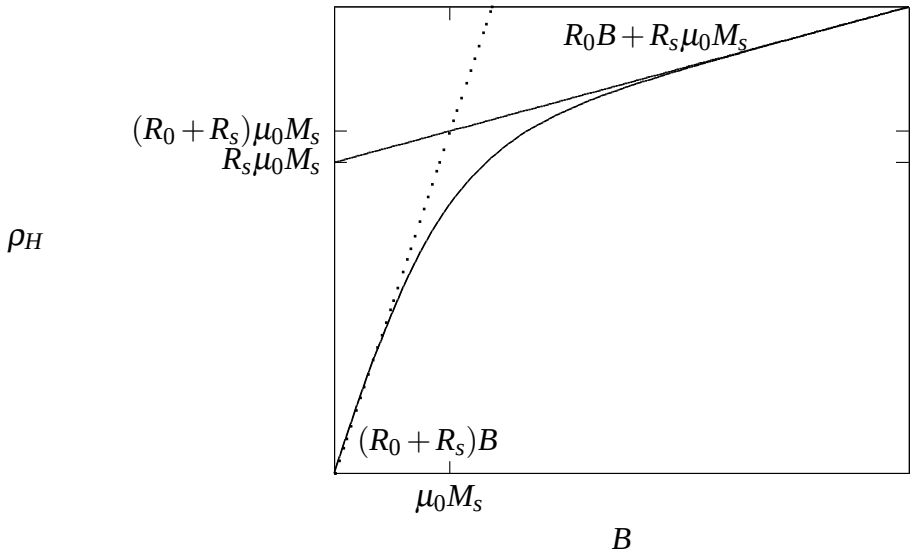

The polynomial expansion in M_p implies that the $\sigma_{ijp^1\ldots p^n}$ are symmetric in all but the first two indices, so

$$\sigma_{ij\ldots p^m\ldots p^n\ldots} = \sigma_{ij\ldots p^n\ldots p^m\ldots}. \tag{1.12}$$

Eq. (1.12) is the first of three symmetry relations that we use to simplify the form of the conductivity expansion.

The second symmetry condition on the form of the conductivity is a consequence of microscopic reversibility, resulting in the Onsager relation

$$\sigma_{ij}(\mathbf{M}) = \sigma_{ji}(-\mathbf{M}). \tag{1.13}$$

This relationship (1.13) implies that the symmetric and antisymmetric parts of σ_{ij}

$$\sigma^s_{ij}(\mathbf{M}) = \tfrac{1}{2}\big(\sigma_{ij}(\mathbf{M}) + \sigma_{ji}(\mathbf{M})\big) = \tfrac{1}{2}\big(\sigma_{ji}(-\mathbf{M}) + \sigma_{ij}(-\mathbf{M})\big) = \sigma^s_{ij}(-\mathbf{M}) \tag{1.14}$$

$$\sigma^a_{ij}(\mathbf{M}) = \tfrac{1}{2}\big(\sigma_{ij}(\mathbf{M}) - \sigma_{ji}(\mathbf{M})\big) = \tfrac{1}{2}\big(\sigma_{ji}(-\mathbf{M}) - \sigma_{ij}(-\mathbf{M})\big) = -\sigma^a_{ij}(-\mathbf{M}) \tag{1.15}$$

are respectively even and odd functions of the magnetization $\mathbf{M}$. Eqs. (1.14) and (1.15) imply also that the current density $\mathbf{J}$ is also comprised of both an even *Ohmic current* $\mathbf{J}^s$ and an odd *Hall current* $\mathbf{J}^a$. The Hall current reads

$$\mathbf{J}^a = \mathbf{E} \times \sigma^a, \tag{1.16}$$

where $\sigma^a_k = (1/2)\varepsilon_{ijk}\sigma^a_{ij}$. $\mathbf{J}^a$ is perpendicular to $\mathbf{E}$ but not necessarily to $\mathbf{M}$, since σ^a and $\mathbf{M}$ may not be collinear. Since $\mathbf{J}\cdot\mathbf{E} = 0$, the antisymmetric Hall current is dissipationless,

and Joule heating is associated only with the even terms $\mathbf{J}^s$. Even in single crystals, $\sigma^a \parallel \mathbf{M}$ only when $\mathbf{M}$ points along certain high-symmetry directions.

The microscopic contribution to the Hall conductivity is antisymmetric (odd), and the experiments measuring the Hall coefficient R_s all measure the odd part of the voltage by reversing the magnetic field. We will not discuss the symmetric part of either the resistivity or the conductivity in this dissertation. Unless otherwise stated, ρ or σ refer to the antisymmetric part.

The third symmetry condition applying to the conductivity arise from the symmetry of the crystal. The conductivity tensor remains invariant under the action of the crystal's point group [16, 17]. The action of the point group on σ is considered in detail in appendix B. If R is a representation of a point group symmetry on σ, then invariance under R means that

$$R\sigma_{ij}(\mathbf{M}) = \det R\sigma_{ij}(\mathbf{M}). \tag{1.17}$$

The direct inspection method may be used to find an invariant form of the conductivity polynomial, unless the point group contains a 3-fold rotation axis [17]. This method provides a practical way to reduce the polynomial expansion to a manageable form. We have found it necessary to expand σ to fifth order in the magnetization to describe the conductivity of nickel, requiring us to calculate the symmetries of a seventh order tensor.

1.3.1 Symmetry and Anisotropy

By introducing the direction cosines α_i and unit vectors $\mathbf{e}_i$, we express $\mathbf{M}$ in components $M_i = M\alpha_i\mathbf{e}_i$. The expansion coefficients may then be written $a_{ijp^1\ldots p^n} = (1/M_n)\sigma_{ijp^1\ldots p^n}$ and we can separate isolate the angular dependence in (1.11):

$$\sigma_{ij}(\mathbf{M}) = a_{ij}^{(0)} + a_{ijp}^{(1)}\alpha_p + a_{ijpq}^{(2)}\alpha_p\alpha_q + \ldots. \tag{1.18}$$

We call the Hall effect in a material *isotropic* if, with $\hat{\alpha}$ a unit vector in the $\mathbf{M}$ direction, the Hall conductivity has the form

$$\sigma_{ij}(\mathbf{M}) = \sigma\varepsilon_{ijk}\alpha_k. \tag{1.19}$$

In components, (1.19) reads

$$a_{123} = a_{231} = a_{312} \quad \text{and} \tag{1.20}$$

$$a_{ij\ldots} = 0 \quad \text{otherwise.} \tag{1.21}$$

When the material is isotropic, (1.16) becomes $\mathbf{J} = (\sigma/M)\mathbf{E}\times\mathbf{M}$. We define *anisotropy* in the Hall conductivity as any deviation from isotropy. Using the symmetry conditions (1.12), (1.13), and (1.17) for a cubic crystal, $a_{123} = a_{231} = a_{312}$. Therefore, to first order in M, a cubic crystal is isotropic, but to third order in M, cubic crystals can show an anisotropic Hall conductivity. In a tetragonal or a hexagonal system, symmetry relations state $a_{231} = a_{312}$, so anisotropy can appear to first order in M in these crystals.

The anisotropy of the Hall effect may also be expressed in terms of spherical harmonics. The spherical harmonic form of (1.18) is desirable because we calculate the $\sigma_{ij}(\mathbf{M})$ appearing on the left hand side of (1.18) at constant $|\mathbf{M}|$. The α_i are related by $\alpha_1^2+\alpha_2^2+\alpha_3^2=1$, implying that the polynomials in α_i appearing in (1.18) are not linearly independent over the sphere at constant $|\mathbf{M}|$. This linear dependence implies that the $a_{ij\ldots}^{(n)}$ cannot be determined from $\sigma(\mathbf{M})$ if $|\mathbf{M}|$ is held constant. We need linearly independent polynomials defined over a sphere $|\mathbf{M}|=$ constant to describe the anisotropy in $\sigma_{\mathbf{M}}$.

The spherical harmonics Y_l^m span the set of l-th order polynomials on a sphere. We can expand $\sigma_{ij}(\theta,\phi)$ in terms of the Y_l^m

$$\sigma_{ij}(\theta,\phi)=\sum_{l=0}^{\infty}\sum_{m=-l}^{l}a_l^m Y_l^m(\theta,\phi), \tag{1.22}$$

where

$$a_l^m=\int_0^{2\pi}\int_0^{\pi}Y_l^m(\theta,\phi)\,\sigma_{ij}(\theta,\phi)^*\sin\theta\,d\theta\,d\phi. \tag{1.23}$$

and θ and ϕ are the usual spherical coordinates. With σ_{ij} real, these relations may be written in terms of real spherical harmonics C_l^m and S_l^m, defined by

$$C_l^m(\theta,\psi)=\frac{1}{\sqrt{2}}(Y_l^{-m}+(-1)^m Y_l^m)=(-1)^m\sqrt{2}\ \mathrm{Re}\ Y_l^m \tag{1.24}$$

$$S_l^m(\theta,\psi)=\frac{i}{\sqrt{2}}(Y_l^{-m}-(-1)^m Y_l^m)=(-1)^m\sqrt{2}\ \mathrm{Im}\ Y_l^m. \tag{1.25}$$

Then (1.22) becomes

$$\sigma_{ij}(\theta,\psi)=\sum_{l=0}^{\infty}\sum_{m=0}^{l}\left[A_l^m C_l^m(\theta,\psi)+B_l^m S_l^m(\theta,\psi)\right], \tag{1.26}$$

where the coefficients A_l^m and B_l^m are related to the a_l^m by

$$a_l^0 = \sqrt{2}A_l^0 \tag{1.27}$$

$$a_l^m = \frac{(-1)^m}{\sqrt{2}}\left[A_l^m-iB_l^m\right] \tag{1.28}$$

$$a_l^{-m} = \frac{1}{\sqrt{2}}\left[A_l^m+iB_l^m\right], \tag{1.29}$$

and the coefficients A_l^m and B_l^m are real since $\sigma_{ij}(\theta,\phi)$ is real.

The C_l^m and S_l^m retain the orthonormality of the Y_l^m. Orthogonality is a convenient property for the discussion of the coefficients A_l^m, as it eliminates the covariance between terms of different orders in l. This orthogonality guarantees that a least squares values of the coefficients A_l^m at one order of l remain constant as we increase the order of the expansion [18].

The coefficients A_l^m of (1.22) feature prominently in the subsequent discussion of the anisotropy in the Hall conductivity. Since the B_l^m can be expressed in terms of the A_l^m for the systems studied here, there is little to gain by considering them separately. In this work, we find the parameters A_l^m using a least squares fit of $\sigma_{ij}(\theta,\phi)$ over a suitably defined grid over θ and ϕ. The details are given in the subsequent chapters.

The A_l^m, like their Cartesian counterparts the $a_{ij\ldots}^{(n)}$ are related by the symmetry conditions (1.12), (1.13), and (1.17). The relations between the A_l^m and the $a_{ij\ldots}^{(n)}$ can be derived by first constructing a polynomial expansion in Cartesian coordinates with the expected symmetries, and then transforming this polynomial into spherical harmonics using (1.23). These relationships are described in detail in appendix B. We have derived expressions for $\sigma_{ij}(\theta,\phi)$ up to fifth order ($l=5$) in α to describe the conductivity of cubic systems.

As an example, consider an isotropic system. From (1.20), the σ_{ij} in an isotropic system are given by

$$\sigma_{23} = a_{123}\alpha_1 \tag{1.30}$$
$$\sigma_{31} = a_{123}\alpha_2 \tag{1.31}$$
$$\sigma_{12} = a_{123}\alpha_3. \tag{1.32}$$

From the definitions of the real spherical harmonics, we have $C_1^1 = \sqrt{3/(4\pi)}\alpha_1$, $S_1^1 = \sqrt{3/(4\pi)}\alpha_2$, and $C_1^0 = \sqrt{3/(2\pi)}\alpha_3$. Substituting the isotropy expression (1.20) in terms of A_l^m, we find

$$\sigma_{23} = A_1^1 C_1^1(\theta,\phi) \tag{1.33}$$
$$\sigma_{31} = B_1^1 S_1^1(\theta,\phi) \tag{1.34}$$
$$\sigma_{12} = C_1^0 C_1^0(\theta,\phi), \tag{1.35}$$

with

$$A_1^1 = B_1^1 = \sqrt{\frac{4}{3\pi}}a_{123} \tag{1.36}$$

$$A_1^0 = \sqrt{\frac{2}{3\pi}}a_{123} = (\sqrt{2}/2)A_1^0. \tag{1.37}$$

In hcp crystals, the orientation dependence is given to third order by the expansion by (see Appendix B)

$$\sigma_{23} = A_1^1 C_1^1(\theta,\phi) + A_3^1 C_3^1(\theta,\phi) \tag{1.38}$$
$$\sigma_{31} = A_1^1 S_1^1(\theta,\phi) + A_3^1 S_3^1(\theta,\phi) \tag{1.39}$$
$$\sigma_{12} = A_1^1 C_1^0(\theta,\phi) + A_3^0 C_3^0(\theta,\phi), \tag{1.40}$$

where $C_{lm}(\theta,\phi)$ and $S_{lm}(\theta,\phi)$ are real spherical harmonics. Because σ_{12} is independent of ϕ, while σ_{23} and σ_{31} have respectively cosine and sine dependences, σ^a and $\mathbf{M}$ share the same azimuthal angle, and their polar-angle mismatch is independent of ϕ.

1.3.2 Experimental Geometry of the Anomalous Hall Effect

When discussing the isotropic Hall effect, it is conventional to use coordinates where the coordinate axes are placed along orthogonal directions defined by the primary current, the direction of voltage measurement, and the magnetic field. For the anisotropic Hall effect, we can choose only two of these three directions to lie on the coordinate axes. We define the x-axis as the primary current direction. In experiments where the Hall voltage is fixed, and measured independently of the magnetic field, it is convenient to define the y-axis as the direction along which the voltage is measured. In experiments where the voltage measurement is rotated with the magnetic field, it is convenient to define the y'-axis as the normal to the x-axis and $\mathbf{B}$. In our *ab initio* calculations, the magnetic field direction is varied directly, so the second convention is also useful theoretically.

The Hall effect, being described by an antisymmetric tensor, may also be expressed by a Hall resistivity (pseudo)-vector $\mathbf{A}$, defined by $\rho_{ij} = \varepsilon_{ijk}\mathbf{A}_k$. This vector $\mathbf{A}$ is used by several authors to discuss anisotropy [19, 15]. This vector $\mathbf{A}$ describes the Hall resistivity by

$$\mathbf{E} = \mathbf{J} \times \mathbf{A}. \tag{1.41}$$

In this section, we relate $\mathbf{A}$ the usual Hall resistivity ρ_H, in both coordinate systems.

We introduce a laboratory coordinate system, as shown in figure 1.2. The primary current $\mathbf{J}$ is fixed in the x-direction, the Hall voltage is measured in the y-direction, and the z-direction is perpendicular to both x and y. From (1.41), the induced electric field always lies in the yz-plane, perpendicular to $\mathbf{J}$, even if the material is anisotropic. The Hall resistivity ρ_H, defined by

$$\rho_H = (1/J)\mathbf{E} \cdot \hat{\mathbf{y}} = (1/J)\mathbf{J} \times \mathbf{A} \cdot \hat{\mathbf{y}} = -\hat{\mathbf{z}} \cdot \mathbf{A}, \tag{1.42}$$

measures only part of the total Hall field $\mathbf{E}$, since $\mathbf{E}$ may have a component along $\hat{\mathbf{z}}$.

In the alternative $y'z'$ system, we choose y' and z' as shown in figure 1.3. In this $y'z'$ system, $\hat{\mathbf{y}}' = (\mathbf{B} \times \hat{\mathbf{x}})/B$ is a unit vector in the yz-plane, and $\hat{\mathbf{z}}' = \hat{\mathbf{x}} \times \hat{\mathbf{y}}'$ completes the triad. The unit vector $\hat{\mathbf{z}}'$ is the projection of $\mathbf{B}$ perpendicular to the current $\mathbf{J} = J\hat{\mathbf{x}}$, so $\hat{\mathbf{z}}'$ lies along $B_y\hat{\mathbf{y}} + B_z\hat{\mathbf{z}}$. We may then write $\mathbf{B} = B_{z'}\hat{\mathbf{z}}' + B_x\hat{\mathbf{x}}$. Expressing $\mathbf{E}$ in terms of $\hat{\mathbf{y}}'$ and $\hat{\mathbf{z}}'$, we have:

$$\mathbf{E} = J_x A_{z'} \hat{\mathbf{y}}' + J_x A_{y'} \hat{\mathbf{z}}'. \tag{1.43}$$

The Hall field $\mathbf{E}$ remains in the $y'z'$-plane, orthogonal to $\mathbf{J}$.

When the Hall resistivity is isotropic, $\mathbf{A}$ is parallel to $\mathbf{B}$ for all directions of $\mathbf{B}$, or $\mathbf{E} = \rho_H \mathbf{J} \times \mathbf{B}$. In the primed coordinates, $\mathbf{E} = \rho_H J_x B_\rho \hat{\mathbf{y}}'$, so that $E_x = E_{z'} = 0$. The induced Hall field $\mathbf{E}$ lies entirely along $\hat{\mathbf{y}}'$, and $E_{y'} = R_H B_{z'} J$. In terms of $\mathbf{A}$, we see that, for an isotropic material

$$A_{z'} = R_H B_{z'} \tag{1.44}$$

$$A_{y'} = 0. \tag{1.45}$$

Figure 1.2: Laboratory coordinate system for anisotropy measurements. The x-direction is defined to be the direction of the primary current **J**. The direction of voltage measurement, perpendicular to **J**, defines the y-direction. A third direction $\hat{\mathbf{z}} = \hat{\mathbf{x}} \times \hat{\mathbf{y}}$ completes the triad.

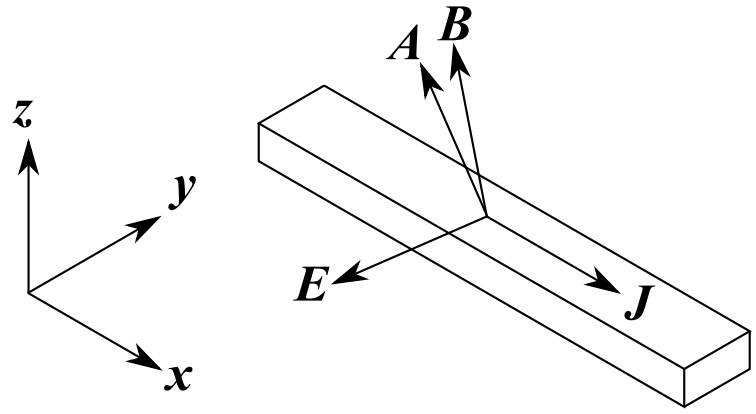

Anisotropy in the resistivity has two chief consequences. First, a second component of the Hall resistivity $A_{y'}$ appears, perpendicular both to **J** and to the usual Hall field $\mathbf{J} \times \mathbf{B}$. Second, $A_{z'}$ can depend on each component of **B**. If we measured the Hall voltage along y' in figure 1.3, the Hall resistivity could change in magnitude as a function of **B**. With this observation, we see that we can quantify the anisotropy of the Hall effect using $A_{z'}$ and $A_{y'}$. The deviation of $A_{y'}$ from 0, and the deviation of $A_{z'}$ from its average are independent measures of the Hall effect anisotropy.

In general, **E** in an anisotropic material has components that are both perpendicular (along $\hat{\mathbf{y}}'$) and parallel (along $\hat{\mathbf{z}}'$) to the magnetic field. The component $E_{y'}$ is no longer independent of the direction of **B**, but can change as **B** is rotated. The component $E_{z'}$ is no longer zero, and implies the existence of a nonzero voltage measured along the direction normal to **J** and along **B**.

1.3.3 The Intrinsic Conductivity and the Hall Coefficient

To compare our calculations of the Hall conductivity σ to the Hall coefficient R_s, we must invert the conductivity tensor, find the corresponding antisymmetric components of the resistivity tensor $\rho_{ij}(\mathbf{M})$, and calculate the resulting Hall field **E** in the laboratory coordinate system. We use the following expression for the conductivity, where the subscripts refer to the crystal coordinate system.

$$\sigma(\mathbf{M}) = \begin{pmatrix} 1/\rho_{11} & \sigma_{12}(\mathbf{M}) & -\sigma_{31}(\mathbf{M}) \\ -\sigma_{12}(\mathbf{M}) & 1/\rho_{22} & \sigma_{23}(\mathbf{M}) \\ \sigma_{31}(\mathbf{M}) & -\sigma_{23}(\mathbf{M}) & 1/\rho_{33} \end{pmatrix} \tag{1.46}$$

No attempt has been made to compensate for other magnetoresistive effects in the estimates of R_s. Published experimental values have been used for the diagonal resistivity ρ_{ii} and for the saturation magnetization M_s, since these quantities are difficult to evaluate from first

Figure 1.3: Alternative $y'z'$-coordinates constructed by placing the z-axis along the magnetic field **B**. These coordinates are convenient theoretically, since the direction of **B** is known. The dotted components shown below vanish if the Hall effect is isotropic.

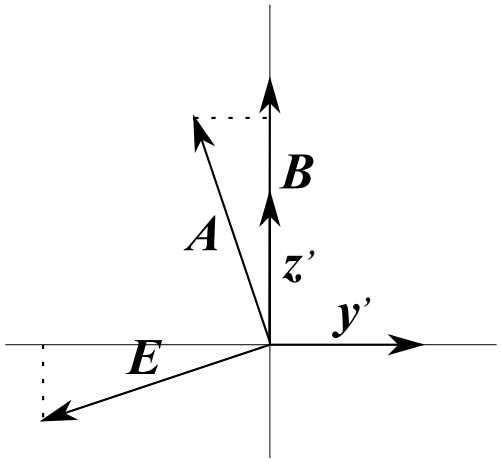

principles. In the chapters that follow, we present first the direct calculations of σ, and convert to R_s when comparing with measurements. For an example, see table 3.4.

The symmetry relationships discussed above for the conductivity σ also apply to the Hall resistivity ρ_H. The permutation symmetry (1.12), Onsager relations (1.13), and point group symmetry (1.17) have exactly the same form if σ is replaced with ρ, and therefore the tensors obey the same relationships. For example, the resistivity tensor may be broken into a symmetric and antisymmetric parts, and by analagy with (1.20) we can define an isotropic Hall resistivity $\rho_{ij}(\mathbf{M}) = \varepsilon_{ijk}\rho_H\alpha_k$, in analogy with (1.19).

1.4 Microscopic Contributions to the Anomalous Hall Effect

There are three main contributions to the anomalous Hall conductivity in ferromagnets. Karplus and Luttinger showed the existence of a scattering-independent *intrinsic mechanism*. Later, Smit found a second mechanism for the anomalous Hall conductivity, the *skew scattering mechanism*, caused by scattering in the presence of spin-orbit coupling. In 1970, Berger found an additional contribution to the anomalous Hall conductivity, the *side-jump mechanism*, arising from the displacement of the center of a wave packet [20]. Smit argued that the intrinsic contribution vanishes, and controversy continued as to which mechanism caused the anomalous Hall effect [21, 22].

The intrinsic and side-jump mechanisms each predict a conductivity that is independent of the impurity concentration. Consequently, for both mechanisms, $R_s \propto \rho^2$, where ρ is the diagonal resistivity. On the other hand, the skew scattering mechanism predicts that $R_s \propto \rho$. Early experiments tried to distinguish these mechanisms by varying the diagonal resistivity,

either with temperature or with impurity concentration, to determine the exponent in the relation $R_s = a\rho^b$. Early log-log plots of R_s versus ρ show that the dependence $R_s \propto \rho^{1.94}$ for Fe and $R_s \propto \rho^{1.42}$ for Ni [4]. These findings show that the intrinsic and side-jump mechanisms dominate for iron, but that in nickel the skew scattering mechanism is also important.

$$R_s = a_{skew}\rho_{xx} + (\sigma_{side-jump} + \sigma_{intrinsic})\rho_{xx}^2 \tag{1.47}$$

When the sample is highly conductive, ρ is small, and the skew scattering dominates the anomalous Hall effect. At higher temperatures, when ρ is large, it is the side-jump and intrinsic scattering terms that dominate. This is seen clearly in nickel. Volkenshtein measured the anomalous Hall conductivity for $T < 100$ K, and found that $R_s \propto \rho$ at these temperatures, but measurements of R_s in nickel at $T > 300$ K show that $R_S \propto \rho^2$ for sufficiently high temperatures [23, 24]. The impurity (side-jump and skew scattering) terms are difficult to calculate, but the intrinsic conductivity can be calculated from first principles.

1.4.1 Origin of the Intrinsic Hall Conductivity

The ordinary Hall coefficient can be understood from the equations of motion for a Bloch electron in a solid [25]:

$$\hbar\dot{\mathbf{k}} = -e\mathbf{E}(\mathbf{r}) - e\dot{\mathbf{r}} \times \mathbf{B}(\mathbf{r}) \tag{1.48}$$

$$\hbar\dot{\mathbf{r}} = \frac{\partial E_n(\mathbf{k})}{\partial \mathbf{k}}. \tag{1.49}$$

Strictly speaking, (1.49) is valid only in crystals with both time-reversal and inversion symmetry. The full form of (1.49) contains an additional term [26, 27], so that the complete semiclassical equations of motion for a Bloch electron are

$$\hbar\dot{\mathbf{k}} = -e\mathbf{E}(\mathbf{r}) - e\dot{\mathbf{r}} \times \mathbf{B}(\mathbf{r}) \tag{1.50}$$

$$\hbar\dot{\mathbf{r}} = \frac{\partial E_n(\mathbf{k})}{\partial \mathbf{k}} - \hbar\dot{\mathbf{k}} \times \mathbf{b}_n(\mathbf{k}), \tag{1.51}$$

where

$$\mathbf{b}_n(\mathbf{k}) = \nabla \times \langle u_{n\mathbf{k}} | i\nabla | u_{n\mathbf{k}} \rangle \tag{1.52}$$

and the $|u_{n\mathbf{k}}\rangle$ are the periodic parts of the wave functions

$$|\psi_{n\mathbf{k}}\rangle = e^{i\mathbf{k}\cdot\mathbf{r}} |u_{n\mathbf{k}}\rangle. \tag{1.53}$$

The quantity $\mathbf{b}_n(\mathbf{k})$ is a vector identified with the antisymmetric part of the curvature tensor $\Omega_{n,ij}(\mathbf{k})$, where the p-th component is given by $b_{n,p}(\mathbf{k}) = \varepsilon_{pqr}\Omega_{qr}(\mathbf{k})$.

The group velocity $\dot{\mathbf{r}}$ gains a contribution from the term $-\hbar\dot{\mathbf{k}} \times \mathbf{b}_n(\mathbf{k})$. This contribution is known as the *anomalous velocity* from its relationship to the anomalous Hall effect.

When $\mathbf{b}_n = 0$, eqs. (1.50) and (1.51) reduce to their usual forms (1.48) and (1.49). The similarity between the anomalous velocity term $\hbar\dot{\mathbf{k}} \times \mathbf{b}_n(\mathbf{k})$ appearing in (1.50) and the Lorentz term $e\dot{\mathbf{r}} \times \mathbf{B}(\mathbf{r})$ appearing in (1.51) has motivated many authors to describe $\mathbf{b}_n$ as a magnetic field acting in $\mathbf{k}$-space. The anomalous Hall effect follows as a direct result of adding the anomalous velocity to the semiclassical Boltzmann theory of transport in a metal. The off-diagonal components of the conductivity tensor include a contribution from the anomalous velocity given by

$$\sigma_{pq} = -\frac{e^2}{\hbar} \int_{\mathrm{BZ}} \frac{d^3k}{(2\pi)^3} \sum_n f_{n\mathbf{k}} \varepsilon_{pqr} b_{n,r}(\mathbf{k}). \tag{1.54}$$

The expression (1.54), or equivalently (1.1) was first derived by Karplus and Luttinger [4]. For this reason, it is called the Karplus-Luttinger expression. Since (1.54) depends only on the band structure of the material, and not the impurity concentration, it is known as the *intrinsic conductivity*.

The symmetry of the crystal determines whether $\mathbf{b}_n(\mathbf{k})$ contributes to the anomalous Hall conductivity [27]. In crystals with time-reversal symmetry, (1.51) implies that $\mathbf{b}_n(-\mathbf{k}) = -\mathbf{b}_n(\mathbf{k})$. With $\mathbf{b}_n(\mathbf{k})$ odd in $\mathbf{k}$, and $f_n(\mathbf{k})$ even in $\mathbf{k}$, the Brillouin zone integral in (1.1) vanishes. Therefore, if the Hamiltonian of the system is time-reversal invariant, the total intrinsic anomalous Hall conductivity vanishes. In a system with inversion symmetry, (1.51) implies that $\mathbf{b}_n(\mathbf{k}) = \mathbf{b}_n(-\mathbf{k})$. Therefore, when the Hamiltonian is invariant under both time-reversal and inversion symmetry, $\mathbf{b}_n(\mathbf{k}) = 0$ everywhere in the Brillouin zone.

The anomalous velocity term is related to the Berry curvature of the bands. Defining the Berry connection

$$\mathbf{a}_n(\mathbf{k}) = i\langle u_{n\mathbf{k}} | \nabla_{\mathbf{k}} | u_{n\mathbf{k}} \rangle, \tag{1.55}$$

then the Berry curvature is given by

$$\mathbf{b}_n(\mathbf{k}) = \nabla_{\mathbf{k}} \times \mathbf{a}_n(\mathbf{k}). \tag{1.56}$$

From perturbation theory, these definitions can be expressed as a sum over all bands:

$$a_{n,p}(\mathbf{k}) = i \sum_{m \neq n} \frac{v_{nm,p}(\mathbf{k})}{E_m(\mathbf{k}) - E_n(\mathbf{k})}, \tag{1.57}$$

and

$$b_{m,p}(\mathbf{k}) = -2\hbar^2 \,\mathrm{Im} \sum_{m \neq n} \frac{\varepsilon_{pqr} v_{nm,q}(\mathbf{k}) v_{mn,r}(\mathbf{k})}{\left[E_m(\mathbf{k}) - E_n(\mathbf{k})\right]^2}, \tag{1.58}$$

where $v_{mn,i}(\mathbf{k}) = \langle u_{m\mathbf{k}} | v_i(\mathbf{k}) | u_{n\mathbf{k}} \rangle$.

1.4.2 Phenomenological Description of the Karplus-Luttinger Contribution

The expansion (1.11) is usually justified by assuming a valid Taylor expansion of σ_{ij} in M, but it is not clear that the Karplus-Luttinger formula (1.1) admits such an expansion.

The Fermi-Dirac function is discontinuous at the Fermi energy, and the Berry curvature is singular at points of degeneracy in the Brillouin zone. We have little reason to expect that the conductivity is even a continuous function of the magnetization, let alone sufficiently differentiable to admit a Taylor expansion that converges quickly over all M.

Although it's tempting to dismiss these issues as formalities, we should remain aware of them in light of the following findings: First, singularities in the Berry curvature comprise about half of the total intrinsic Hall conductivity in the 3d metals [7]. Second, previous calculations of σ in $SrRuO_3$ found that σ is varies erratically as a function of the Fermi level [8]. Finally, it has been argued that in some materials the Fermi surface changes topology under rotations of the magnetization [28]. Given the large variation of $\Omega_{n\mathbf{k}}$ seen previously in the vicinity of the Fermi level, we must be somewhat cautious in assuming smooth variation of σ as $\mathbf{M}$ rotates [6].

We can appeal to the Stone-Weierstrass theorem to show that such an expansion exists over an intervals where σ is a continuous function in M. Standard theorems from Fourier analysis show that, if σ is square integrable over the sphere, then the spherical harmonic expansion converges to σ, so we don't need to rely on the use of Taylor's theorem to justify the expansion. The calculations of σ in subsequent chapters make it evident that the polynomial expansion is valid to within numerical limits.

1.5 First-Principles Calculations of the Intrinsic Anomalous Hall Conductivity

1.5.1 Density Functional Theory

The electronic structure of a material, neglecting nuclear motions, is described by the Hamiltonian [29].

$$\hat{h}(\mathbf{r}) = T + V_{\text{ion}} + V_{\text{Coulumb}} = \frac{-\hbar^2}{2m}\sum_{i=1}^{N}\nabla_i^2 - e^2\sum_{j=1}^{N_a}\sum_{i=1}^{N}\frac{Z_j}{|\mathbf{R_j}-\mathbf{r_i}|} + \frac{e^2}{2}\sum_{i=1,j\neq i}^{N}\frac{1}{|\mathbf{r}_i-\mathbf{r}_j|}. \quad (1.59)$$

Eq. (1.59) is not solved directly, but further refined by a series of approximations. The Hohenberg-Kohn theorem shows that the ground state solution to (1.59) is a functional of the electron density. The Kohn-Sham formalism enables us to construct a single-particle Hamiltonian with the same charge density as the interacting system, at the expense of introducing an unknown *exchange-correlation* potential, which must be approximated. Finally, the ionic Coulomb potential is replaced by a pseudopotential to provide both faster convergence of the valence electron wave functions and to introduce spin-orbit coupling.

The basic variable in the fully relativistic Kohn-Sham formulation is the density matrix:

$$\rho(\mathbf{r},\sigma,\sigma') = \sum_i f_i \psi_i^*(\mathbf{r},\sigma)\psi_i(\mathbf{r},\sigma'), \quad (1.60)$$

σ is a spin index, the $\psi_i(\mathbf{r},\sigma)$ are the two components of a single-particle spinor wave functions, and f_i is the occupancy of the state ψ. The charge density is then given by:

$$n(\mathbf{r}) = \sum_{i,\sigma} f_i \psi_i^*(\mathbf{r},\sigma)\psi_i(\mathbf{r},\sigma). \tag{1.61}$$

Eq. (1.60) is usually written in terms of the particle density $n(\mathbf{r})$ and the magnetization density $m(\mathbf{r})$

$$\rho(\mathbf{r},\sigma,\sigma') = \frac{1}{2}\left[n(\mathbf{r})\mathbf{I} + \mathbf{m}(\mathbf{r})\cdot\mathbf{S}\right] \tag{1.62}$$

where the operator $\mathbf{S} = \sigma_x\hat{\mathbf{x}} + \sigma_y\hat{\mathbf{y}} + \sigma_z\hat{\mathbf{z}}$ and the σ_i are the 2×2 Pauli spin matrices.

The functions ψ_i satisfy

$$\left(-\frac{\hbar^2}{2m}\nabla^2 + \sum_{\sigma'} V_{scf}(\mathbf{r},\sigma,\sigma')\right)\psi_i(\mathbf{r},\sigma) = E_i\psi_i(\mathbf{r},\sigma) \tag{1.63}$$

where $V_{scf}(\mathbf{r},\sigma,\sigma')$ is the *self-consistent potential*. We can express $V_{scf}(\mathbf{r},\sigma,\sigma')$ as

$$V_{scf}(\mathbf{r},\sigma,\sigma') = V_{ext}(\mathbf{r}) + e^2\int\frac{n(\mathbf{r}')}{|\mathbf{r}-\mathbf{r}'|}d\mathbf{r}' + V_{xc}(\mathbf{r}) - \mu_B\mathbf{m}(\mathbf{r})\cdot\mathbf{B}_{xc}(\mathbf{r}). \tag{1.64}$$

The first term on the right-hand side of (1.64) is the *external potential*, which in our calculations is the pseudopotential from the ionic core. The second term is known as the *Hartree potential*. The last two terms are given by

$$\mathbf{B}_{xc}(\mathbf{r}) = -\nabla_{\mathbf{m}}E_{xc} \tag{1.65}$$

$$V_{xc}(\mathbf{r}) = \frac{\partial E_{xc}}{\partial n}, \tag{1.66}$$

where E_{xc} is the exchange-correlation functional (discussed in 1.5.2). Both the Hartree potential and the exchange-correlation potential are functionals of the charge density $n(\mathbf{r})$, so (1.63) and (1.60) are a pair of nonlinear equations that must be solved both for the wave functions ψ_i and the charge density $n(\mathbf{r})$.

The solution of these equations is usually accomplished via a *self-consistency* procedure. First, a trial density $n(\mathbf{r})$ is constructed, and a V_{scf} is calculated from the trial density. Next, (1.63) is solved for the wave functions ψ_i. Once a set of ψ_i have been found a new trial density is constructed from (1.62), and the procedure repeats until a chosen termination criteria is reached. The final self-consistent charge density $n(\mathbf{r})$ may then be saved and used as an input to calculate other electronic properties.

1.5.2 The Local Spin Density and Generalized Gradient Approximations

The exchange-correlation functional E_{xc} accounts for much of the electron-electron interaction of the material. Although the exact exchange-correlation functional, i.e. one that

reproduces the ground state density of the exact many-body Hamiltonian (1.59), can be shown to exist, the exact functional is unknown, and we must resort to the use of an approximation. Many approximate exchange-correlation potentials exist. The local spin density approximation and the generalized gradient approximation are among the most commonly used approximations. We have chosen to use the Perdew-Burke-Ernzerhof (PBE) parameterization of the generalized gradient approximation for the calculations of the anomalous Hall conductivity.

1.5.3 Plane Wave Pseudopotential Method

In this section we describe the plane wave expansion of the Kohn-Sham equations and describe the approximation of the external potential due to the ionic cores by an equivalent *pseudopotential*.

Although it would seem that the correct Hamiltonian for a relativistic calculation of the band structure is the Dirac equation, Kleinman [30] showed that the relativistic effects can be modelled with the use of a relativistic pseudopotential and a non-relativistic Hamiltonian. One can solve the Dirac equation for a spherical potential, and from this solution construct an approximate pseudopotential for use in a non-relativistic Hamiltonian of the form (1.63). This method is accurate to order α^2 in the fine-structure constant. Defining the spin-averaged and spin-orbit parts of the pseudopotential

$$V_l^{\mathrm{so}}(r) = \frac{2}{2l+1}\left[V_{l+1/2}^{\mathrm{ion}}(r) - V_{l-1/2}^{\mathrm{ion}}(r)\right], \tag{1.67}$$

and

$$V_l^{\mathrm{avg}}(r) = \frac{1}{2}\left[V_{l+1/2}^{\mathrm{ion}}(r) + V_{l-1/2}^{\mathrm{ion}}(r)\right] \tag{1.68}$$

the ionic pseudopotential is written

$$V_{\mathrm{ps}}^{\mathrm{ion}}(r) = \sum_l |l\rangle \left[V_l^{\mathrm{so}}(r)\mathbf{L}\cdot\mathbf{S} + V_l^{\mathrm{avg}}(r) + (1/4)V_l^{\mathrm{so}}(r)\right] \langle l| \tag{1.69}$$

Translational symmetry of the electronic wave functions in a solid implies that they satisfy Bloch's theorem

$$\psi_{n\mathbf{k}} = \exp(i\mathbf{k}\cdot\mathbf{r})u_{n\mathbf{k}}(\mathbf{r}) \tag{1.70}$$

where $u_{n\mathbf{k}}(\mathbf{r})$ is periodic in $\mathbf{r}$, and $\mathbf{k}$ is a vector, and n is an index identifying the n-th eigenfunction. The density matrix may then be written as

$$\rho(\mathbf{r},\sigma,\sigma') = \sum_{n\mathbf{k}} f_{n\mathbf{k}}\psi_{n\mathbf{k}}^*(\mathbf{r},\sigma)\psi_{n\mathbf{k}}((r),\sigma'), \tag{1.71}$$

The spinor wave functions above are expanded in terms of plane waves,

$$\psi_{n\mathbf{k}}(\mathbf{r}) = \exp(i\mathbf{k}\cdot\mathbf{r})\sum_{\mathbf{G}}\begin{pmatrix} a(\mathbf{k}+\mathbf{G})\exp(i\mathbf{G}\cdot\mathbf{r}) \\ b(\mathbf{k}+\mathbf{G})\exp(i\mathbf{G}\cdot\mathbf{r}) \end{pmatrix} \tag{1.72}$$

where $\mathbf{G}$ is a vector in the reciprocal lattice

1.5.4 Wannier Functions

The success of our attempt to calculate the anomalous Hall conductivity from first principles depends on our ability to calculate the **k**-derivatives in (1.55) and our ability to perform the integration over the Brillouin zone in (1.1). Although the **k**-derivatives can be evaluated using a sum over all states in (1.58), the computational cost of this scheme makes it prohibitive for studying all but the simplest systems. While Yao used this approach in an early calculation of the Hall conductivity, a more efficient scheme was introduced by Wang et al. in 2006. In their scheme, the Wannier representation is employed as an intermediate representation to calculate the terms appearing in (1.1). We have employed this scheme in our calculations of the anomalous Hall conductivity. We describe the scheme in detail in this section.

Conventionally, the Wannier functions $\phi_n(\mathbf{r})$ are defined by

$$\phi_n(\mathbf{r}-\mathbf{R}) = \frac{1}{\Omega}\int d^3\mathbf{k}\,\exp(-i\mathbf{k}\cdot\mathbf{R})\,\psi_{n\mathbf{k}}, \tag{1.73}$$

where $\psi_{n\mathbf{k}}$ is the n-th eigenfunction of the Hamiltonian [31]. This definition does not specify a unique ϕ_n for a given Hamiltonian. The phases of the $\psi_{n\mathbf{k}}$ are not defined, and the band index n is not well defined at points of degeneracy in the Brillouin zone. We can combine these two statements by saying that the Wannier functions fail to be gauge invariant under a **k**-dependent unitary transformation

$$\psi'_{n\mathbf{k}}(\mathbf{r}) = \sum_m U_{mn}(\mathbf{k})\,\psi_{m\mathbf{k}}. \tag{1.74}$$

This gauge dependence makes the numerical construction of Wannier functions difficult, since a numerical formulation depends on the rapid convergence of the inverse transform

$$\psi_{n\mathbf{k}} = \sum_{\mathbf{R}} \phi_n(\mathbf{r}-\mathbf{R})\exp(i\mathbf{k}\cdot\mathbf{R}), \tag{1.75}$$

which requires the ϕ_n to converge rapidly with **R**, so that the sum over **R** can be truncated without introducing appreciable error. In other words, we require a gauge condition that localizes $\phi_n(\mathbf{r})$.

Marzari and Vanderbilt described such a localization condition for a group of bands separated by a band gap (e.g. the valence bands of an insulator), and termed the resulting Wannier functions *maximally localized* Wannier functions. Souza et al. later removed the gap condition and provided a practical scheme for calculating the (partially-occupied) Wannier functions in a metal, by generalizing the definition (1.73) so that the $\psi_{n\mathbf{k}}$ are no longer eigenfunctions of the crystal Hamiltonian, but basis functions spanning a subspace of the eigenfunctions. These $u_{n\mathbf{k}}$ are a basis chosen to span the eigenstates lying within an energy window $E_{min} < E_n < E_{max}$. The basis states defining the Wannier functions are written $u^W_{n\mathbf{k}}$, and the Hamiltonian eigenstates as $u^H_{n\mathbf{k}}$.

1.5.5 Wannier Interpolation

The $u^W_{n\mathbf{k}}$ span a subspace of the $u^H_{n\mathbf{k}}$. This property allows us to use the $u^W_{n\mathbf{k}}$ as a basis set with which to interpolate operators over this subspace (for example, by interpolating the Hamiltonian, we can interpolate the energy bands of the crystal). The two basis sets are related a unitary transformation

$$u^W_{n\mathbf{k}} = \sum_m U_{mn}(\mathbf{k}) u^H_{m\mathbf{k}}, \tag{1.76}$$

where the $U(\mathbf{k})$ are determined by the localization condition. The matrix elements of an operator $\hat{O}$ in this basis are then

$$O^{(W)}(\mathbf{k}) = U(\mathbf{k}) O^{(H)}(\mathbf{k}) U^\dagger(\mathbf{k}) \tag{1.77}$$

where the matrices $O(\mathbf{k})$ are defined by the matrix elements

$$O_{mn}(\mathbf{k}) = \langle u_{m\mathbf{k}} | \hat{O}(\mathbf{k}) | u_{n\mathbf{k}} \rangle. \tag{1.78}$$

Now we define

$$O^{(W)}(\mathbf{R}) = \frac{1}{N} \sum_{\mathbf{k}} \exp(-i\mathbf{k}\cdot\mathbf{R}) O^{(W)}(\mathbf{k}). \tag{1.79}$$

The sum in (1.79) is a discrete Fourier transform, where the integration is taken over the Brillouin zone, in analogy with the continuous transform in (1.73). The localization in the construction of the $u_{n\mathbf{k}}$ ensures that the sum converges to the integral. Once we calculate $O^{(W)}(\mathbf{R})$, we can then calculate

$$O^{(W)}(\mathbf{k}') = \sum_{\mathbf{R}} \exp(i\mathbf{k}\cdot\mathbf{R}) O^{(W)}(\mathbf{R}). \tag{1.80}$$

where $\mathbf{k}'$ is an arbitrary point in the Brillouin zone. The advantage of using (1.80) to evaluate an operator is that the $O^{(W)}(\mathbf{R})$ need only be calculated once, and then (1.80) may be used to evaluate $O^{(W)}(\mathbf{k}')$ at an arbitrary $\mathbf{k}$-point. The Hamiltonian in the smooth basis $H^{(W)}$ is no longer diagonal, since these smooth basis functions are not required to be eigenfunctions of $\hat{H}$. To construct eigenfunctions of the Hamiltonian in the smooth basis, it is necessary to find matrices $U(\mathbf{k})$ which diagonalize $H^{(W)}$ at each point $\mathbf{k}'$ by a transformation

$$H^{(H)}(\mathbf{k}') = U^\dagger(\mathbf{k}') H^{(W)}(\mathbf{k}') U(\mathbf{k}') \tag{1.81}$$

where $H^{(H)}$ is a diagonal matrix. The final steps in evaluating the interband matrix elements of an operator are to calculate $O^{(W)}(\mathbf{k}')$ in (1.80), and then transform the operator into the basis diagonalizing H, using the matrices $U(\mathbf{k}')$ in (1.82):

$$O^{(H)}(\mathbf{k}') = U^\dagger(\mathbf{k}') O^{(W)}(\mathbf{k}') U(\mathbf{k}'). \tag{1.82}$$

This procedure is called *Wannier interpolation*, since by (1.79), the $O^{(W)}(\mathbf{R})$ are the matrix elements of Wannier functions constructed from smooth Bloch functions.

The final steps of the Wannier interpolation procedure must be modified for the Berry connection $\mathbf{a}_n(\mathbf{k})$, since the derivative on the right-hand side of (1.55), operates directly on the basis functions. The necessary modifications are described in detail in ref. [6]. Such a quantity no longer obeys the relationship (1.82), but instead contains an additonal term

$$\mathbf{a}^{(H)}(\mathbf{k}) = U^{\dagger}(\mathbf{k})\mathbf{a}^{(W)}(\mathbf{k})U(\mathbf{k}) + iU^{\dagger}(\mathbf{k})\left(\nabla_{\mathbf{k}}U(\mathbf{k})\right). \tag{1.83}$$

The same considerations apply to the Berry curvature $\Omega_{mn,pq}(\mathbf{k})$, resulting in the transformation law

$$\Omega_{pq}(\mathbf{k}) = \partial_p\left(U^{\dagger}(\mathbf{k})a_q^{(W)}(\mathbf{k})U(\mathbf{k})\right) - \partial_q\left(U^{\dagger}(\mathbf{k})a_p^{(W)}(\mathbf{k})U(\mathbf{k})\right) - i[U^{\dagger}(\mathbf{k})\partial_p U(\mathbf{k}), U^{\dagger}(\mathbf{k})\partial_q U(\mathbf{k})]. \tag{1.84}$$

The Wannier interpolation procedure is implemented as follows. First, we use a calculate a self-consistent Hamiltonian, using a full plane wave basis set. Second, we use this self-consistent Hamiltonian to calculate the Bloch functions $u_{n\mathbf{k}}$ on a coarse grid over $\mathbf{k}$-space. We then construct Wannier functions from the $u_{n\mathbf{k}}$, using the localization criteria to ensure that the matrices $O^{(W)}(\mathbf{R})$ decay quickly with $\mathbf{R}$. Finally, we use (1.80) to recalculate the band structure on a dense grid on the Brillouin zone. The advantage of using the interpolation procedure (from a small set of Bloch states), as opposed to directly calculating the eigenfunctions of the self-consistent Hamiltonian at each $\mathbf{k}$ is speed. The sum in (1.80) can be evaluated almost 1000 times faster than the iterative diagonalization of the self-consistent Hamiltonian can be performed for each $\mathbf{k}$. The dense Brillouin zone integrations needed to integrate the Berry curvature in (1.1) make Wannier interpolation the only feasible method for accurate studies of the intrinsic anomalous Hall conductivity.

Chapter 2

Cobalt

Parts of this chapter have been published in ref. [32].

In this chapter, we present a detailed first-principles study of the orientation dependence of the intrinsic AHE in Co. Anisotropy in the AHE has been measured in single crystals of the ferromagnetic elements (hcp Co [24], hcp Gd [33], fcc Ni [19], and bcc Fe [34]), and more recently in ferromagnetic compounds [35, 36, 37]. On the theoretical side there has been little progress beyond the basic phenomenological description. To our knowledge, the only attempt at a microscopic model has been the tight-binding study of Ref. [35]. Because the AHC is very sensitive to fine details in the band structure [5, 8, 6], a quantitative *ab initio* theory of anisotropy is highly desirable. It is also not obvious that the phenomenological description of magnetocrystalline anisotropy [14, 15] applies to the AHC given by Eq. (1.1). The Berry curvature undergoes strong and rapid variations in k-space, with sharp peaks and valleys from avoided crossings near the Fermi level [5, 8, 6]. It has been argued that such behavior cannot be described perturbatively [5], and that it often gives rise to a complex or even irregular behavior of the AHC as a function of exchange splitting and Fermi level position [8]. This raises the possibility that the orientation dependence of σ^a_{ij} may also not be smooth. We find instead that in hcp Co it is strong but remarkably smooth, and can be described by a phenomenological power-series expansion. The calculated anisotropy accounts for the experimental observations in both single crystals (angular dependence) and polycrystalline films (angular average).

2.1 The Hall conductivity in hcp crystals

In this section we first present the phenomenological expansion of the anomalous Hall conductivity σ^a of an hcp ferromagnet to third order in powers of the magnetization $\mathbf{M}$, and for fixed magnitude of $\mathbf{M}$ we re-express it in terms of $l = 1$ and $l = 3$ spherical harmonics. The orientation dependence of $\sigma^a(\mathbf{M})$ can be described phenomenologically by expanding

in powers of the direction cosines $\{\alpha_i\}$ of **M** [14, 15]:

$$\sigma^a_{ij}(\hat{\mathbf{m}}) = a_{ijp}\alpha_p + a_{ijpqr}\alpha_p\alpha_q\alpha_r + \ldots \tag{2.1}$$

Here $\hat{\mathbf{m}} = \alpha_x\hat{\mathbf{x}} + \alpha_y\hat{\mathbf{y}} + \alpha_z\hat{\mathbf{z}}$ is the unit vector along the spin magnetization **M**, and it is assumed that the magnitude of **M** is independent of orientation, as is the case for hcp Co to a very good approximation. Crystal symmetry and other considerations reduce the number of independent coefficients in Eq. (2.1). They are tabulated for the hcp structure to third order in Ref. [14]:

$$\sigma^a_1 = a_{231}\alpha_1 + a_{23111}(\alpha_1^3 + \alpha_1\alpha_2^2) + a_{31233}\alpha_1\alpha_3^2 \tag{2.2}$$
$$\sigma^a_2 = a_{231}\alpha_2 + a_{23111}(\alpha_2^3 + \alpha_2\alpha_1^2) + a_{31233}\alpha_2\alpha_3^2 \tag{2.3}$$
$$\sigma^a_3 = a_{123}\alpha_3 + a_{12113}(\alpha_3\alpha_1^2 + \alpha_3\alpha_2^2) + a_{12333}\alpha_3^3. \tag{2.4}$$

The uniaxial nature of the hcp structure implies $a_{231} \neq a_{123}$, producing a misalignement between σ^a and **M** to first order in the expansion.

There are six coefficients in Eq. (2.2), the number needed to describe σ^a to third order as a function of the orientation *and* magnitude of **M**. For fixed magnitude, the angular dependence requires only four independent parameters, which are conveniently chosen as the coefficients of an expansion in orthonormal real spherical harmonics defined in (1.24), resulting in

$$\sigma^a_1 = A^1_1 C^1_1(\theta,\phi) + A^1_3 C^1_3(\theta,\phi) \tag{2.5}$$
$$\sigma^a_2 = A^1_1 S^1_1(\theta,\phi) + A^1_3 S^1_3(\theta,\phi) \tag{2.6}$$
$$\sigma^a_3 = A^0_1 C^0_1(\theta,\phi) + A^0_3 C^0_3(\theta,\phi). \tag{2.7}$$

Using the conventions of appendix B to define the real spherical harmonics, the coefficients are given by

$$A^0_1 = \frac{2}{5}\sqrt{\frac{\pi}{3}}(5a_{123} + 2a_{12113} + 3a_{12333}) \tag{2.8}$$
$$A^1_1 = -\frac{2}{5}\sqrt{\frac{\pi}{3}}(5a_{231} + a_{31233} + 4a_{23111}) \tag{2.9}$$
$$A^0_3 = -\frac{4}{5}\sqrt{\frac{\pi}{7}}(a_{12113} - a_{12333}) \tag{2.10}$$
$$A^1_3 = -\frac{4}{5}\sqrt{\frac{2\pi}{21}}(a_{31233} - a_{23111}). \tag{2.11}$$

The four coefficients A^0_1, A^1_1, A^0_3, and A^1_3 were obtained from a least-squares fitting to the first-principles calculations at $T = 0$. The rather good fit and, more generally, the smooth orientation dependence of the calculated intrinsic AHC seen in Fig. 2.1 should be contrasted with the oscillatory behavior found when scanning the chemical potential [8].

The comparatively less dramatic angular dependence can perhaps be rationalized by noting that the zero-spin-orbit limit is the same regardless of the magnetization direction (e.g., same crossings between Fermi surface sheets).

To characterize the anisotropy we write σ^a as

$$\sigma^a = \sigma_m \hat{\mathbf{m}} + \sigma_\theta \hat{\theta} + \sigma_\phi \hat{\phi}, \tag{2.12}$$

where θ and ϕ are respectively the polar and azimuthal angles of $\mathbf{M} = M\hat{\mathbf{m}}$. In macroscopically isotropic systems such as polycrystals $\sigma^a \parallel \mathbf{M}$, i.e., $\sigma_\theta = \sigma_\phi = 0$.

2.2 Resistivity and Conductivity in hcp crystals

The comparison between the calculated Hall conductivities and the measured Hall resistivities requires inverting the resistivity tensor. For $\theta = 0$ and $\theta = \pi/2$ the vectors σ^a and $\mathbf{M}$ are parallel. It then suffices to consider the components of ρ and σ in the orthogonal plane. The 2×2 in-plane resistivity matrix reads

$$\rho = \begin{pmatrix} \rho_{11} & \rho_{12} \\ -\rho_{12} & \rho_{22} \end{pmatrix}, \tag{2.13}$$

with inverse

$$\sigma = \rho^{-1} = \frac{1}{\rho_{11}\rho_{22} + \rho_{12}^2} \begin{pmatrix} \rho_{22} & -\rho_{12} \\ \rho_{12} & \rho_{11} \end{pmatrix}. \tag{2.14}$$

For $\theta = 0$ this yields the familiar relation between the Hall conductivity $\sigma_z^a = \sigma_{xy}$, the Hall resistivity $\rho^a = \rho_{yx}$, and the longitudinal resistivity ρ_{xx}:

$$\sigma_z^a = -\frac{\rho_{xy}}{\rho_{xx}\rho_{yy} + \rho_{xy}^2} = \frac{\rho_{yx}}{\rho_{xx}^2 + \rho_{xy}^2} \simeq \frac{\rho^a(\theta = 0)}{\rho_{xx}^2}, \tag{2.15}$$

where we used $\rho_{xx} = \rho_{yy}$ and $\rho^a \ll \rho_{xx}$. For $\theta = \pi/2$ the in-plane resistivity is anisotropic ($\rho_{yy} \neq \rho_{zz}$) and thus

$$\sigma_x^a \simeq \frac{\rho^a(\theta = \pi/2)}{\rho_{yy}\rho_{zz}} = \frac{\rho^a(\theta = \pi/2)}{\rho_{xx}\rho_{zz}}. \tag{2.16}$$

Dividing Eq. (2.15) by Eq. (2.16) yields the relation

$$\frac{\sigma^a(\theta = 0)}{\sigma^a(\theta = \pi/2)} \simeq (\rho_{zz}/\rho_{xx}) \frac{\rho^a(\theta = 0)}{\rho^a(\theta = \pi/2)}. \tag{2.17}$$

Since the diagonal resistivity is not isotropic, $\rho_{zz} \neq \rho_{xx}$, and (2.17) shows that the ratio of two Hall conductivities does not equal the ratio of the corresponding Hall resistivities, but has the additional factor ρ_{zz}/ρ_{xx}. In an isotropic crystal, $\rho_{zz}/\rho_{xx} = 1$, so the two ratios are equal. If we use the room-temperature values for hcp Co from Ref. [38], $\rho_{zz} = 10.280 \times 10^{-6}\,\Omega$ cm and $\rho_{xx} = 5.544 \times 10^{-6}\,\Omega$ cm, then $(\rho_{zz}/\rho_{xx}) \approx 1.85$. Therefore, after rotating θ from the *ab*-plane to the *c*-axis, the ratio of the Hall conductivities is 1.85 times the ratio of the corresponding Hall resistivities.

2.3 Method

We have carried out fully-relativistic band-strucutre calculations for hcp and fcc Co at the experimental lattice constants of 4.74 and 6.68 bohr respectively, using the `Quantum ESPRESSO` code [39]. The pseudopotential was generated using similar parameters as in Ref. [7]. The plane-wave basis cutoff for the expansion of the valence wave functions was set at 140 Ry, and the PBE generalized-gradient approximation[40] was used for the exchange-correlation functional. The self-consistent ground state was obtained using a $16 \times 16 \times 16$ Monkhorst-Pack mesh [41] of k points and a fictitious Fermi smearing [42] of 0.02 Ry for the Brillouin-zone integration. The calculation was initialized with the spin magnetization pointing along a specified direction; when self-consistency was achieved using a convergence threshold of 10^{-8} Ry for the total energy, the final cell-averaged magnetization was found to be parallel to the initial magnetization. Because of the spin-orbit interaction, the spin density $\sigma(\mathbf{r})$ is not strictly collinear within the crystalline cell. In hcp Co we find $|\int_{\text{cell}} d^3r\, \sigma(\mathbf{r})| = 3.20\,\mu_{\text{B}}$, while $\int_{\text{cell}} d^3r\, |\sigma(\mathbf{r})| = 3.53\,\mu_{\text{B}}$ (both values are independent of the spin magnetization direction to the given accuracy). Hence it was not necessary to impose an energy-penalty constraint to fix $\mathbf{M}$ during the energy minimization.

For each spin magnetization direction we froze the self-consistent potential and performed a non-self-consistent calculation of the lowest 48 (28 for fcc Co) Bloch eigenstates and eigenvalues over a $10 \times 10 \times 10$ uniform k point mesh including the Γ point. From these, maximally-localized Wannier functions were then calculated using the method of Refs. [43, 44], as implemented in the `wannier90` code [45]. For both fcc and hcp Co we chose 18 WFs per atom, covering the s, p, and d characters and both spins. During the disentanglement step used to select the Wannier subspace [44] the upper limit of the "outer energy window" was set at 41.4 eV above the Fermi level. All states up to 11.4 eV above the Fermi level were kept in the subspace by setting the "inner energy window" accordingly. The maximally-localized Wannier functions spanning the resulting subspace were then calculated by minimizing the spread functional [43]. The functional minimization procedures carried in both steps (subspace selection and localization) were initialized by projecting onto trial orbitals of the same type as used in Ref. [6] for bcc Fe: three t_{2g} d-like orbitals and six sp^3d^2 hybrids per spin channel and per atom.

The AHC was calculated using (1.1). The k space integral of the Berry curvature was carried out using a Wannier-interpolation scheme [6] to sample efficiently the Brillouin zone over a $125 \times 125 \times 125$ uniform k-point mesh ($200 \times 200 \times 200$ for fcc Co), with a $5 \times 5 \times 5$ adaptively refined mesh around the points where the magnitude of the Berry curvature exceeded 10 Å^2. The magnetic circular dichroism (MCD) spectrum was computed in a similar manner [46] on the same interpolation mesh used for calculating the AHC.

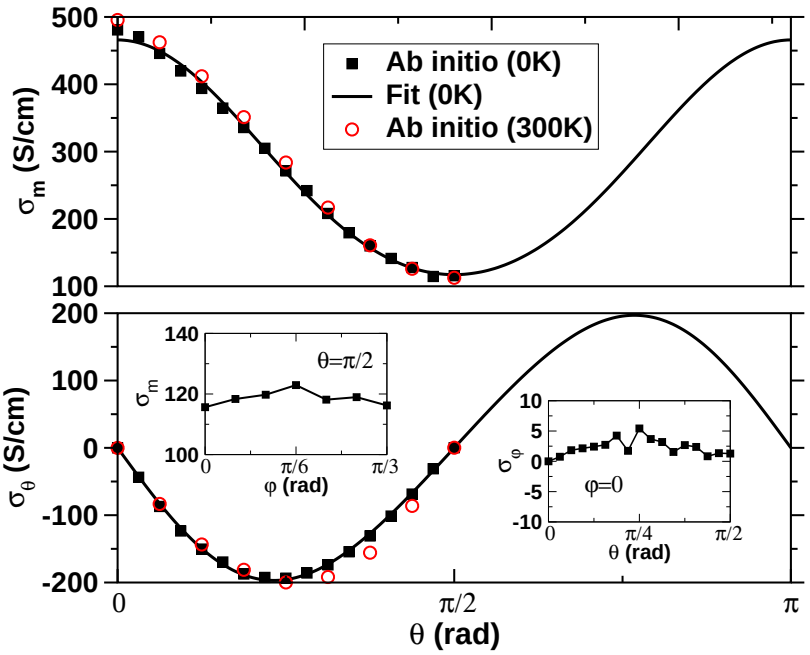

Figure 2.1: Evolution of the components of the anomalous Hall conductivity parallel (σ_m) and perpendicular (σ_θ) to the magnetization [Eq. (2.12)] as $\mathbf{M}$ is tilted by θ from the c-axis towards the a-axis. The solid lines are fits to the first-principles data, as described in the text. The left and right insets shows respectively $\sigma_m(\pi/2,\phi)$, and $\sigma_\phi(\theta,0)$.

2.4 Results

The AHC of hcp Co was calculated for several orientations of the cell-averaged magnetization in the ac-plane ($\phi = 0$). The tilting angle θ was increased from 0 ($\mathbf{M} \parallel c$-axis) to $\pi/2$ ($\mathbf{M} \parallel a$-axis) in steps of $\pi/32$, and for each step the vector $\sigma^a(\theta,\phi)$ was calculated. Fig. 2.1 contains the numerical results: $\sigma_m(\theta,0)$ and $\sigma_\theta(\theta,0)$ are shown in the panels, while the insets contain additional data which confirms the absence of (or very weak) basal-plane anisotropy. The vectors σ^a and $\mathbf{M}$ start out parallel, but as $\mathbf{M}$ begins to tilt away from the c-axis σ^a lags behind ($\sigma_\theta < 0$), and they become parallel again upon reaching the basal plane. The AHC is strongly anisotropic, decreasing in magnitude by a factor of $481/116 \simeq 4.1$ between $\theta = 0$ and $\theta = \pi/2$. This is in reasonable agreement with the ratio of 2.93 measured in single crystals at 290 K [24]. While strong, the angular dependence of σ^a is smooth, and can be described by Eqs. (2.5-2.7). A least-squares fitting to the data yields, in S/cm, $A_1^0 = 951.5$, $A_1^1 = -204.1$, $A_3^0 = 1.2$, and $A_3^1 = 38.4$, producing the solid-line curves in Fig. 2.1.

2.5 The Hall Conductivity in Polycrystalline Films

According to the spin-fluctuation model [47, 48], the thermal average $\langle\sigma^a\rangle_T$ as a function of the polar and azimuthal angles θ and ϕ of $\langle\hat{\mathbf{m}}\rangle_T$ is given by Eq. (2.5), with the coefficients A_l^m therein replaced by

$$A_l^m(T) = A_l^m(0)\left[\frac{M(T)}{M(0)}\right]^{l(l+1)/2}. \tag{2.18}$$

This "$l(l+1)/2$ power law" model was used to generate the plot in the inset of Fig. 4.

We evaluate at $T=0$ the orientational average $\sigma^a_{\rm poly} = \langle\sigma^a\cdot\hat{\mathbf{m}}\rangle$ of the anomalous Hall conductivity at T=0 from the data in Fig.2.1, finding $\sigma^a_{\rm poly} = 226$ S/cm. The value of $\sigma^a_{\rm poly}$ can also be obtained from the fitted coefficients in Eq. (2.5). Expressing $\hat{\mathbf{m}}$ in terms of $l=1$ spherical harmonics and invoking the orthonormality condition, one finds

$$\sigma^a_{\rm poly} = \frac{A_1^0 - 2A_1^1}{2\sqrt{3\pi}} = 221\,{\rm S/cm}, \tag{2.19}$$

where on the right-hand side we have used the values of A_1^0 and A_1^1. The good agreement between the two values confirms the validity of the phenomenological expansion. Eq. (2.19) is valid to all orders in the spherical-harmonic expansion. If the nonlinear terms in Eq. (2.2) are small, $\sigma^a_{\rm poly}$ can be estimated from the single-crystal AHC evaluated at $\theta=0$ and $\theta=\pi/2$ only:

$$\sigma^a_{\rm poly} \simeq \frac{1}{3}\sigma_m(0) + \frac{2}{3}\sigma_m(\pi/2) = 238\,{\rm S/cm}, \tag{2.20}$$

where $\sigma_m(\theta) = \sigma^a\cdot\hat{\mathbf{m}}$.

We now turn to the comparison with the measurements on polycrystalline films [10]. The films were magnetized along the growth direction by an applied field; assuming randomly oriented crystallites, each with a bulk-like Hall current density $\mathbf{J}^a(\theta,\phi)$, the net Hall current density in the films can be estimated by performing an orientational average: $\langle\mathbf{J}^a\rangle = \mathbf{E}\times\langle\sigma^a\rangle$. Because σ^a displays azimuthal isotropy, it suffices to average Eq. (2.12) over θ for fixed ϕ. The average of σ_θ vanishes (see Fig. 2.1), resulting in an isotropic AHC $\langle\sigma^a\rangle = \langle\sigma_m\rangle\hat{\mathbf{m}}$ of magnitude $\sigma^a_{\rm poly} = \int_0^{\pi/2}\sigma_m(\theta)\sin\theta\,d\theta = 226$ S/cm. This should be compared with the value $b = 205$ S/cm obtained in Ref. [10] by fitting the experimental data to Eq. (1.2). The experiment does not discriminate between the intrinsic and side-jump components of b, but the close agreement with the calculated $\sigma^a_{\rm poly}$ reinforces the conclusion [10] that the former dominates. Table 2.1 summarizes the comparison between our calculations and experiments.

2.6 Discussion

The anomalous Hall conductivities of single crystals magnetized along the c and a axes can be calculated from the experimental resistivities. We take the room-temperature

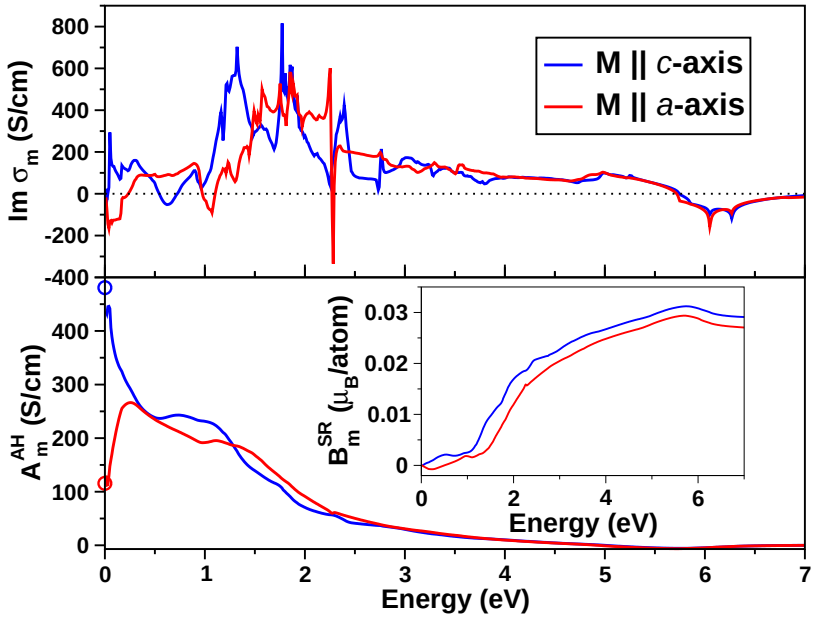

Figure 2.2: Upper panel: MCD spectrum for two magnetization directions. Lower panel: Cumulative contribution to the AHC from the spectrum above energy $\hbar\omega$. The circles denote the AHC calculated directly from Eq. (1.1). Inset: Cumulative contribution to the self-rotation part of the orbital magnetization from the spectrum below $\hbar\omega$.

Table 2.1: Anomalous Hall conductivity $|\sigma^a| = \sigma_m$ in S/cm for selected high-symmetry orientations of the magnetization in hcp and fcc Co. The AHC of polycrystalline samples is calculated as an orientational average (see text).

Co	Orientation	Calc.	Expt.
hcp	*c*-axis	481	683 [24]
	ab-plane	116	232 [24]
	Polycrystal	226	205 [10], 275 [23]
fcc	[001]	249	
	[110]	218	
	[111]	234	

anomalous Hall resistivities from Fig. 2 of Ref. [24]: $\rho^a(\theta=0)=2.5\times10^{-8}\,\Omega$ cm and $\rho^a(\theta=\pi/2)=0.853\times10^{-8}\,\Omega$ cm. Since the corresponding longitudinal resistivities are not given in that work, we use the room-temperature values from Ref. [38], $\rho_{zz}=10.280\times10^{-6}\,\Omega$ cm and $\rho_{xx}=5.544\times10^{-6}\,\Omega$ cm. Plugging these numbers into (2.16) and 2.17 we find the values given in Table 2.1, $\sigma_z^a(\theta=0)\sim 813$ S/cm and $\sigma_x^a(\theta=\pi/2)\sim 150$ S/cm. Given the disparate experimental sources used to obtain them, these numbers should be taken as approximate.

Next we discuss the origin of the strong anisotropy. The AHE of uniaxial crystals is anisotropic to first order in an expansion in powers of the magnetization (see Appendix B) while in cubic crystals anisotropy appears only in third-order [19], and is expected to be much weaker. For example, the AHC of fcc Co changes by less than 10% as a function of the magnetization direction (Table 2.1). Perhaps more surprising is the fact that the AHE in hcp Co appears to be considerably more anisotropic than both the magneto-optical spectrum [49] and the orbital magnetization [50, 51]. This is intriguing because the three phenomena are related by linear sum rules [52], and hence anisotropy appears at the same order.

The sum rules read $\langle\omega^{-1}\mathrm{Im}\,\sigma^a\rangle_\omega=(\pi/2)\sigma^a(\omega=0)$ and $\langle\mathrm{Im}\,\sigma^a\rangle_\omega=(\pi ec/\hbar)\mathbf{M}^{(\mathrm{I})}_{\mathrm{SR}}$, where $\langle f\rangle_\omega=\int_0^\infty f(\omega)d\omega$. $\sigma^a(\omega=0)$ is the dc AHC; at finite frequencies σ^a acquires an imaginary part which describes the differential absorption of right and left circularly-polarized light, or magnetic circular dichroism (MCD). The first sum rule expresses the AHC in terms of the first inverse moment of the MCD spectrum. The second relates $\mathbf{M}^{(\mathrm{I})}_{\mathrm{SR}}$, the "gauge-invariant self-rotation" part of the orbital magnetization [52], to the zero-th spectral moment.

The absorptive part of $\sigma_m(\omega)$ is plotted in the upper panel of Fig. 2.2 for $\theta=0,\pi/2$. The lower panel shows $A_m^{\mathrm{AH}}(\omega)=\frac{2}{\pi}\int_\omega^{\omega_{\max}}\frac{1}{\omega'}\mathrm{Im}\,\sigma_m(\omega')\,d\omega'$. For $\omega_{\max}\to\infty$ (in practice we use $\omega_{\max}=7$ eV) $A_m^{\mathrm{AH}}(0)=\sigma_m(\omega=0)$, so that $A_m^{\mathrm{AH}}(\omega>0)$ is the cumulative contribution to the AHC from optical transitions above ω. While for either orientation there are sizeable contributions to the AHC up to $\omega\sim 3.5$ eV, its orientation dependence is concentrated below 0.3 eV. At these low frequencies the MCD spectrum changes sign between $\theta=0$ and $\theta=\pi/2$. This difference gets magnified in the AHC via the inverse-frequency weight factor, producing the bifurcation below 0.3 eV of the two $A_m^{\mathrm{AH}}(\omega)$ curves. All frequencies are equally weighted in the orbital moment sum rule, which as a result is more isotropic. This is seen in the inset, where we plot $B_m^{\mathrm{SR}}(\omega)=\frac{V_c\hbar}{2\pi ec}\int_0^\omega\mathrm{Im}\,\sigma_m^a(\omega')d\omega'$, the cumulative contribution below ω to the gauge-invariant self-rotation per atom.

The origin of the low-frequency anisotropy can be seen in Fig. 2.3. The upper panel displays the energy bands for the two magnetization directions. Rotating $\mathbf{M}$ from the c-axis to the a-axis in the presence of the SOI turns various band crossings into avoided crossings and vice-versa. When this occurs close to the Fermi level the Berry curvature along $\mathbf{M}$ can flip sign in the process, while retaining a large magnitude. This is what happens near the L-point, as seen in the middle and lower panels, where we plot $-\Omega_{\mathbf{k}}\cdot\hat{\mathbf{m}}$ for the two orientations ($\Omega_{\mathbf{k},k}=(1/2)\varepsilon_{ijk}\sum_n f_{n\mathbf{k}}\Omega_{n\mathbf{k},ij}$ is the total Berry curvature at $\mathbf{k}$). The sensitivity

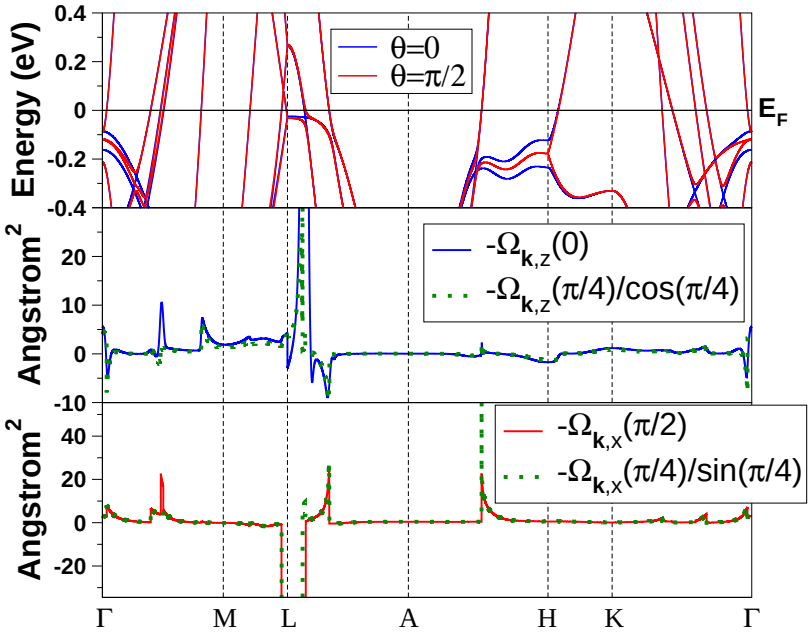

Figure 2.3: Upper panel: Energy bands close to the Fermi level for $\mathbf{M} \parallel c$-axis ($\theta = 0$) and $\mathbf{M} \parallel a$-axis ($\theta = \pi/2$). Middle and lower panels: k-space Berry curvature $\Omega_{\mathbf{k}}(\theta)$ for $\theta = 0$, $\theta = \pi/2$, and $\theta = \pi/4$. The full height of the resonance peaks near the L-point is of the order of 10^3 Å^2.

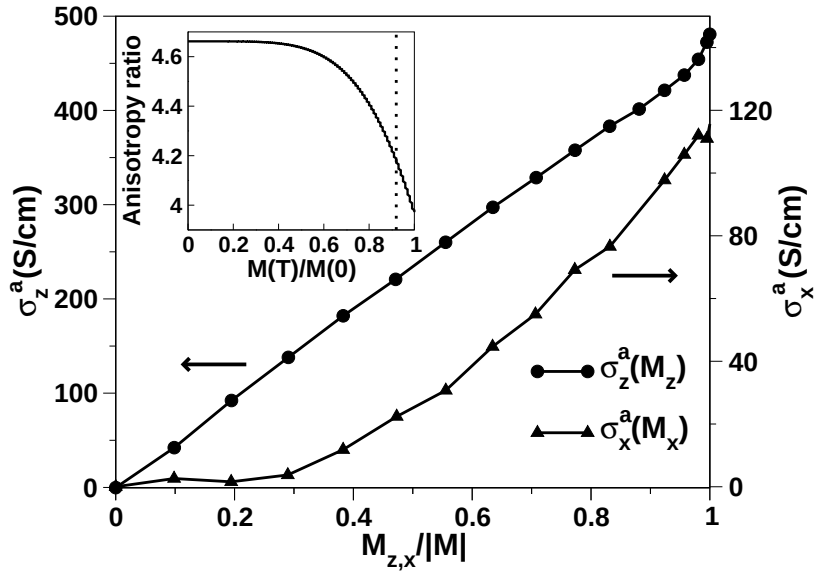

Figure 2.4: Evolution of σ^a as the magnetization is rotated in the *ac* plane, plotted as $\sigma_z^a(\cos\theta)$ and $\sigma_x^a(\sin\theta)$. Inset: Anisotropy ratio $\sigma_z^a(\theta=0)/\sigma_x^a(\theta=\pi/2)$ versus the reduced magnetization, according to the spin-fluctuation model. The dotted line denotes the approximate location of the hcp→fcc transition.

of the AHC to changes in the electron states near E_F may also be understood from the fact that σ^a can be recast as a Fermi surface integral [7, 53], whereas the orbital magnetization truly depends on all occupied states.

How can the spiky behavior of $\Omega_{\mathbf{k}}$ be reconciled with the smooth angular dependence displayed by $\sigma^a(\theta)$ in Fig. 2.1? According to the phenomenological expansion (2.5), $\sigma_i^a \propto M_i$ to leading order ($i = x,y,z$). This will be the case for the AHC given by Eq. (1.1) provided that $\Omega_{\mathbf{k},i} \propto M_i$ at each $\mathbf{k}$. This proportionality holds reasonably well even around strong resonance peaks, judging from the comparison in Fig. 2.3 between $\Omega_{\mathbf{k}}$ calculated at $\theta = \pi/4$ and at $\theta = 0, \pi/2$.

2.7 Temperature Dependence of the Anomalous Hall Conductivity

We end with a discussion of temperature effects. The AHC hardly changes as the Fermi-smearing temperature in Eq. (1.1) is varied from 0 K to 300 K (Fig. 2.1). This agrees with the constancy of the coefficient b of polycrystalline films in the range 78-350 K [10]. The angular dependence of the AHC can also give rise to a temperature dependence, via long-wavelength thermal fluctuations in $\hat{\mathbf{m}}$ [9]. According to this model, if $\sigma_i^a(T=0)$ changes

linearly with M_i upon rotating **M**, then $\sigma^a(T) = [M(T)/M(0)]\sigma^a(T=0)$. This model assumes that the magnetization thermally fluctuates about an easy axis. The applicability of this model to ferromagnetic Co is questionable, since interacting spin waves in ferromagnets show correlations, rather than simple thermal fluctuations, but this simple model does seem to explain the temperature dependence in Mn_5Ge_3 [9].

Fig. 2.4 shows that in hcp Co σ_z^a depends linearly on M_z, while the $\sigma_x^a(M_x)$ curve is significantly nonlinear (note that $|A_3^1/A_1^1| \gg |A_3^0/A_1^0|$). As a result, the a-axis AHC should decrease with T faster than $M(T)$, producing an increase with temperature of the ratio $\sigma_z^a(\theta=0)/\sigma_x^a(\theta=\pi/2)$. An estimate of the magnitude of this effect can be obtained using the "$l(l+1)/2$ power law" [47, 48] for the coefficients $A_l^m(T)$ (see section 2.5 for details). The result, shown in the inset of Fig. 2.4, is a 17% increase between 0 K and T_c. This is a sufficiently large effect that is should be observable in principle, but in practice it is preempted by the phase transformation into the fcc structure at 695 K, well below $T_c =$ 1400 K. The AHC of polycrystalline Co has been found to drop at the hcp→fcc transition temperature from $\sim$ 1320 S/cm to $\sim$ 660 S/cm [54]. These values seem inconsistent with Table 2.1.

2.8 Conclusions

In summary, we have shown by means of first-principles calculations that the intrinsic mechanism for the AHE describes quantitatively the observed strong angular dependence in hcp Co single crystals. The key role of near-degeneracies across the Fermi level was elucidated, and the AHE of polycrystalline Co films was reproduced by averaging the single-crystal Hall conductivity over all magnetization directions. Further experimental and theoretical studies of the orientation dependence of the AHE are needed. For example, very little is known about the anisotropy of the skew-scattering contribution [37].

Chapter 3

Iron

In this chapter we discuss the anomalous Hall effect in bcc iron. Yao [5] evaluated the Karplus-Luttinger expression for the anomalous Hall conductivity of (GGA) iron, with the magnetization is along $[001]$, and found a conductivity of 751 S/cm, agreeing in sign and magnitude with measurements performed by Dheer of 1029 S/cm. Since iron is a cubic material, symmetry considerations show that the anisotropy of the Hall conductivity appears at 3rd-order in the magnetization, so we expect the anisotropy of bcc iron to be small, and this has been confirmed by measurements. In refs. [55, 56], the authors were unable to observe any anisotropy of the anomalous Hall coefficient, though other measurements [34] found a large anisotropy. Here we present first-principles calculations of the anisotropy, and compare these calculations with measurements. Our calculations show that the intrinsic anomalous Hall conductivity is almost isotropic. The deviation from isotropy is too small to have been measured by the experiments of refs. [55, 56].

3.1 Method

The anomalous Hall effect calculations for iron were performed using density functional calculations in the Perdew-Burke-Ernzerhof (PBE) parameterization of the generalized gradient approximation (GGA) [40]. A relativistic norm-conserving pseudopotential was used to model the ionic core of the iron atom. Self-consistent calculations were run using `Quantum ESPRESSO` [39] version 4.0.5 with an energy cutoff of 160 Ry over a $16 \times 16 \times 16$ k-point grid. The calculation was performed in the primitive bcc unit cell using the experimental lattice constant of 5.42 a_0. The magnetization is varied by setting the initial direction of the magnetization for each run, and allowing the system to relax. The magnetization direction at the end of the self-consistent calculation differs from that of the starting magnetization by less than a degree. A separate self-consistent calculation is required for each orientation of the magnetization.

An $8 \times 8 \times 8$ k-point grid was used to generate the Wannier functions. A new set of Wannier functions is required for each orientation of the magnetization. The number of

Wannier functions (18) was chosen to match the expected number of atomic wave functions for $j = 5/2$, i.e. 2 s-orbitals, 6 p-orbitals, and 10 d-orbitals. The 18 Wannier functions were extracted from a set of 28 bands. The outer window for the disentanglement procedure used is 70 eV, so that disentanglement was performed over all the input bands, rather than a subset. The anomalous Hall effect integrations are performed on a $128 \times 128 \times 128$ grid, which is further refined over a $7 \times 7 \times 7$ grid if the Berry curvature exceeds 100 $\AA^2$.

The parameters describing the anisotropy were calculated with a multiple linear regression fit to the non-vanishing terms of the spherical harmonic expansion of the conductivity for cubic crystals (crystal class O_h). To third-order in the magnetization, the antisymmetric Hall conductivity cubic material is given by the following tensor:

$$\sigma_{23} = A_1^1 C_1^1(\theta,\phi) + A_3^1 C_3^1(\theta,\phi) + A_3^3 C_3^3(\theta,\phi) \quad (3.1)$$

$$\sigma_{31} = B_1^1 S_1^1(\theta,\phi) + B_3^1 S_3^1(\theta,\phi) + B_3^3 S_3^3(\theta,\phi) \quad (3.2)$$

$$\sigma_{12} = A_1^0 C_1^0(\theta,\phi) + A_3^0 C_3^0(\theta,\phi), \quad (3.3)$$

where the C_m^l and S_l^m are real spherical harmonics (see appendix B for definitions), θ, and ϕ are the usual polar and azimuthal angles of the magnetization relative to $[001]$, and the A_l^m are spherical harmonic coefficients. The A_l^m are not all independent. Two independent parameters (A_1^1 and A_3^1) are required for a description of the Hall conductivity tensor in cubic materials to this order.

To determine the coefficients A_l^m from the numerical data $\sigma_{ij}(\theta,\phi)$ we use multiple linear regression. The σ_{ij} are calculated for a selected set of field directions θ and ϕ, and a least squares matrix is used to determine the A_l^m from the calculated σ_{ij}. In the calculations for iron, we determine each nonvanishing A_l^m independently so the symmetry relations relating, for example, A_3^1 to A_3^3 are not satisfied exactly. Deviations from the expected symmetry arise if the Brillouin zone integration of the Berry curvature is not performed to accurately or if the self-consistent band structure is not fully converged. Allowing the non-vanishing coefficients A_l^m to vary independently, we can use the deviations from the expected symmetry to estimate errors in the conductivity. The symmetry deviations serve as an estimate of the accuracy of the conductivity calculations.

Some care is required in choosing the field directions since some choices produce a least-squares matrix that cannot determine all of the coefficients, yield A_l^m that are sensitive to small errors in the data, or data points that have no impact on the values of the fit parameters (see appendix B for further details). The field configurations chosen for the anisotropy calculations of iron are described in table 3.1.

3.2 Results

The results for our calculations are summarized in table 3.2. The relations implied by (3.1) relate the coefficients given in table 3.2. For the first-order coefficients, we have the relations $A_1^1/A_1^0 = \sqrt{2} \approx 1.414$. From the table 3.2 for $N = 256$, we find $A_1^1/A_1^0 =$

Table 3.1: Six field orientations are sufficient to calculate the anisotropy of the anomalous Hall conductivity to third-order in the magnetization. The angles θ and ϕ are the spherical coordinates of the initial magnetization. The angle θ is measured from the $[001]$-direction, and ϕ is the angle between the initial magnetization and the $[100]$-direction in the (001)-plane.

ϕ	θ
0	15
0	45
0	75
60	15
60	45
60	75

Table 3.2: Calculated values of the A_l^m, in S/cm of iron, over an $N \times N \times N$ grid in k-space. The A_l^m are related to the Hall conductivity tensor through (3.1).

N	A_1^0	A_3^0	A_1^1	A_3^1	A_3^3
64	$1053(5)$	$-24(5)$	$1508(12)$	$15(9)$	$-19(9)$
96	$1124(17)$	$-32(15)$	$1609(9)$	$22(7)$	$-65(7)$
128	$1116(5)$	$-22(5)$	$1584(16)$	$30(14)$	$-38(14)$
192	$1148(12)$	$-30(11)$	$1637(9)$	$29(7)$	$-55(7)$
256	$1155(9)$	$-30(9)$	$1647(10)$	$30(8)$	$-52(8)$

1.426(9). For the 3rd-order coefficients, the symmetry relations are $A_3^1/A_3^0 = -1$, and $A_3^3/A_3^0 = \sqrt{5/3} \approx 1.29$. Comparing these relations with our numerical calculations, we find that $A_3^1/A_3^0 = -1$, and $A_3^3/A_3^0 = 1.73$. The numerical data for the 3rd-order coefficients agrees with the expected symmetry relations in both sign and magnitude, but due to the small size of these 3rd-order coefficients, the relative uncertainty is large.

The results of these fits are shown in figure 3.1. In this figure, we compare the fits to the data, from the parameters described above, to a separate anomalous Hall conductivity calculation. The two smooth curves are the fits described above (for $N = 128$ to match the additional Hall conductivity calculations). For these calculations, the magnetization is rotated in the (001)-plane by a full 360°; σ_{zx} and σ_{yz} are calculated for each magnetization direction. To first order when $\mathbf{M}$ lies in the (001)-plane, $\sigma_{yz} \propto \cos\phi$ and $\sigma_{zx} \propto \sin\phi$. The curve labeled σ_{yz} was determined from a fit to σ_{yz} over the 6 magnetization directions described above. The coefficients for the curve describing σ_{zx} have been determined from the corresponding parameters for σ_{yz} (A_1^1, A_3^1, and A_3^3). This plot shows that the fits do an excellent job describing the behavior of the conductivity in the (001)-plane. Further, the parameterization of σ_{zx} in terms of the coefficients determined for σ_{yz} introduces no appreciable error. The symmetry relationships between σ_{yz} and σ_{zx} (analogous to (B.34), (B.33) discussed in the appendix) are maintained numerically.

In figure 3.2, there are 3 plots shown. The line labeled "3rd-order terms" contains shows only the contribution to σ_{yz} from the 3rd-order terms in (3.1). The points labeled "1st-order residual" show the difference between the calculated σ_{yz} and a *first*-order fit to this data. If the first-order fit were exact, then the residual would vanish everywhere. Any deviation from zero is attributed to a 3rd-order variation of σ_{yz} with the magnetization. The final curve, labeled "3rd-order residual" shows the difference between the complete 3rd-order fits shown in figure 3.1 and the calculation in the (001)-plane. We can see from the graphs that a 3rd-order trend is present in the data. The third-order variation is of roughly the same size as its residual. Applying a *t*-test to the data to learn whether the 3rd-order terms should be included at all, we learn that the 3rd-order terms are significant; all of the 3rd-order C-coefficients in table 3.2 are 3 to 4 standard deviations away from 0.

From the results described above, we may draw some conclusions about both the accuracy of the first-principles calculations for iron, and the behavior of the anisotropy of the Hall conductivity of iron. First, figure 3.1 shows that our fits to the conductivity tensor are sufficient to describe the behavior of the Hall conductivity over the entire magnetization sphere. Second, the numerical accuracy of our calculation is sufficient to describe the first order behavior of the anomalous Hall conductivity as the magnetization changes direction to about 1% accuracy, and the third-order variation to a relative accuracy of about 30%. We can say that the 3rd-order coefficients are nonzero, and obey the expected symmetries. Third, the anomalous hall conductivity of iron is almost perfectly isotropic. We can estimate about a 3% deviation from perfectly isotropic behavior by noting that for a cubic material, the leading term describing anisotropy is given by the 3rd-order coefficients A_3^m. Finally, we see no evidence of an observable 5th-order variation in the anomalous hall

Figure 3.1: The anomalous Hall conductivity of iron as the magnetization is rotated through the (001)-plane.

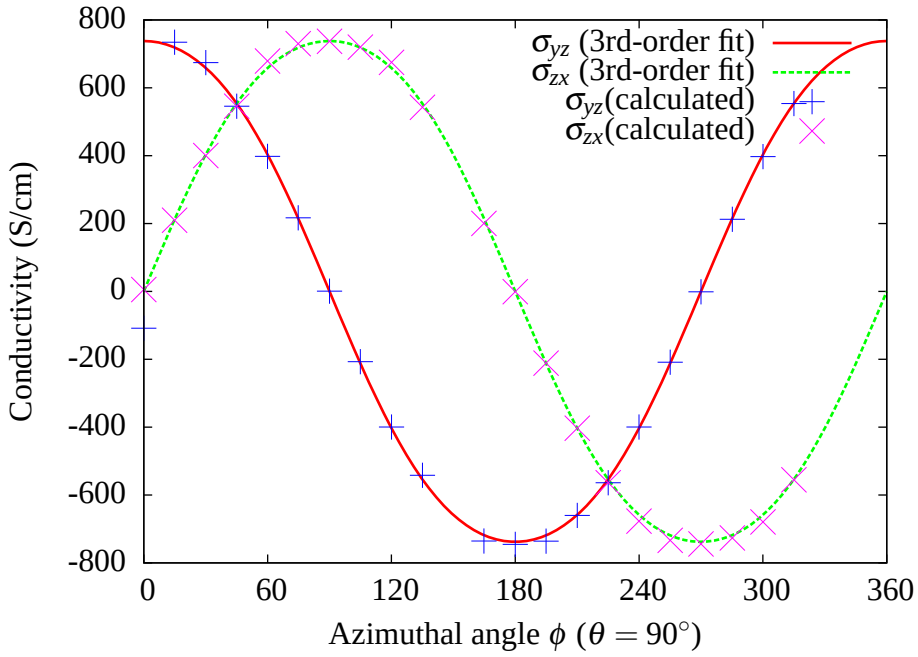

conductivity. The 3rd-order description explains almost all the variation in σ_{ij} as the magnetization changes. Although this observation seems minor, it does disagree with Hirsch and Weissman's measurement of the anisotropy [34] of the Hall effect in iron. This point is discussed further below.

3.3 The anomalous Hall effect of iron

In this section, we compare our results with other calculations and with indirect measurements of the anomalous Hall conductivity. As discussed in the introduction, the anomalous Hall coefficient is related to the resistivity through the relationship

$$R_s = a\rho + b\rho^2. \tag{3.4}$$

The coefficient b is proportional to the conductivity through the relationship $R_s = \sigma/(\mu_0 M)\rho^2$. Therefore, we can determine the conductivity directly from experimental measurements by varying the diagonal resistivity ρ. The diagonal resistivity ρ may be varied either by changing the temperature, or by doping the material with a small amount of impurities. In early experiments, when the scattering mechanisms were not as well understood, the Hall coefficients are fit an equation of the form

$$R_1 = \alpha(\rho/\rho_0)^\beta. \tag{3.5}$$

Figure 3.2: Residuals to fits of the magnetization in the (001) plane.

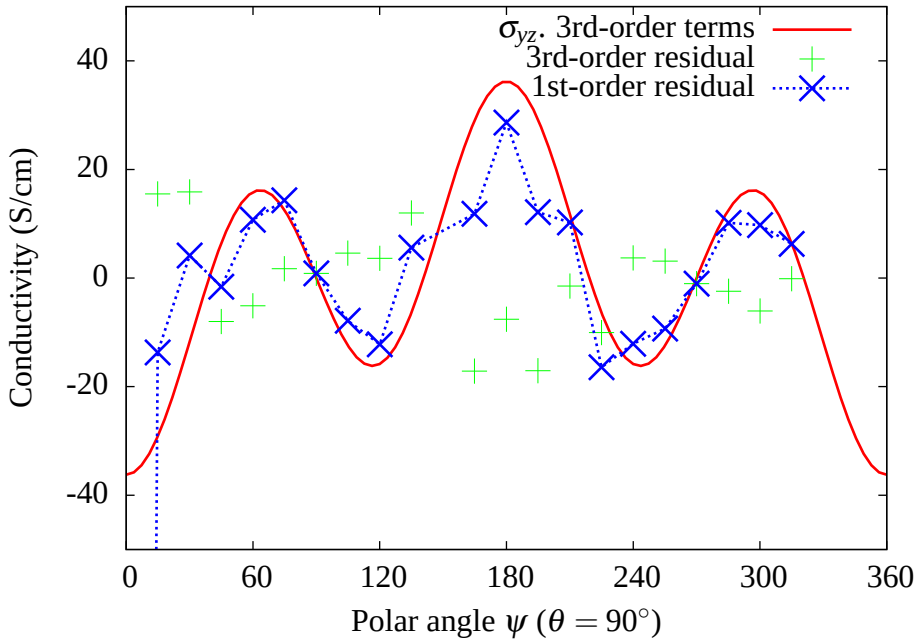

The exponent β was treated as an unknown to determine the dominant scattering mechanism. Such empirical fits can be used to estimate the conductivity, by taking $\beta = 2$ or by taking $R_1 \approx R_s$ and fitting the experimental α and β to (3.4). Kooi [57], Klaffky and Coleman [58], and Okamoto [59] report their data in this exponential form, and the results of the conductivity are described in table 3.3.

From Kooi's tables and from the results of Okamoto, we have some evidence that the anomalous Hall conductivity is, for low concentrations of silicon, independent of the silicon concentration. Okamoto plotted R_1 as a function of ρ and found that he could fit his data by a curve of the form $R_1 = 0.06 \times 10^{-10}(\rho/\rho_0)^{1.94}$ with $\rho = 10^{-8}\Omega$m. In Kooi's paper, we

Table 3.3: The anomalous Hall conductivity of iron

Description	σ (S/cm)
Side-jump [20]	100
Intrinsic [5]	751
Intrinsic [7]	750
Klaffky and Coleman [58]	1440
Dheer [60]	1029
Tian[11]	1100
Okamoto[59]	1012
Kooi[57]	926

Figure 3.3: The extraordinary Hall coefficient R_1 as a function of ρ

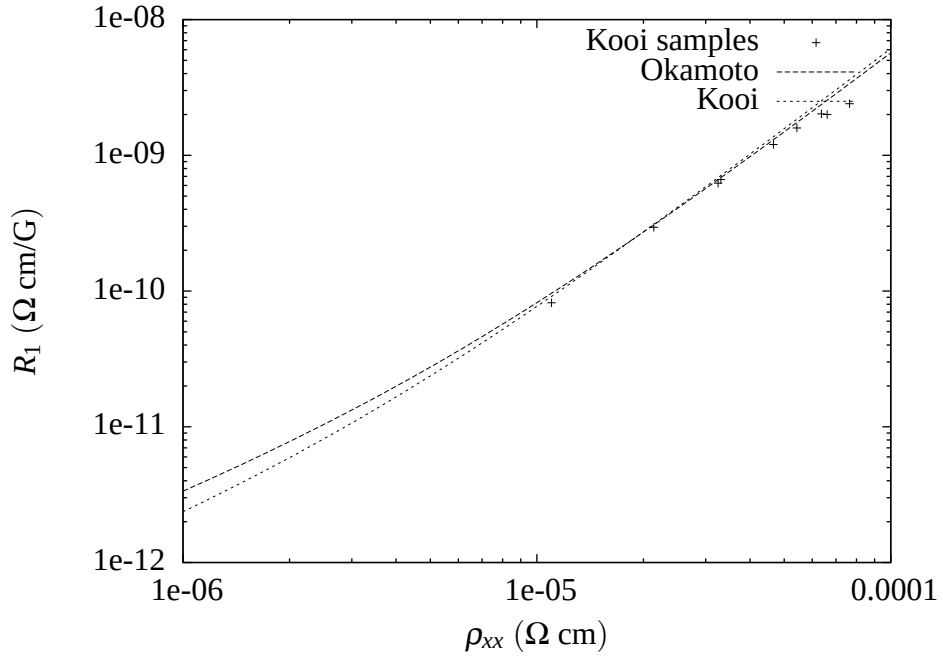

find $R_1 = 0.07 \times 10^{-10}(\rho/\rho_0)^{1.9}$ where R_1 is in Ωm/T and ρ is in Ωcm. If take $R_s \gg R_0$ we can estimate the conductivity sigma. Using the relationship $\sigma = (\mu_0 M/\rho^2)R_1$ and taking $R_1 = a(\rho/\rho_0)^\beta$, we find

$$\sigma = \frac{\mu_0 M}{\rho_0^\beta}\rho^{\beta-2}. \tag{3.6}$$

Since Okamoto found $\beta = 1.94 \approx 2$, we can then use the approximation

$$\sigma = \frac{\mu_0 M}{\rho_0^\beta}\rho^{\beta-2} \tag{3.7}$$

to estimate σ.

Note that we've taken $M = M_s$ as constant for the samples, and equal to the saturation magnetization of iron $M_s = 1.715$ A/m [25]; i.e. we are not accounting for the change in M_s due to Si doping, or the changes in M at room temperature. Doping from 1-5 percent changes the resistivity of iron by more than a few percent according to Kooi's tables, but has much less of an impact on the magnetization. Berger [20] shows similar results for R_s for other alloys. From these results (other than the Klaffky and Coleman result) we conclude that the experimental anomalous Hall conductivity σ is about 1000 S/cm.

Table 3.4: The anomalous Hall coefficient, R_s, in 10^{-10} Ωm/T for iron at room temperature, for different orientations of the magnetization **M** and primary current **J**, and the Hall coefficient along $\mathbf{M} \times \mathbf{J}$.

Current direction	Electric field component	Magnetization direction	R_s	Reference
$[100]$	$[010]$	$[001]$	4.31	Dheer
			9.70	Webster
			4.22	Tatsumoto and Okamoto
			6.0	Hirsch and Weissman
			3.74	GGA (this work)
$[111]$	$[\bar{1}10]$	$[11\bar{2}]$	4.31	Dheer
			3.88	GGA (this work)
$[001]$	$[1\bar{1}0]$	$[110]$	9.80	Webster
			4.22	Tatsumoto and Okamoto
			29.8	Hirsch and Weissman
			3.94	GGA (this work)
$[1\bar{1}0]$	$[00\bar{1}]$	$[110]$	11.4	Webster
			3.94	GGA (this work)
$[11\bar{2}]$	$[\bar{1}10]$	$[111]$	9.70	Webster
			3.98	GGA (this work)
$[\bar{1}10]$	$[11\bar{2}]$	$[111]$	3.92	Tatsumoto and Okamoto
			3.98	GGA (this work)

3.4 Anisotropy in the anomalous Hall coefficient

Table 3.4 summarizes the available measurements and calculations of the anomalous Hall coefficients at room temperature. The most recent measurements of the anisotropy of the anomalous Hall effect in iron has been performed by Dheer [60]. The first few lines of the table, with the magnetization along the $[001]$ axis, is the same arrangement used in earlier calculations of the anomalous Hall conductivity by done by Wang [7] and Yao [5]. The *ab initio* calculations agree with each other, and predict R_s to be about 30% smaller than is observed experimentally.

To measure the anisotropy of the anomalous Hall effect at room temperature, Dheer measured R_s for a second set of samples, where the magnetization and primary current were along different crystal axes. His conclusion is that the anomalous Hall effect is isotropic. Dheer estimates these R_s measurements to be accurate to about 10 percent. An *ab initio* estimate of R_s in this geometry shows that R_s should increase by about 4 percent, too small to have been detected in Dheer's experiments.

Dheer also measured the anomalous Hall conductivity in samples at 4.2 K and found that, for fields along the $[100]$ direction, R_s varied between 0.1×10^{-10} Ωm/T to 0.5×10^{-10} Ωm/T, depending on the sample purity and field orientation. We can estimate the contribution of the intrinsic mechanism at these temperatures using the scaling relationship $R_s = \sigma_{xy}\rho_{xx}^2$. Since $\rho_{298K}/\rho_{4.2K} \approx 300$ for Dheer's whiskers, and the intrinsic conductivity is independent of temperature, we find that the Berry curvature only contributes 3.49×10^{-15} Ωm/T to the Hall resistivity at these temperatures. This value is far too small to explain either the observed R_s, or the anisotropy in R_s at these temperatures. There are two probable explanations for this low temperature behavior of the AHC of iron. First is skew scattering. At 4.2 K, the samples are highly conductive, and the diagonal resistivity is small. Since $R_s \propto \rho_{xx}$ for skew scattering, but $R_s \propto \rho_{xx}^2$ for the intrinsic contribution, it is likely that the skew scattering dominates the intrinsic contribution at low temperatures. We could then interpret the low temperature measuremnts as showing that skew scattering is anisotropic at 4.2 K. The second explanation is anisotropy in the ordinary Hall Effect R_0 at low temperature. Since Dheer only measured R_1, and did not determine R_s from the low temperature measurements, we cannot distinguish these two possibilities.

Webster [55] measured the Hall coefficient R_1 in iron plates. His measurement ($R_1 = 9.7 \times 10^{-10}$ Ωm/T) disagrees in magnitude with Dheer's measurements for the same field directions. Webster's measurement with J along $[1\bar{1}0]$ found $R_s = 11.7 \times 10^{-10}$ Ωm/T, but Webster also reports that the sample was damaged while being prepared, and discards the measurement. In the other measurements for single crystals, he found that the Hall resistance for iron is isotropic. He estimates that his R_s measurements are accurate to about 2 percent. His conclusion is that the Hall effect is isotropic in crystals of iron. In our calculations, we predict a 3 to 6 percent change in R_s for iron crystals.

Tatsumoto and Okamoto [56] measured the anomalous Hall effect in samples of 1.23 % silicon iron at room temperature for 3 field configurations. Although a small change in the band structure due to the impurities could modify the anisotropy of the intrinsic contri-

bution, we saw in section 3.3 in the analysis of Kooi's data that the impurity concentration has little impact on the conductivity along the crystal axes [57]. Tatsumoto and Okamoto found that the extraordinary Hall coefficient R_1 was isotropic in their samples, but that the ordinary Hall coefficient R_0 showed some anisotropy. The ordinary Hall coefficient R_0 changes from 1×10^{-10} Ωm/T when the primary current was along the $[100]$-direction to 0.7×10^{-10} Ωm/T when the primary current was passed along the $[1\bar{1}0]$-direction. Since $R_s = R_1 - R_0$, this data indicates that R_s is anisotropic. However, it seems unlikely that an anisotropic variation of R_0 could cancel a variation in R_s to produce an isotropic R_1. The *ab initio* calculations predict that R_s for the $(1\bar{1}0) - [111]$ sample should be larger than the $(001) - [100]$ sample by 0.22×10^{-10} Ωm/T, but experimentally, R_s is smaller for the $(001) - [100]$ sample by 0.30×10^{-10} Ωm/T, due to the change in R_0 between the two samples. Tatsumoto and Okamoto with Dheer's, we see that both measurements agree that there is some anisotropy in R_s, but that they disagree about whether the anisotropy originates in R_1 or R_0.

One possible reason for the discrepancy between the Tatsumoto and Okamoto is the change in the band structure due to the silicon impurities. Although we have argued that this change should not alter the conductivity, it may be possible to simulate the effects of these impurities by varying the magnetization of the iron. This could be done directly, with a constrained magnetization calculation, or indirectly, by altering the exchange splitting of iron in the same way we have performed for nickel in 4.1.2. A second explanation for our small discrepancy with Tatsumoto and Okamoto's results is the presence of additional side-jump scattering introduced by the silicon impurities. Since we have no means of estimating the side-jump scattering, we cannot rule out this possibility.

Hirsch and Weissman [34] measured the Hall coefficients R_0 and R_1 in a rod of iron at 300 K. They passed a primary current J along the axis of the rod (the $[001]$ direction), and measured the Hall voltage perpendicular to the rod. These experiments found that the ordinary Hall coefficient for iron is $R_0 = 10.0 \times 10^{-10}\,\Omega$m/T. The anomalous Hall coefficient R_1 can be fit to the form $R_1 = a - b\cos 4\phi$, where $a = 27.9 \times 10^{-10}\,\Omega$m/T, and $b = 11.9 \times 10^{-10}\,\Omega$m/T. Using the relationship $R_s = R_1 - R_0$, we find $R_s = m_0 + m_4 \cos 4\phi$ where $m_0 = 17.9 \times 10^{-10}\,\Omega$m/T, and $m_4 = -11.9 \times 10^{-10}\,\Omega$m/T. At $\phi = 0^\circ$, when $\mathbf{M}$ is along the $[100]$ direction, Hirsch and Weissman find that $R_s = 6.0 \times 10^{-10}$ Ωm/T, about 50% larger than the measurements of either Dheer or Tatsumoto and Okamoto, listed in the first set of directions in 3.4. At $\phi = 45^\circ$, corresponding to the third set of orientations listed in table 3.4, Hirsch and Weissman find $R_s = 29.8 \times 10^{-10}\,\Omega$m/T. As shown in table 3.4, every other measurement of anisotropy in the Hall coefficients of iron concluded that the anomalous Hall effect in iron is isotropic. Given the disparity between Hirsch and Weissman's measurements and the other available measurements, the results of Hirsch and Weissman should not be taken as evidence of anisotropy of the anomalous Hall effect in iron.

Figure 3.4: The anomalous Hall coefficient R_s of iron, measured transverse to $\mathbf{M}$ and $[001]$, as the magnetization rotates through the (001)-plane. The measurements of Hirsch and Weissman [34] disagree with measurements by Tatsumoto and Okamoto [56], with measurements by Webster [55], and with *ab initio* calculations presented here.

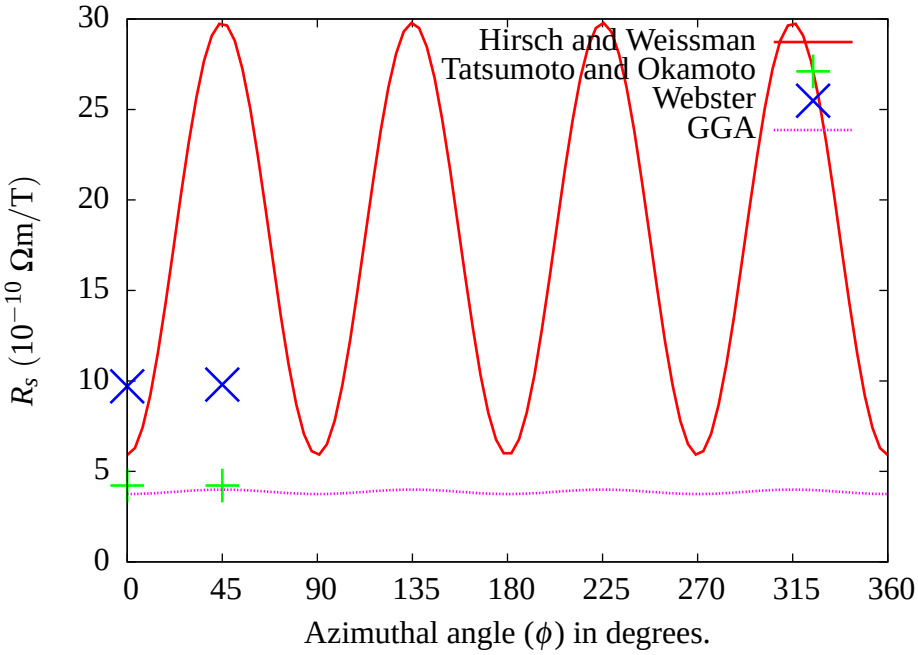

3.5 Conclusions

Our calculations for the anomalous Hall conductivity of iron show that the Hall conductivity tensor is nearly isotropic in this material. We predict deviations from perfectly isotropic behavior of a few percent, too small to have been detected in the existing experiments. This result is consistent with the findings of Dheer, with the measurements of Tatsumoto and Okamoto (though there is a small discrepancy for one sample), and those of Webster. Our results are not consistent with Hirch and Weissman's measurements for the anisotropy in iron, but as we have shown, their measurements differ by almost a factor of 10 from the other measurements of the anisotropy of the Hall coefficients in iron.

Tatsumoto and Okamoto also studied the anisotropy of the Hall coefficients while the iron sample was strained. Although we have not attempted to simulate these experiments, such simulations are possible, and would make an interesting study for future work.

Chapter 4

Nickel

This chapter describes the anomalous Hall conductivity of bulk fcc nickel. Previous *ab initio* calculations of the intrinsic Hall conductivity (with **M** along the theoretical easy axis, $[001]$) predict $R_s = -18.4 \times 10^{-10}\,\Omega$m/T [7], but measurements of the anomalous Hall coefficient in nickel show a smaller R_s. Lavine, for example, found $R_s = -5.70 \times 10^{-10}\,\Omega$m/T [61] when **M** is along the $[111]$ axis (experimental easy axis). In this chapter, we show that a semi-empirical correction to the *ab initio* calculations to improves the agreement with experiments, and make corresponding predictions of the anisotropy of R_s in nickel.

4.1 The Electronic Structure of Nickel

The standard approximations used in *ab initio* calculations, namely the local density approximation (LDA) and the generalized gradient approximation (GGA) do not accurately describe the electronic structure of fcc nickel [62]. First, the GGA predicts the exchange splitting in nickel to be 0.7 eV but experimentally the exchange splitting is only 0.3 eV. Second, the GGA predicts the width of the 3*d*-bands to be 4.5 eV but experiments find 3.7 eV. Finally, GGA predicts that a hole pocket should exist along Γ-X, corresponding to the $X_{2\downarrow}$ band, but this does not seem to agree with experiments.

There is some disagreement in the available experimental data regarding this $X_{2\downarrow}$ pocket. Hodges, Stone, and Gold performed de Haas-van Alphen measurements of Ni and did not find an orbit that matched the predicted extremal area of the second hole pocket predicted by theory[28]. Gersdorf found that it was necessary to include such a pocket to explain the magnetic anisotropy of Ni [63]. Gersdorf believed that the $X_{2\downarrow}$ band crosses the Fermi level as the magnetization direction is rotated. Kamakura et al. [64] used soft x-ray angle-resolved photoemission to map the energy bands of Ni, and found that this second hole pocket does exist, since the the $X_{2\downarrow}$ band crosses the Fermi surface along the Γ-X line.

The parameters for these calculations are as follows. The lattice constant of nickel is set to the experimental lattice constant, $3.52 \times 10^{-10}\,m$ [25]. The cutoff energy for the wave functions is 140 Ry. The initial self-consistent calculation is performed on a $16 \times$

Figure 4.1: The figures shows the band structure of Ni, along the Γ-X lines, when the magnetization lies along [001]. The left half of each plot shows a path in the [001]-direction, and the right half is taken along the [100]-direction. The energies of the bands are relative to the Fermi energy. Part (a) shows the GGA band structure, while part (b) shows the GGA bands after an empirical correction has been made to the exchange splitting of the d-bands. The bottom part of each figure shows the contribution to the Berry curvature.

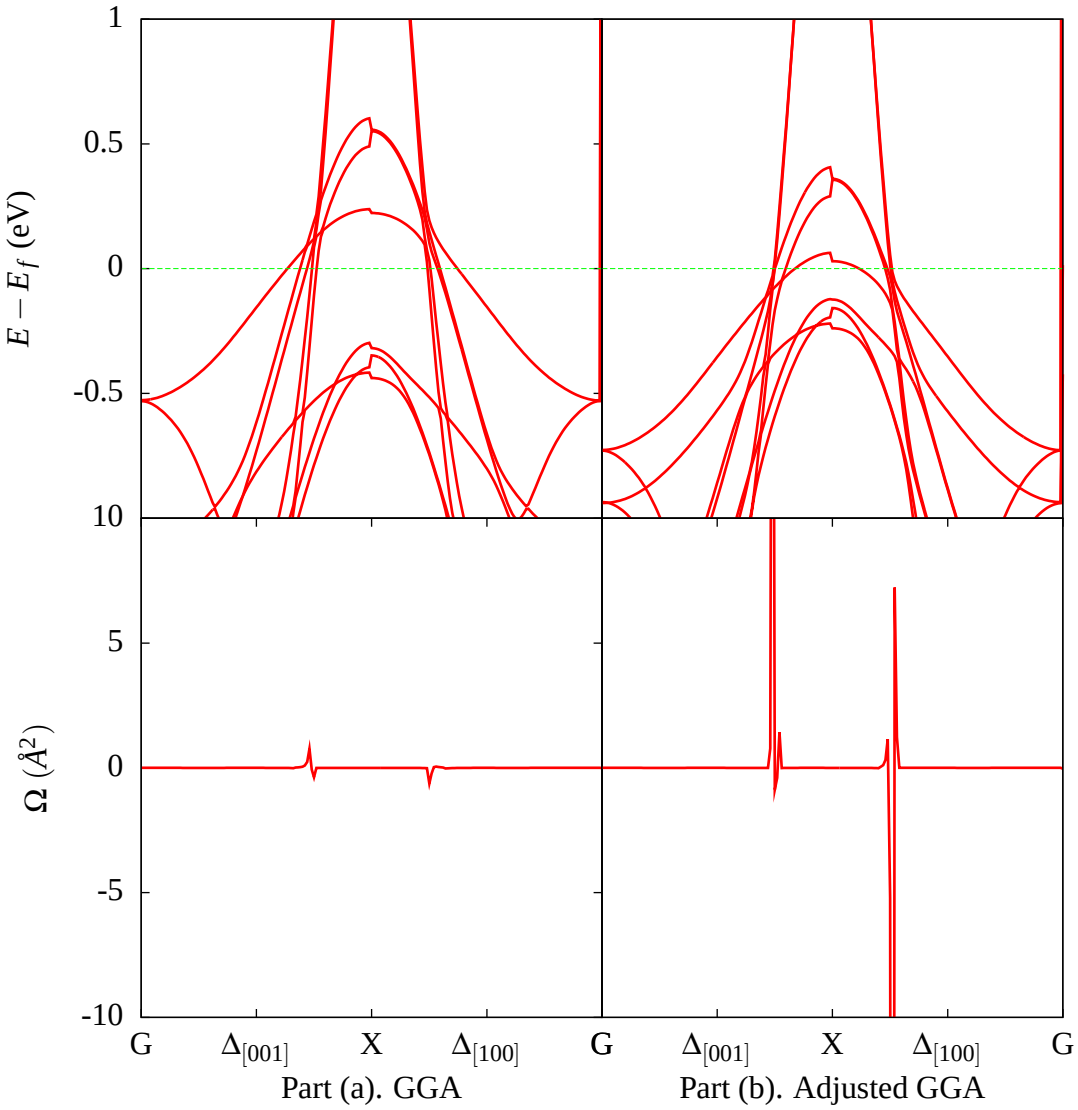

16×16 k-point grid, and the non-self-consistent calculation for the Wannier interpolation is performed on an $8 \times 8 \times 8$ k-point grid. For the initial self-consistent calculations, we use cold smearing with a broadening parameter of 0.02 Ry. The GGA band structure is plotted in figure 4.1.

A pure *ab initio* calculation of the anomalous Hall conductivity suffers from the deficiencies in the band structure introduced by the GGA. Our GGA calculations have found the intrinsic Hall conductivity of nickel [7] to be $-2281\,\mathrm{S/cm}$. This value is larger than the measured experimental conductivity $-646\,\mathrm{S/cm}$ by more than a factor of 3.

It has been known for some time that corrections to the LDA band structure of nickel can improve the theoretical exchange splitting to yield better agreement with both Fermi surface and ARPES measurements [65]. Weling and Calloway found that, in order to fit both the Fermi surface and the ARPES measurements, the exchange splitting of the t_{2g} and e_g bands are best described by splittings of 0.4 eV and 0.1 eV [66]. Liebsch applied self-energy corrections and predicted that the exchange splittings for the t_{2g} and e_g bands are 0.37 eV and 0.21 eV, in good agreement with measurements [65]. An approximate shift of the one-electron LDA eigenvalues to match the self-energy was used in to calculate the optical conductivity tensor, yielding better agreement with the experimental spectrum [67].

Of the discrepancies introduced by the GGA, the most likely to influence the Berry curvature calculations, is the error in the exchange splitting. The small energy denominator in (1.58) will be off by roughly a factor of 2 almost everywhere in the Brillouin zone. The error in the Fermi surface can be partially corrected by adjusting the exchange splitting, as we will see later. The final discrepancy, the error in the d-band width at the L-point, should not impact the calculations of the intrinsic conductivity, since transitions from bands far away from the Fermi surface do not contribute significantly to the total Berry curvature. Before describing the Hall conductivity of nickel in detail, in the next section we will describe a method for adjusting the *ab initio* exchange splitting to match the experimental results.

4.1.1 Wannier functions in Ni

Suppose we want to calculate the Brillouin-zone averaged matrix element of an operator $\hat{O}$. In terms of $O_{nm}^{(W)}(\mathbf{q})$, a matrix element between two Bloch states,

$$\langle O_{nm} \rangle_{BZ} = \frac{\Omega_{cell}}{(2\pi)^3} \int_{BZ} O_{nm}^{(W)}(\mathbf{q}), \tag{4.1}$$

and converting the integral to a sum

$$\langle O_{nm} \rangle_{BZ} = \frac{1}{N} \sum_{\mathbf{q}} O_{nm}^{(W)}(\mathbf{q}). \tag{4.2}$$

We can express (4.2) in terms of the matrix element of $\hat{O}$ between two Wannier functions $O^{(W)}_{nm}(\mathbf{R}) = \langle n\mathbf{0}|\hat{O}|m\mathbf{R}\rangle$. By definition,

$$|n\mathbf{R}\rangle = \frac{1}{N}\sum_{\mathbf{q}} e^{-i\mathbf{q}\cdot\mathbf{R}}|u^{(W)}_{n\mathbf{q}}\rangle \tag{4.3}$$

so that

$$O^{(W)}_{nm}(\mathbf{R}) = \frac{1}{N}\sum_{\mathbf{q}} e^{-i\mathbf{q}\cdot\mathbf{R}} O^{(W)}_{nm}(\mathbf{q}), \tag{4.4}$$

and therefore, at $\mathbf{R} = \mathbf{0}$

$$O^{(W)}_{nm}(\mathbf{0}) = \frac{1}{N}\sum_{\mathbf{q}} O^{(W)}_{nm}(\mathbf{q}). \tag{4.5}$$

Comparing (4.5) with (4.2), we see that

$$\langle O_{nm}\rangle_{BZ} = O^{(W)}_{nm}(\mathbf{0}) = \langle n\mathbf{0}|\hat{O}|m\mathbf{0}\rangle. \tag{4.6}$$

Equation (4.6) shows that the matrix element between two Wannier functions at $\mathbf{R} = 0$ is the Brillouin-zone average of the matrix element between the corresponding Bloch functions. In what follows, we will use this result to analyze the band structure of nickel in terms of Wannier functions.

Table 4.1 lists the average energies and spins of some typical Wannier functions in nickel. These Wannier functions were constructed from an *ab initio* calculation of nickel, with the magnetization tilted 15° from [001]. We can identify two groups of Wannier functions: a group of 8-dimensional sp^3 hybridized bands, and a group of 10-dimensional space of d-bands. These groups can be further classified into spin-up and spin-down states. Although the Wannier localization maintains the orbital character of these bands, the localization procedure is less sensitive to the spin character of the states; the resulting Wannier functions are a mix of spin-up and spin-down states. In this calculation, the magnetization is tilted by 15° from the [001]-direction. The average spin of the Wannier functions aligned along the magnetization direction agrees with the component of the spin along direction, $\sigma_z = \cos 15^\circ \approx 0.9659$.

Looking closer at the d-bands we can see that they split are composed of 2 sets of subbands, a 3-fold degenerate subband and a doubly degenerate subband. We interpret the 3-dimensional subband as t_{2g} orbitals, and the 2-dimensional subband as e_g orbitals. The t_{2g} orbitals show an exchange splitting of 0.79 eV and the e_g orbitals are split by 0.57 eV. Also note that the splitting for the sp^3 orbitals is only 0.03 eV. Overall, the initial Wannier functions used here are consistent with a description from a tight-binding model.

4.1.2 Modifying the exchange splitting in Ni

We can address some of the deficiencies in the GGA description of Ni by modifying the exchange splitting of the d-bands. The Wannier formalism gives us a framework for

Table 4.1: Properties of the Wannier functions of GGA nickel, calculated with the magnetization tilted 15° from the *z*-axis. The label *n* identifies the corresponding band, in no particular order. The column labeled $\langle H_{nn} \rangle_{BZ}$ lists the Brillouin-zone average energy of the band in eV. The Fermi energy is 13.88 eV. The column labeled dim shows the number of bands with average energies within 1 eV of each other. We can decompose the *d*-bands into e_g and t_{2g} states according to their degeneracy. The *d*-band splitting of the Wannier functions corresponds to octahedral symmetry.

n	id	dim	$\langle H_{nn} \rangle_{BZ}$ (eV)	$\langle S^z_{nn} \rangle_{BZ}$ ($\hbar/2$)
1	sp^3	8	26.2423	0.9657
2	sp^3	8	26.2421	0.9658
3	sp^3	8	26.2423	0.9657
4	sp^3	8	26.2421	0.9658
5	e_g	10	12.7277	0.9659
6	t_{2g}	10	12.8202	0.9659
7	t_{2g}	10	12.8202	0.9659
8	e_g	10	12.7279	0.9659
9	t_{2g}	10	12.8203	0.9659
10	sp^3	8	26.2160	-0.9658
11	sp^3	8	26.2161	-0.9658
12	sp^3	8	26.2160	-0.9658
13	sp^3	8	26.2161	-0.9658
14	e_g	10	12.1557	-0.9659
15	t_{2g}	10	12.0271	-0.9659
16	t_{2g}	10	12.0271	-0.9659
17	e_g	10	12.1550	-0.9659
18	t_{2g}	10	12.0271	-0.9659

doing so. We saw in the previous section that a naive localization of the Wannier functions produces two sets of Wannier functions polarized along the magnetization direction, and that these Wannier functions can be interpreted in terms of atomic wave functions. These properties allow us to implement a correction to the *ab initio* band structure to adjust the d-band splitting.

We add a term to the self-consistent Hamiltonian H_0 that shifts the average energies of the d-bands by an amount Δ:

$$H = H_0 + H_d \tag{4.7}$$

where

$$H_d(\mathbf{R}) = \frac{1}{2}\left(P_{d,\downarrow} - P_{d,\uparrow}\right)\delta_{R,0}\Delta, \tag{4.8}$$

and $P_{d,n}$ are projection operators onto the d-band subspace along a direction $\hat{n}$. Due to the form of these projection operators, we must take some care in identifying the spin-up and spin-down Wannier functions, since the Wannier functions are not entirely polarized along the magnetization direction. Although table 4.1 shows that the Wannier functions are nearly spin-polarized, each Wannier function has a small component of the opposite spin. This component is large enough problems in the exchange splitting described by (4.8).

We can force the Wannier functions to have a definite spin polarization by requiring them to be eigenfunctions of a spin-operator. There is, however, a severe drawback to this approach. The eigenvalues of the spin operator in a ferromagnetic system are almost entirely ± 1. Since there are only two eigenvalues, the spin eigenfunctions mix the spin-polarized s, p, and d-like Wannier functions. We then lose the ability to match the Wannier functions with atomic states. If we cannot identify the d-states, then we cannot adjust their exchange splitting. An additional constraint on the eigenfunctions is required.

We choose to eliminate the spin matrix elements only between states of similar character. States of similar character are identified by choosing a small energy window. If the average energy of any two states differs by less than the window threshold, the states are said to be of the same character. The spin-operator is then diagonalized over the space of Wannier functions of a given character. The energy window must be chosen small enough that the hybridized s and p Wannier functions do not hybridize with the d, but large enough that all 10 d-states are identified as having similar character. The results of such an analysis are shown in table 4.1, where we list the dimension of each observed subspace. We then rotate the Wannier functions so that the spin operator is diagonal in each subspace. With this procedure, an arbitrary rotation within each subspace is still allowed, but the overall orbital character of the states is preserved. The resulting Wannier functions will be termed *spin purified* Wannier functions. Table 4.2 shows how spin purification modifies the Wannier functions of Ni.

The success of the exchange adjustment to the Hamiltonian requires a proper identification of the spin-up and spin-down d-bands. The results shown in table 4.1 seem to show that the Wannier localization is able to properly identify the spin-polarized states, so it might be possible to omit the spin purification step and use the original self-consistent

Table 4.2: The Wannier functions of 4.1 after spin purification and adjusting the exchange splitting of the d-bands. The s and p Wannier functions are no longer hybridized. The d-band Wannier functions now have a lower (square planar) symmetry.

n	id	$H_{nn}(\mathbf{0})$ (eV)	$H_{0,nn}(\mathbf{0})$ (eV)	Δ (eV)
1	s	20.9721	20.9721	0
2	p	28.0510	28.0510	0
3	p	27.8760	27.8760	0
4	p	27.9636	27.9636	0
5	$d_{x^2-y^2}$	12.3946	12.1946	0.2
6	d_{yz}	12.1632	11.9632	0.2
7	d_{z^2}	12.2622	12.0622	0.2
8	d_{xy}	12.3453	12.1453	0.2
9	d_{xz}	12.1641	11.9641	0.2
10	p	27.8766	27.8766	0
11	p	27.9594	27.9594	0
12	p	28.0432	28.0432	0
13	s	21.0913	21.0913	0
14	d_{z^2}	12.5862	12.7862	-0.2
15	$d_{x^2-y^2}$	12.6822	12.8822	-0.2
16	d_{xz}	12.5377	12.7377	-0.2
17	d_{yz}	12.5334	12.7334	-0.2
18	d_{xy}	12.6389	12.8389	-0.2

Table 4.3: Exchange splitting of the Ni d-bands, in eV. The experimental results are taken from [68]. The mean exchange splitting is taken from table 4.1. The exchange splitting at the L-point was found from the band structure.

		L	mean
t_{2g}	GGA	0.87	0.82
	Adjusted GGA	0.47	0.42
	experimental	0.33	
e_g	GGA	0.68	0.59
	Adjusted GGA	0.29	0.19
	experimental	0.17	

Wannier functions in the adjusted Hamiltonian (4.7). If this were possible, we could vary the exchange splitting of the e_g and t_{2g} states independently. We attempted this in some early experiments. The results, while promising if the magnetization lies along $[001]$, as we rotate the magnetization along other directions, the resulting band structures are unreliable. The size of the average GGA d-band exchange splitting identified by this procedure fluctuated by large amounts as the magnetization was changed, even though there was no such change in the original self-consistent GGA exchange splitting.

4.2 The Anomalous Hall Conductivity and the Exchange Splitting

Table 4.2 shows the exchange splitting of the d-bands when $M \parallel [111]$. The L column shows the exchange splitting when measured at the L point in the Brillouin zone, and the mean column shows the exchange splitting determined directly from the Wannier function Hamiltonian $H(\mathbf{R})$ at $\mathbf{R} = \mathbf{0}$. The table shows that the mean exchange splitting overestimates the exchange splitting at the L point by 0.05 eV to 0.10 eV. In comparison with the experimental values, the adjusted GGA exchange at the L point is too large by between 0.12 eV and 0.14 eV.

A band structure calculated using the adjusted exchange splitting is shown in figure 4.2 for two different orientations of the magnetization: $[001]$ and $[111]$. On rotating the magnetization, much of the band structure remains unchanged, but there are some regions near the X-point and the L-point where the energy bands differ noticeably. The d-band width, measured at the L-point, remains unchanged from the uncorrected GGA value of 4.5 eV.

Part (b) of Figure 4.1 shows the behavior of the adjusted bands near the X-point. The $X_{2\downarrow}$ band still crosses the Fermi surface, but the band is closer to the Fermi level than for the uncorrected GGA band structure. If we demand that the $X_{2\downarrow}$ Fermi surface in figure 4.1 agree with Gersdorf's suggestion for the magnetic anisotropy, and the results of Bunemann et al., then an additional adjustment to the exchange splitting of about 0.04 eV is required.

Figure 4.2: The band structure and Berry curvature of fcc Ni when an empirical correction has been applied to match the experimental exchange splitting. Two orientations of the magnetization ([001] and [111]) are shown here. The energies of the bands are less sensitive to the orientation of the magnetization than the intrinsic Hall conductivity. The largest contributions to the intrinsic Hall conductivity are in the vicinity of the X and L points.

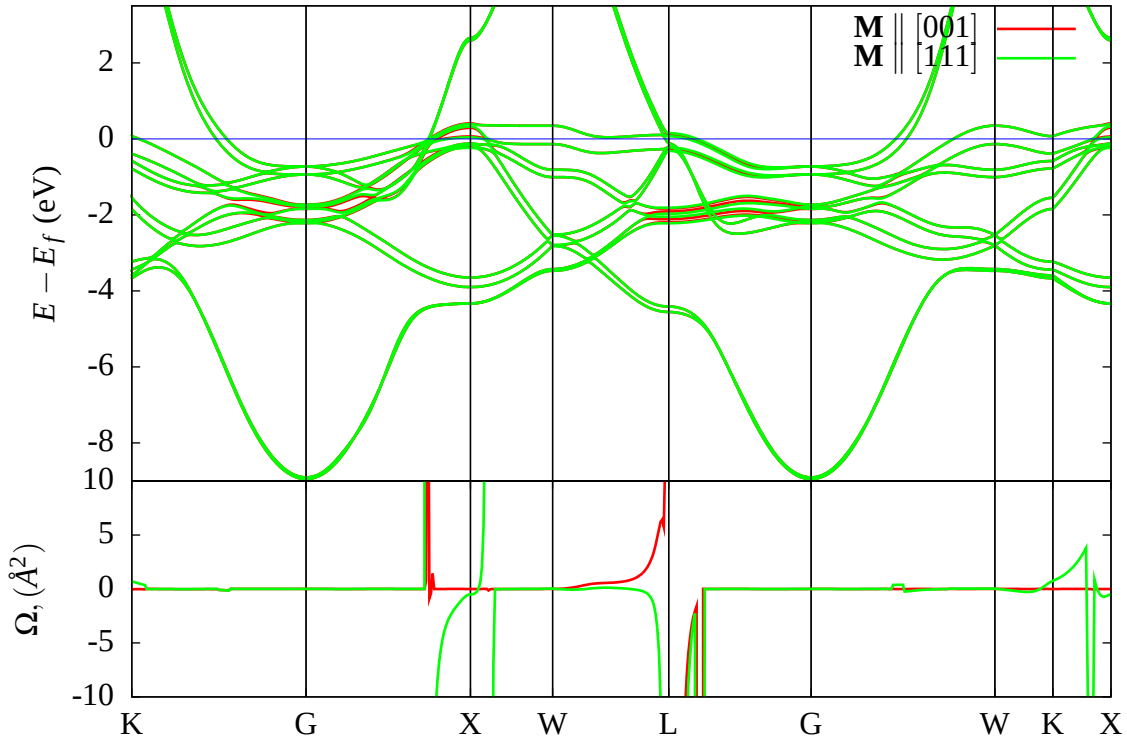

There remain some discrepancies with the experimental band structure. The spin purification procedure destroys the hybridization of the d-band Wannier functions into e_{2g} and t_{2g} orbitals. If we were able to maintain the hybridization during the spin purification, then it would be possible to separately adjust the exchange splitting of each orbital, to match the experimentally observed difference in exchange splitting between the e_{2g} and t_{2g} orbitals.

In figures 4.3 and 4.4 we show the effects of varying the exchange splitting on the average spin moment and the anomalous Hall conductivity. Figure 4.3 shows the average spin magnetic moment as the exchange splitting is modified. The spin moment varies smoothly and close to linearly, with the exchange splitting. Figure 4.3 shows how the conductivity varies with exchange splitting. As we reduce the exchange splitting from the GGA value of 0.73 eV to 0.33 eV the anomalous Hall conductivity drops from $-2281\,\mathrm{S/cm}$ to $-1571\,\mathrm{S/cm}$. Although this is still far from the experimental value, $-700\,\mathrm{S/cm}$, the adjusted GGA exchange splitting eliminates half of the discrepancy with the experimental

Figure 4.3: The spin magnetic moment of Ni as a function of the exchange splitting.

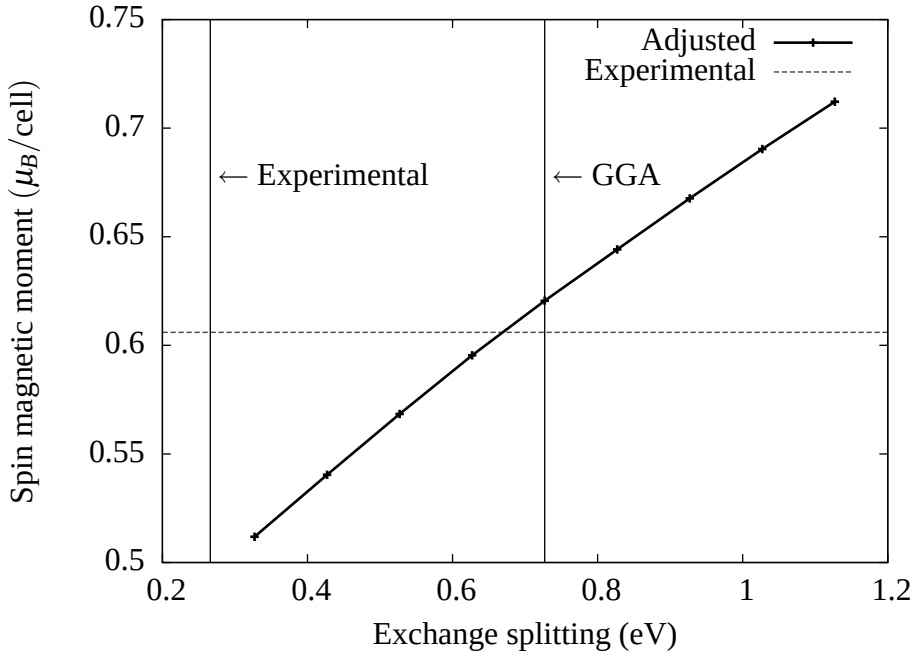

conductivity.

4.3 Temperature Dependence of the Intrinsic Hall Conductivity

Although the intrinsic part of the anomalous Hall conductivity is determined from the band structure, and not from temperature dependent scattering processes, the intrinsic Hall conductivity becomes temperature dependent when we allow the occupancy of the bands to vary. While previous work in iron [5] has shown that the intrinsic temperature dependence

Table 4.4: The anomalous Hall coefficient R_s in Ni

R_s $(10^{-10}\,\Omega\text{m/T})$	Reference
-4.54	Hiraoka
-5.70	Lavine
-5.76	Volkenshtein
-18.4	Wang (GGA)
-18.4	This work (GGA)
-11.7	This work (adjusted GGA)

Figure 4.4: The intrinsic Hall conductivity σ_{xy} of Ni as a function of the exchange splitting.

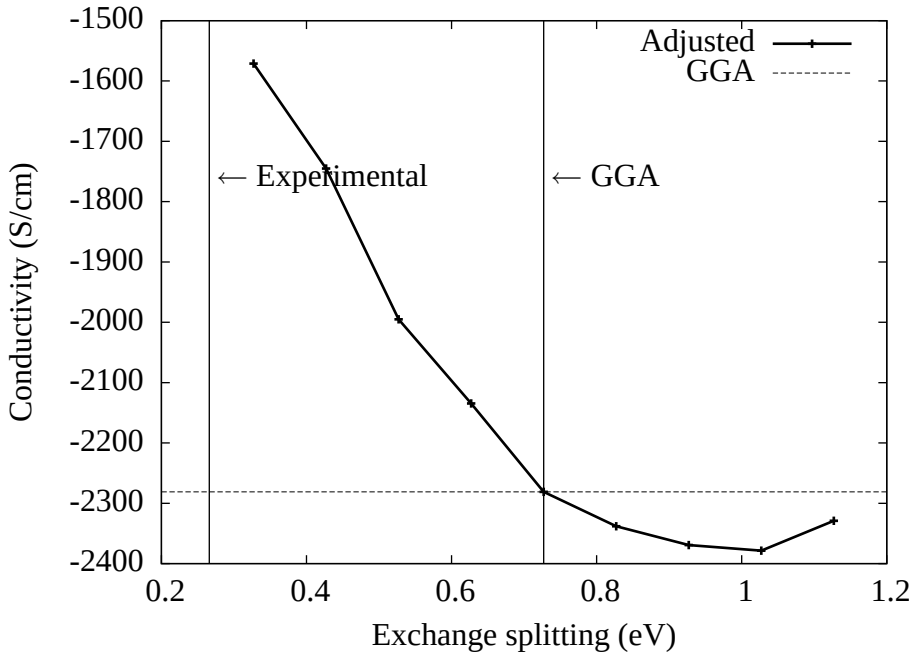

is small, this may not be the case for nickel. In nickel, it has been argued that the proximity of the *d*-bands to near the Fermi level affects the magnetic anisotropy [28]. Since the magnetic anisotropy is also a function only of the band structure and occupation, similar temperature dependence may occur for the intrinsic Hall conductivity.

We can estimate the temperature dependence of the intrinsic part of the anomalous Hall conductivity by using a Fermi-Dirac distribution in the expression for the anomalous Hall conductivity, (1.1). This model of the temperature dependence is highly simplified, taking into account only the changes in occupation of the electrons and neglects effects from the long-wavelength thermal fluctuations discussed in section 2.7. The results are plotted in figure 4.3. The temperature dependence of σ is roughly independent of the magnetization direction. Orienting the magnetization along [111] produces almost the same temperature dependence as *M* along [100]. The GGA predicts that the conductivity should decrease in magnitude by about 400 S/cm as the temperature rises from 200 K to 600 K. The adjusted GGA predicts an increase of only 150 S/cm over the same region. Both models predict that the conductivity should increase in magnitude from 0 K to 150 K.

4.4 Orientation Dependence

The orientation dependence of the anomalous Hall conductivity in Ni has been measured by Hiraoka. Hiraoka modeled his data in terms of a 5th-order expression for the conductivity. To compare the *ab initio* data with Hiraoka's experimental data, we use a

Figure 4.5: Temperature dependence of the intrinsic Hall conductivity

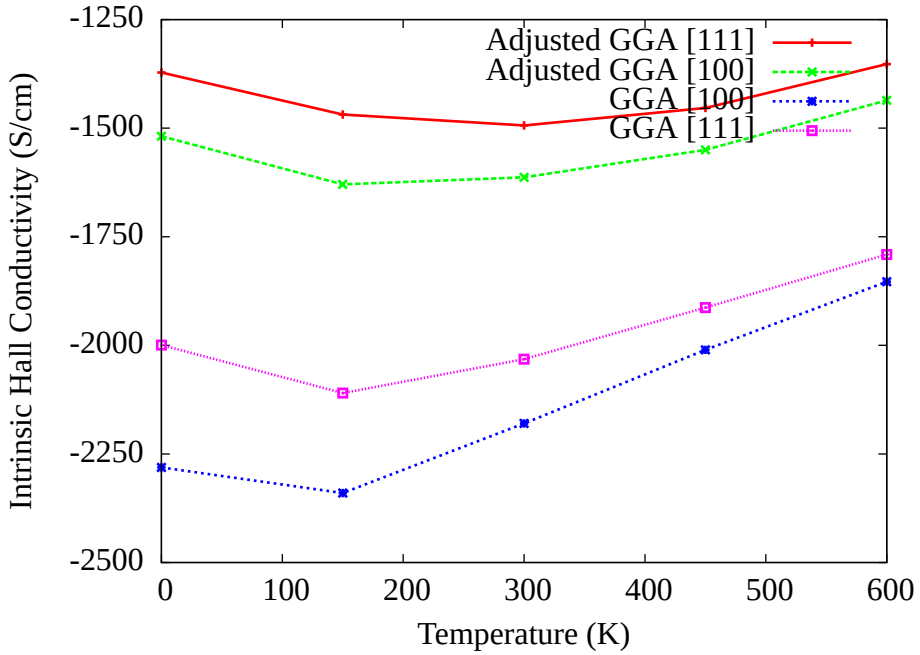

similar 5th-order expansion. By symmetry, the nonvanishing terms of the conductivity are given by:

$$\sigma_{23} = A_1^1 C_1^1(\theta,\phi) + A_3^1 C_3^1(\theta,\phi) + A_3^3 C_3^3(\theta,\phi) + A_5^1 C_5^1(\theta,\phi) + A_5^3 C_5^3(\theta,\phi) + A_5^5 C_5^5(\theta,\phi) \quad (4.9)$$

$$\sigma_{31} = B_1^1 S_1^1(\theta,\phi) + B_3^1 S_3^1(\theta,\phi) + B_3^3 S_3^3(\theta,\phi) + B_5^1 S_5^1(\theta,\phi) + B_5^3 S_5^3(\theta,\phi) + B_5^5 S_5^5(\theta,\phi) \quad (4.10)$$

$$\sigma_{12} = A_1^0 C_1^0(\theta,\phi) + A_3^0 C_3^0(\theta,\phi) + A_5^0 C_5^0(\theta,\phi) + A_5^4 C_5^4(\theta,\phi). \quad (4.11)$$

The coefficients given above are not all independent. There are 4 linearly independent coefficients: A_1^0, A_3^0, A_5^0, and A_5^4. We can relate the coefficients of σ_{23} to those of σ_{12} with the relations:

$$A_1^1 = \sqrt{2} A_1^0 \quad (4.12)$$

$$A_3^1 = -\frac{1}{2}\sqrt{3} A_3^0 \quad (4.13)$$

$$A_3^3 = \frac{1}{2}\sqrt{5} A_3^0 \quad (4.14)$$

$$A_5^1 = \frac{1}{8}\sqrt{30} A_5^0 + \frac{1}{8}\sqrt{21} A_5^4 \quad (4.15)$$

$$A_5^3 = -\frac{1}{8}\sqrt{35} A_5^0 + \frac{9}{16}\sqrt{2} A_5^4 \quad (4.16)$$

$$A_5^5 = \frac{3}{8}\sqrt{7} A_5^0 + \frac{1}{16}\sqrt{10} A_5^4. \quad (4.17)$$

Relations for the nonvanishing B_l^m are given in appendix B. Unlike the 3rd-order case, where σ_{12} is independent of the azimuthal angle ϕ, the appearance of the $m = 4$ term A_5^4 shows that σ_{12} can now vary as ϕ is rotated.

To calculate the coefficients A_l^m to this order we again vary the magnetization direction over the sphere and use a least squares fit to determine the A_l^m from the σ_{ij}. We vary both θ and ϕ independently over a uniform $N \times 2N$ grid on the surface of the sphere such that $\phi_k = \pi k/N$ for $k = 0...2N-1$ and $\theta_j = (k+1/2)\pi/N$ for $k = 0...N-1$, where the $1/2$ is introduced to avoid sampling at the poles. Such a grid of $2N^2$ samples is sufficient to determine a spherical harmonic expansion of order $N-1$ [69].

Although computationally demanding, this procedure is fairly robust. The values of the coefficients do not depend on the form of the expansion (i.e. the covariance is small), and the values of the coefficients are not more sensitive to some data points than others. Also, this procedure allows us to estimate the accuracy of our calculations by testing other models (i.e. 3rd-order models, or models that violate the expected symmetry) of the data.

4.4.1 5th-order dependence

Our results for the Hall conductivity anisotropy are summarized in tables 4.5 and 4.6. In table 4.5 we show the coefficients describing σ_{12} over the magnetization sphere in both the GGA approximation, and after using our adjusted exchange splitting. In table 4.6 we show the parameters for σ_{23}. Using the relations (4.12)-(4.17), we can calculate the discrepancies between the calculated σ_{12} and σ_{23}, as an additional estimate of the error in the *ab initio* calculations.

Table 4.7 shows the results of this calculation. The columns represent the difference in the corresponding coefficient, For example, the A_1^1 column shows $A_1^1 - \sqrt{2}A_1^0$, and from (4.12) each column in the table should be zero. The uncertainties listed in the table were propagated from tables 4.5 and 4.6. The discrepancy from symmetry in the first order and third order GGA expansion are all less than 20 S/cm, and the discrepancies increase as the order of the expansion increases. The discrepancy in the fifth order expansion for the GGA are almost half the magnitude of the corresponding coefficients, indicating that we have run into a limit from numerical accuracy. For the adjusted GGA, we have better agreement between the two components overall, but the first order-discrepancy is much larger. While somewhat troubling, the discrepancy of 20 S/cm is only about 1% of the magnitude of A_1^1, which is -2817 S/cm. The A_5^m in the adjusted GGA agree to within 2 standard deviations, the worst being A_5^3 which differs by 12 ± 6 S/cm.

The A_l^m are proportional to the Hall conductivity, averaged over all magnetization angles. The adjusted GGA results show that the average Hall conductivity $\sqrt{(1/2)}A_1^0 = 1416\,\mathrm{S/cm}$, while its value for $\mathbf{M} \parallel [001]$ of $\sigma = 1571\,\mathrm{S/cm}$. Since A_1^0 is an average over all angles of the magnetization, it can serve as an estimate the Hall conductivity of a polycrystalline sample. The anomalous Hall coefficient R_s of a polycrystalline sample should be about 11% smaller than that of a monocrystalline sample, when all fields are along the

Table 4.5: Spherical harmonic coefficients A_l^m in S/cm describing σ_{12} in Ni.

	A_1^0	A_3^0	A_5^0	A_5^4
GGA	$-2890(8)$	$-271(8)$	$52(7)$	$105(14)$
Adjusted GGA	$-2007(3)$	$-104(4)$	$23(3)$	$52(6)$

Table 4.6: Spherical harmonic coefficients A_l^m in S/cm describing σ_{23} in Ni.

	A_1^1	A_3^1	A_3^3	A_5^1	A_5^3	A_5^5
GGA	$-4091(5)$	$251(4)$	$-318(5)$	$43(3)$	$82(4)$	$113(5)$
Adjusted GGA	$-2819(5)$	$85(4)$	$-101(5)$	$50(3)$	$11(4)$	$35(5)$

cubic axes. The third-order coefficients A_3^m are large, on the order of 100 S/cm, indicating that the anisotropy of nickel should be large enough to measure accurately. The fifth-order A_5^m are small, only a few percent of the A_1^m. Although the calculations here are unable to determine the A_5^m accurately, the discussion in the preceding paragraph shows that these numbers should be accurate in both sign and order of magnitude.

4.5 Discussion

Hiraoka measured the anomalous Hall conductivity in strips of Ni cut at different orientations of the crystal axes in order to measure the anisotropy of the anomalous Hall effect. Hiraoka performed these measurements at two different temperatures: liquid nitrogen (77 K) and room temperature (297 K). Hiraoka fit his data to the following form:

$$R_s = C + C_1 s + C_2 t \tag{4.18}$$

where $s = \alpha_1^2\alpha_2^2 + \alpha_2^2\alpha_3^2 + \alpha_3^2\alpha_1^2$ and $t = \alpha_1^2\alpha_2^2\alpha_3^2$, and the α_i are the direction cosines of the magnetization. The constant term C is isotropic, and equal to the magnitude of the Hall coefficient when the magnetization is along [001]. The next two terms C_1 and C_2. are proportional to the third-order and fifth-order anisotropy in ρ_H. These coefficients are related to the A_l^m as follows:

$$C = \frac{\rho_{xx}^2}{\mu_0 M_s}\sqrt{\frac{1}{2\pi}}\left(\sqrt{3}A_1^0 + \sqrt{7}A_3^0 + \sqrt{11}A_5^0\right) \tag{4.19}$$

Table 4.7: Discrepancy in the A_l^m, in S/cm, of Ni from cubic symmetry.

	A_1^1	A_3^1	A_3^3	A_5^1	A_5^3	A_5^5
GGA	$3(12)$	$-17(8)$	$14(10)$	$53(13)$	$-37(7)$	$-41(11)$
Adjusted GGA	$-20(7)$	$5(5)$	$-15(6)$	$-4(6)$	$13(5)$	$-1(7)$

$$C_1 = -\frac{\rho_{xx}^2}{\mu_0 M_s}\frac{1}{16\sqrt{\pi}}\left(40\sqrt{14}A_3^0 + 49\sqrt{22}A_5^0 - 3\sqrt{385}A_5^4\right) \quad (4.20)$$

$$C_2 = \frac{\rho_{xx}^2}{\mu_0 M_s}\frac{63}{16}\sqrt{\frac{11}{\pi}}\left(3\sqrt{2}A_5^0 - \sqrt{35}A_5^4\right) \quad (4.21)$$

The three coefficients C, C_1 and C_2 are linear combinations of the 4 A_l^m. It is not possible to calculate the A_l^m directly from the experimental data, since the 3 available experimental coefficients are not sufficient to determine the 4 unknown A_l^m.

In the discussion that follows, to calculate the Hall coefficient from the conductivity, we use the usual relation $R_s = \sigma_{AHC}\rho_{xx}^2/(\mu_0 M_s)$. At room temperature $\rho_{xx} = 7\times10^{-8}\,\Omega\,\mathrm{m}$ and $M_s = 0.482\,\mathrm{MA/m}$. At 77 K, we have $\rho_{xx} = 0.55\times10^{-8}\,\Omega\mathrm{m}$ [70] and $M_s = 0.509\,\mathrm{MA/m}$. These values, though reasonable, are a possible source of error when converting the theoretical conductivity to the experimental Hall coefficient, but are consistent with those used by Hiraoka in analyzing his samples [19]

Table 4.8 and 4.9 compare our estimates of the R_s from the conductivities described in the previous section with the experimentally observed R_s. The coefficient C should be equal to the value shown in table 4.4. Again, at room temperature, both the GGA and adjusted GGA predict a Hall coefficient C that is too large compared with experiments. Also, in that same table, note that Hiraokas room temperature Hall coefficient is smaller than both the measurements of Lavine and the measurements of Volkenshtein at 297 K.

Moving to C_1, the third-order anisotropic term, the GGA predicts between $9.9\times10^{-10}\,\Omega$m/T and $12.5\times10^{-10}\,\Omega$m/T, while the adjusted GGA predicts between $2.7\times10^{-10}\,\Omega$m/T and $3.8\times10^{-10}\,\Omega$m/T depending on which parameterization we use. Adjusting the GGA exchange splitting decreases C_1, but not so much to cause the sign to reverse, so that both the GGA and the adjusted GGA predict a C_1 to be positive, in contradiction with Hiraokas measurements at room temperature. The magnitude of the adjusted GGA C_1 is also too large, much like the isotropic prediction of the isotropic C term. Finally, the fifth-order C_2 term is found theoretically to be about $-9\times10^{-10}\,\Omega$m/T, which agrees in sign with Hiraokas measurement of $-3.8\times10^{-10}\,\Omega$m/T, but is too large at room temperature, by about a factor of 2.

We can also compare to Hiraoka's measurements at 77 K. Here the calculated intrinsic conductivities are too small by about a factor of 2. The sign of C_1 still disagrees with Hiraoka's measurements, while the sign of C and C_2 agree with the measurements. The anisotropy does not change sign either in the theory or in the experiments. At these temperatures, unlike room temperature, the adjusted GGA (as well as the GGA values, not shown) are now smaller compared to the experimental values, by about a factor of 3.

Figures 4.6 and 4.7 compare the anomalous Hall coefficient R_s calculated from Hiraoka's fit to his experimental data, a measurement reported by Lavine [61], and the calculation by Wang [7], along with our results. The plots show that these results are consistent with previous theoretical calculations, and that Hiraoka's experiments agree with Dheer's measurements along the $[001]$ direction at room temperature.

Thomas and Marsocci [71] presented an argument based on perturbation theory, and

Table 4.8: Anisotropy of the anomalous Hall coefficient R_s of Ni at 297 K in $10^{-10}\,\Omega$m/T

	C	C_1	C_2	Remarks
GGA	-18.4	12.5	-30.6	σ_{23}
	-18.2	11.5	-27.5	σ_{31}
	-17.9	9.9	-23.8	σ_{12}
Adjusted GGA	-11.6	2.7	-8.4	σ_{23}
	-11.6	2.8	-8.0	σ_{31}
	-11.9	3.8	-12.6	σ_{12}
Experimental	-4.5	-1.8	-3.8	Hiraoka, 297 K
	-9.5	-6.3		Chen and Marsocci

Table 4.9: Anisotropy of the anomalous Hall coefficient R_s of Ni at 77 K in $10^{-12}\,\Omega$m/T

	C	C_1	C_2	Remarks
GGA	-6.8	1.6	-4.9	σ_{23}
	-6.8	1.7	-4.7	σ_{31}
	-6.9	2.2	-7.4	σ_{12}
Experimental	-13.9	-4.9	-14.2	Hiraoka, 77 K

estimated the magnitude of the anisotropy in R_1 to be about 3%. Our results for the adjusted GGA show that σ varies by about 3.5%, and about 6.7% for the GGA. Chen and Marsocci [72] measured the anisotropy of the Hall coefficients in thin films of Ni, but they conclude that their measurements are unreliable, due to the difficulty of correcting for the demagnetizing-field in the sample. They fit the Hall resistivity ρ_{12} to a third order expression, and found that $C = -9.5 \times 10^{-10}\Omega$m/T and $C_1 = -6.3 \times 10^{-10}\Omega$m/T. These results agree with Hiraoka's results, in that C_1 and C have the same sign, but the Hall coefficient R_1 is too large by almost a factor of 2. Also, they note that the error in their C_1 is almost as large as C_1 itself, due to errors in accounting for the demagnetization of the film.

Volkenshtein measured the temperature dependence of the anomalous Hall conductivity from 4.2 K to 300 K. They found that from about 77 K to 100 K the extraordinary Hall coefficient R_1 shows a linear relationship $R_1 \propto A\rho$ to the resistivity. This shows that skew scattering is likely to dominate the Hall conductivity at lower temperatures in nickel. Lavine measured the Hall resistivity of Ni over a range of temperatures from 77 K to over 600 K. At higher temperatures, $R_1 \propto \rho^{1.97}$, showing that the side-jump and intrinsic mechanisms dominate, but at low temperatures $R_1 \propto \rho^{1.10}$, showing that skew scattering dominates.

Figure 4.6: Plot of the anomalous Hall coefficient R_s in nickel at 297 K. The figures below show the change in R_s, from (4.18), as **M** rotates around the axis **J**, using the parameters in table 4.8.

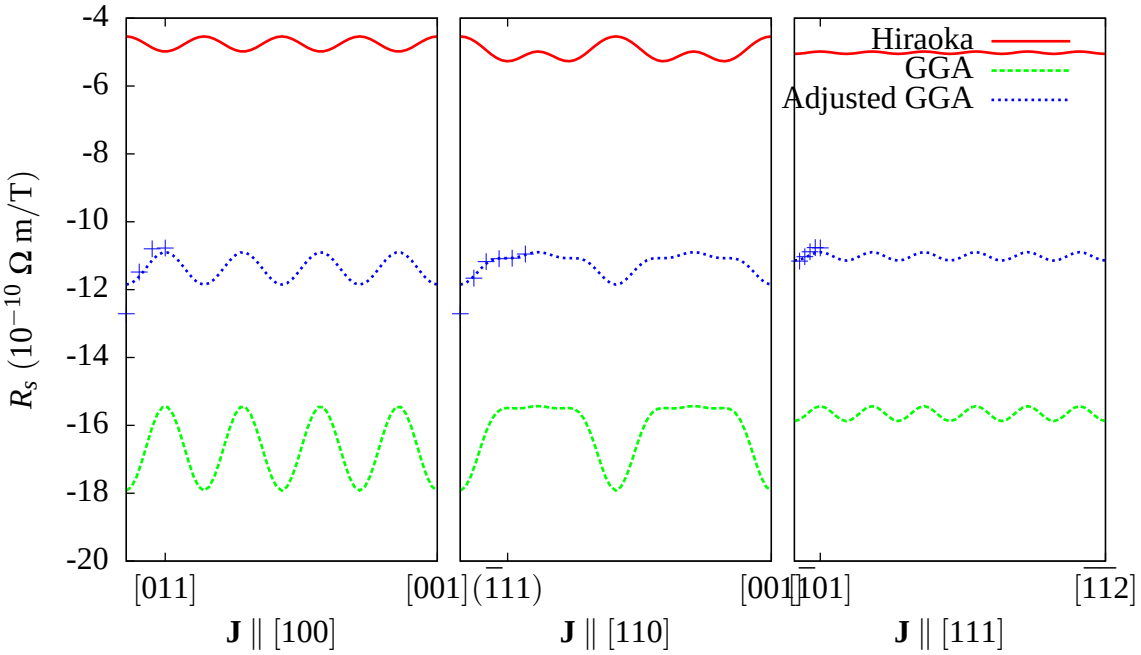

Figure 4.7: Plot of the anomalous Hall coefficient R_s in nickel at 77 K. The figures below show the change in R_s, from (4.18), as **M** rotates around the axis **J**, using the parameters in table 4.9.

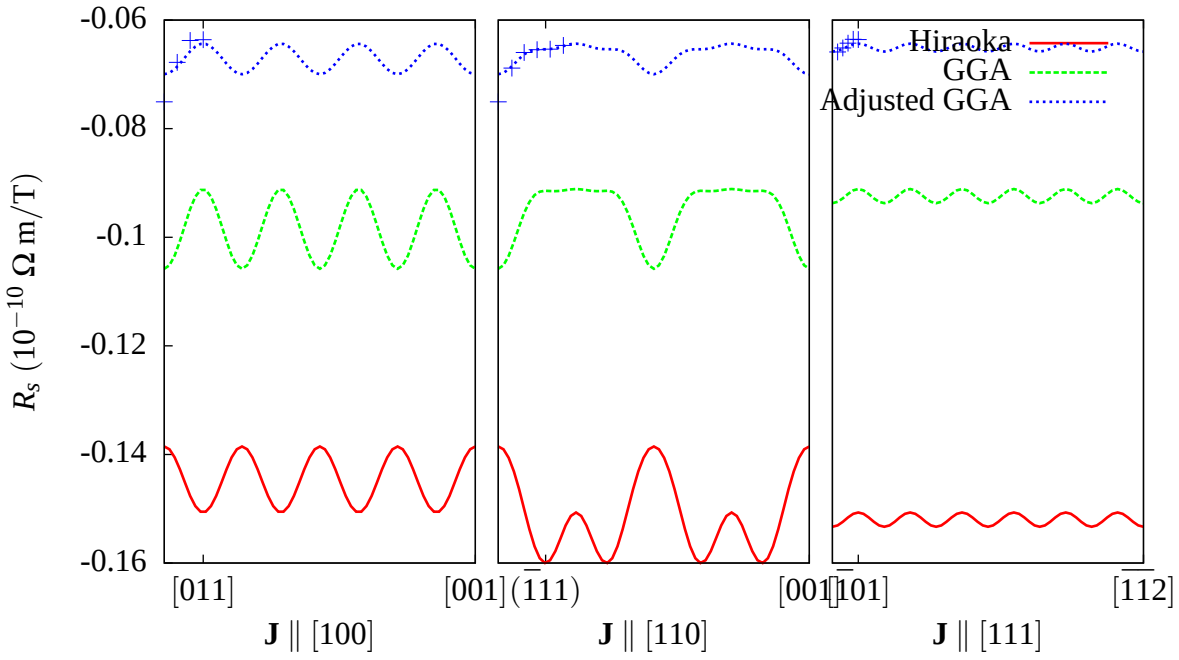

4.6 Conclusions

In this chapter, we have discussed the anomalous Hall conductivity in Ni under a variety of conditions. First, we discussed the known limitations of the GGA in describing Ni. We introduced a modification to the Wannier interpolation Hamiltonian to reduce the exchange splitting of the *d*-bands. We showed that this adjustment brings the electronic structure closer to what is observed experimentally, and described how adjusting the exchange splitting affects the anomalous Hall conductivity. We found that our exchange splitting adjustment corrects half of the discrepancy between the experimental R_s and the intrinsic contribution to R_s. We also discussed the temperature dependence of the intrinsic conductivity, and showed that the change in the conductivity, though only about 10%, should be large enough to be observable. In the final section of the chapter we discussed the orientation dependence of the anomalous Hall conductivity and compared with the available experimental data for Ni.

The calculations here agree with the measurements of Hiraoka, in that we predict a large anisotropy in the Hall conductivity of Ni, but disagree in some important ways. First, the Hall conductivity predicted here is again too large. Second, our calculations predict the wrong sign for the third-order anisotropy of nickel, but improvements to the band structure calculations could alter the third-order anisotropy. The *d*-band width in our calculations is too large, but as we argued earlier, although we don't expect this to make a significant difference in the conductivity. A more robust calculation could be made by using a self-consistent Hamiltonian to calculate the band structure. Such a self-consistent calculation could have a significant effect on the structure of the *d*-bands. Another method method that has shown promise in describing Ni is the LDA+U method. LDA+U has been used to calculate the magnetic anisotropy of nickel, and the predicted magnetic anisotropy energy agreed with experimental measurements of the easy axis of Ni [73]. Similar calculations may improve our ability to describe the Hall conductivity.

The most significant limitation, though, in the data described here is that we cannot evaluate either the side-jump or skew scattering contributions to the Hall resistivity. It is entirely possible that the skew scattering contribution to Ni is large and anisotropic. Figure 4.7 shows that the intrinsic mechanism is too small to account for the observed Hall resistivity at 77 K. At 77 K, Volkenshtein showed that the is dominated by skew scattering. This is significant, since at room temperature, we saw that the intrinsic contribution to the resistivity was too large. We can use this estimate of the intrinsic conductivity as an upper bound. If we ignore side-jump scattering, then we can attribute the discrepancy between the calculated intrinsic Hall resistivity and the observed Hall resistivity to skew scattering. We can then conclude that the skew scattering is anisotropic, and that $C_1 < 0$ for skew scattering.

Chapter 5

Conclusion

This work shows that the anomalous Hall conductivity in iron, cobalt, and nickel, over all orientations of the magnetization, is adequately described by the Karplus-Luttinger theory, when used with an *ab initio* calculation of the electronic structure. In cobalt, these calculations show that the observed Hall conductivity in polycrystalline thin films can be explained by taking into account the first-order anisotropy of the magnetization. In iron, anisotropy appears to third-order in the magnetization, but the magnitude of the third-order term is too small to have been measured by past experiments. For nickel, in addition to describing the anisotropy, we also showed that half of the discrepancy between previous *ab initio* calculations and the measured anomalous Hall coefficient can be eliminated by adjusting the theoretical exchange splitting of nickel to estimates of the experimental exchange splitting. Using this same adjustment, we calculated the third-order orientation dependence of the intrinsic anomalous Hall conductivity, and showed that the third-order intrinsic term does not explain the experimentally observed anisotropy in nickel. We speculated that this discrepancy is a result of skew-scattering from the low temperature measurements of nickel, where skew-scattering is expected to dominate the anomalous Hall effect.

The motivation for this work came from several areas. First and foremost is the desire to understand the microscopic mechanisms of the anomalous Hall effect. The intrinsic Karplus-Luttinger mechanism is only one of the contributions to the anomalous Hall conductivity. Calculations of this contribution from first principles, combined with measurements of the Hall coefficients, allow us to estimate the size of the side-jump and skew coefficients. Second, the intrinsic conductivity is a macroscopic manifestation of a geometric property, the Berry curvature, of the electron band structure. The geometric effects are sensitive to the fine details of the electronic structure, so early efforts were hampered due to the lack of sufficient accuracy in the wave functions. Studying the anomalous Hall conductivity from first principles, using accurate Hamiltonians, allows us to gain insight as to how these effects behave in realistic systems, and serve as a complement to model Hamiltonians using simplified descriptions of these materials. A final goal of this work is to serve as a starting point for future studies of the anomalous Hall conductivity as the mag-

netization changes orientation. The magnetic field orientation is one of the few parameters that can be easily adjusted by both experiments and in theoretical calculations. Therefore, this work is expected to be of interest to future theorists calculating the side-jump and skew scattering contributions, and also to experimentalists studying anisotropic transport.

5.1 Future Work

The calculations of the AHC anisotropy of nickel failed to explain the third-order anisotropy. Although the error could be a remaining problem in the electronic structure, the discrepancy could also be due to skew scattering at room temperature. A self-consistent calculation of the band structure of nickel, using a modern treatment of the exchange and correlation energies, can clarify the possible errors in the band structure. A calculation should be performed using one of the methods that has been shown to agree with the magnetic anisotropy energy calculations of nickel. The most direct step in this direction is an LDA+U calculation of nickel using spinor wave functions.

These intrinsic calculations of the conductivity are only the first step towards a complete *ab initio* treatment of the anomalous Hall effect. The side-jump and skew scattering terms remain important in some regimes, and no practical scheme has yet emerged for calculating these terms. The results for nickel presented in this work show that the anisotropy of the Hall conductivity in nickel is a promising starting point for future insight into the role of these mechanisms, in particular the skew scattering. At higher temperatures, the intrinsic effect should dominate the Hall coefficient of nickel. Therefore, a measurement of the AHE anisotropy at higher temperatures may reveal that the third-order anisotropy changes sign as the temperature increases.

Our estimates for polycrystalline samples of cobalt showed agreement with the existing measurements, but we used a relatively crude approximation to model the polycrystalline behavior. Better models of polycrystalline samples are required to connect the conductivity calculations presented here with measurements of the anomalous Hall effect in polycrystalline samples.

In our comparison with Hiraoka's measurements of nickel [19], and Tatsumoto and Okamoto's measurements of iron [56], we note here that these researchers also measured the pressure and strain dependence of the anomalous Hall coefficients in these materials. Simulations of the pressure and strain dependence could be useful to supplement the orientation dependence described here.

Bibliography

[1] N. Nagaosa, J. Sinova, S. Onoda, A. H. MacDonald, and N. P. Ong, Anomalous Hall effect, arXiv:0904.4154v1, 2009.

[2] E. H. Hall, Amer. J. Math **2**, 287 (1879).

[3] E. H. Hall, Phil. Mag. **12**, 157 (1881).

[4] R. Karplus and J. M. Luttinger, Phys. Rev. **95**, 1154 (1954).

[5] Y. Yao, L. Kleinman, A. H. MacDonald, J. Sinova, T. Jungwirth, D.-s. Wang, E. Wang, and Q. Niu, Phys. Rev. Lett. **92**, 037204 (2004).

[6] X. Wang, J. R. Yates, I. Souza, and D. Vanderbilt, Phys. Rev. B **74**, 195118 (2006).

[7] X. Wang, D. Vanderbilt, J. R. Yates, and I. Souza, Phys. Rev. B **76**, 195109 (2007).

[8] Z. Fang, N. Nagaosa, K. S. Takahashi, A. Asamitsu, R. Mathieu, T. Ogasawara, H. Yamada, M. Kawasaki, Y. Tokura, and K. Terakura, Science **302**, 92 (2003).

[9] C. Zeng, Y. Yao, Q. Niu, and H. H. Weitering, Phys. Rev. Lett. **96**, 037204 (2006).

[10] J. Kötzler and W. Gil, Phys. Rev. B **72**, 060412 (2005).

[11] Y. Tian, L. Ye, and X. Jin, Phys. Rev. Lett. **103**, 087206 (2009).

[12] N. A. Sinitsyn, Journal of Physics: Condensed Matter **20**, 023201 (2008).

[13] C. M. Hurd, *The Hall Effect in Metals and Alloys* (Plenum Press, New York, 1972).

[14] R. R. Birss, *Symmetry and Magnetism* (North-Holland Publishing Company, Amsterdam, 1964).

[15] C. M. Hurd, Adv. Phys. **23**, 315 (1974).

[16] A. P. Cracknell, Adv. Phys. **23**, 673 (1974).

[17] M. J. Lax, *Symmetry Principles in Solid State and Molecular Physics* (Wiley, New York, 1974).

[18] N. R. Draper and H. Smith, *Applied Regression Analysis*, 3rd ed. (Wiley, New York, 1998).

[19] T. Hiraoka, J. Sci. Hiroshima Univ. **32**, 153 (1968).

[20] L. Berger, Phys. Rev. B **2**, 4559 (1970).

[21] J. Smit, Physica **21**, 877 (1955).

[22] J. Smit, Physica **24**, 39 (1958).

[23] V. V. Volkenshtein and G. V. Fedorov, JETP **11**, 48 (1960).

[24] N. V. Volkenshtein, G. V. Fedorov, and V. P. Shirokovskii, Phys. Met. Metallogr **11**, 151 (1961).

[25] C. Kittel, Introduction to Solid State Physics, 1995.

[26] E. I. Blount, in *Solid State Physics*, edited by F. Seitz and D. Turnbull (Academic Press, New York, 1972), Vol. 27, p. 1.

[27] A. Bohm, A. Mostafazadeh, H. Koizumi, Q. Niu, and J. Zwanziger, *The Geometric Phase in Quantum Systems* (Springer, New York, 2003).

[28] L. Hodges, D. R. Stone, and A. V. Gold, Phys. Rev. Lett. **19**, 655 (1967).

[29] J. Kohanoff, *Electronic Structure Calculations for Solids and Molecules* (Cambridge University Press, Cambridge, 2006).

[30] L. Kleinman, Phys. Rev. B **21**, 2630 (1980).

[31] N. W. Ashcroft and N. D. Mermin, *Solid State Physics* (Brooks Cole, New York, 1976).

[32] E. Roman, Y. Mokrousov, and I. Souza, Phys. Rev. Lett. **103**, 097203 (2009).

[33] R. S. Lee and S. Legvold, Phys. Rev. **162**, 431 (1967).

[34] A. A. Hirsch and Y. Weissman, Physics Letters A **44**, 239 (1973).

[35] K. Ohgushi, S. Miyasaka, and Y. Tokura, Journal of the Physical Society of Japan **75**, 013710 (2006).

[36] B. C. Sales, R. Jin, and D. Mandrus, Phys. Rev. B **77**, 024409 (2008).

[37] J. Stankiewicz and K. P. Skokov, Phys. Rev. B **78**, 214435 (2008).

[38] H. Masumoto, H. Saitô, and M. Kikuchi, Sci. Rep Res. Inst. Tohoku Univ. Phys. Chem. Metall. **18**, 84 (1966).

[39] P. Giannozzi, S. Baroni, N. Bonini, M. Calandra, R. Car, C. Cavazzoni, D. Ceresoli, G. L. Chiarotti, M. Cococcioni, I. Dabo, A. D. Corso, S. de Gironcoli, S. Fabris, G. Fratesi, R. Gebauer, U. Gerstmann, C. Gougoussis, A. Kokalj, M. Lazzeri, L. Martin-Samos, N. Marzari, F. Mauri, R. Mazzarello, S. Paolini, A. Pasquarello, L. Paulatto, C. Sbraccia, S. Scandolo, G. Sclauzero, A. P. Seitsonen, A. Smogunov, P. Umari, and R. M. Wentzcovitch, Journal of Physics: Condensed Matter **21**, 395502 (2009).

[40] J. P. Perdew, K. Burke, and M. Ernzerhof, Phys. Rev. Lett. **77**, 3865 (1996).

[41] H. Monkhorst and J. Pack, Phys. Rev. B **13**, 5188 (1976).

[42] N. Marzari, D. Vanderbilt, A. De Vita, and M. C. Payne, Phys. Rev. Lett. **82**, 3296 (1999).

[43] N. Marzari and D. Vanderbilt, Phys. Rev. B **56**, 12847 (1997).

[44] I. Souza, N. Marzari, and D. Vanderbilt, Phys. Rev. B **65**, 035109 (2001).

[45] A. A. Mostofi, J. R. Yates, Y.-S. Lee, I. Souza, D. Vanderbilt, and N. Marzari, Computer Physics Communications **178**, 685 (2008).

[46] J. R. Yates, X. Wang, D. Vanderbilt, and I. Souza, Phys. Rev. B **75**, 195121 (2007).

[47] C. Zener, Phys. Rev. **96**, 1335 (1954).

[48] H. Callen and E. Callen, Journal of Physics and Chemistry of Solids **27**, 1271 (1966).

[49] D. Weller, G. R. Harp, R. F. C. Farrow, A. Cebollada, and J. Sticht, Phys. Rev. Lett. **72**, 2097 (1994).

[50] J. Trygg, B. Johansson, O. Eriksson, and J. M. Wills, Phys. Rev. Lett. **75**, 2871 (1995).

[51] D. Ceresoli, U. Gerstmann, A. P. Seitsonen, and F. Mauri, Phys. Rev. B **81**, 060409 (2010).

[52] I. Souza and D. Vanderbilt, Phys. Rev. B **77**, 054438 (2008).

[53] F. D. M. Haldane, Phys. Rev. Lett. **93**, 206602 (2004).

[54] I. A. Tsoukalas, Physica Status Solidi (a) **23**, K41 (1974).

[55] W. L. Webster, Proc. Cambridge Phil. Soc. **23**, 800 (1927).

[56] E. Tatsumoto and T. Okamoto, J. Phys. Soc. Japan **14**, 226 (1959).

[57] C. Kooi, Phys. Rev. **95**, 843 (1954).

[58] R. W. Klaffky and R. V. Coleman, Phys. Rev. B **10**, 2915 (1974).

[59] T. Okamoto, J. Sci. Hiroshima Univ. **26**, 11 (1962).

[60] P. N. Dheer, Phys. Rev. **156**, 637 (1967).

[61] J. M. Lavine, Phys. Rev. **123**, 1273 (1961).

[62] F. J. Himpsel, J. A. Knapp, and D. E. Eastman, Phys. Rev. B **19**, 2919 (1979).

[63] R. Gersdorf, Phys. Rev. Lett. **40**, 344 (1978).

[64] N. Kamakura, Y. Takata, T. Tokushima, Y. Harada, A. Chainani, K. Kobayashi, and S. Shin, Phys. Rev. B **74**, 045127 (2006).

[65] A. Liebsch, Phys. Rev. Lett. **43**, 1431 (1979).

[66] F. Weling and J. Callaway, Phys. Rev. B **26**, 710 (1982).

[67] K. J. Kim, T. C. Leung, B. N. Harmon, and D. W. Lynch, Journal of Physics: Condensed Matter **6**, 5069 (1994).

[68] J. Bünemann, F. Gebhard, T. Ohm, S. Weiser, and W. Weber, Phys. Rev. Lett. **101**, 236404 (2008).

[69] J. R. Driscoll and D. M. Healy, Advances in Applied Mathematics **15**, 202 (1994).

[70] in *Springer Materials - The Landolt-Börnstein Database*, edited by K.-H. Hellwege and J. L. Olsen (Springer-Verlag, Berlin, 1982), Vol. 15a: Electrical Resistivity, Kondo and Spin Fluctuation Systems, Spin Glasses and Thermopower, p. 92.

[71] G. Thomas and V. A. Marsocci, Journal of Applied Physics **40**, 2462 (1969).

[72] T. T. Chen and V. A. Marsocci, Physica **59**, 498 (1972).

[73] I. Yang, S. Y. Savrasov, and G. Kotliar, Phys. Rev. Lett. **87**, 216405 (2001).

[74] R. Jaggi and F. Hulliger, in *Zahlenwerte und Funktionen*, edited by Landolt-Börnstein (Springer-Verlag, Berlin, 1959), Vol. 2, part 6(1), p. 205, galvanomagnetic and Thermognetic Transverse Effects.

[75] W. H. Kleiner, Phys. Rev. **142**, 318 (1966).

[76] H. J. Juretschke, Acta Crystallographica **5**, 148 (1952).

[77] F. G. Fumi, Acta Cryst. **5**, 44 (1952).

[78] H. J. Juretschke, Acta Crystallographica **8**, 716 (1955).

[79] F. G. Fumi, Nuovo Cimento **9**, 739 (1952).

[80] R. Fieschi and F. G. Fumi, Nuovo Cimento **10**, 865 (1953).

[81] F. G. Fumi and C. Ripamonti, Acta Crystallographica Section A **36**, 535 (1980).

[82] F. G. Fumi and C. Ripamonti, Acta Crystallographica Section A **36**, 551 (1980).

[83] F. G. Fumi and C. Ripamonti, Acta Crystallographica Section A **39**, 245 (1983).

[84] T. H. Cormen, C. E. Leiserson, R. L. Rivest, and C. Stein, *Introduction to Algorithms*, 2nd ed. (MIT Press, Cambridge, MA, 2001).

[85] G. B. Arfken and H. J. Weber, *Mathematical Methods for Physicists*, sixth ed. (Elsevier, Amsterdam, 2005).

Appendix A

Units

In the magnetism literature the saturation magnetization M_s is rarely listed in units of emu/cm^3, but is usually expressed in the cgs unit of magnetic flux density G. To convert into SI units,

$$M = \frac{B}{\mu_0} = \frac{4\pi}{\mu_0}\frac{B}{4\pi} \tag{A.1}$$

where $B/(4\pi)$ is the cgs magnetization in G, and M is in A/m, and $4\pi/\mu_0 = 10^3$A/m/G.

A.1 Units and Conventions

Resistivity is measured in s^{-1} in Gaussian units, but in the older Hall effect literature it is common to use the SI unit of resistivity, and Gaussian units for the magnetic quantities B, H, and M, so the ordinary Hall coefficient R_0 is in units of Ω cm/G. We may convert both R_0 and R_s into SI units in the usual manner (1 Ωcm/G $= 10^2$ Ωm/T), but we must take some care when with the extraordinary Hall coefficient R_1.

We defined R_1 through the relationship (1.5). If we substitute H for $\mu_0 H$ and $4\pi M$ for $\mu_0 M$, we find

$$\rho_H = R_0 H + R_1 4\pi M. \tag{A.2}$$

In the older literature, we find instead of (A.2) the convention $\rho_H = R_0 H + R_1 M$, so if we now define

$$R_1^\star = 4\pi R_1 \tag{A.3}$$

then

$$\rho_H = R_0 H + R_1^\star M. \tag{A.4}$$

These relationships are summarized in table A.1 When comparing the results presented here with older work, R_0 and R_s should agree, but the reader must check to see whether relationship (A.4) (e.g. [19], [34]) or (A.2) (e.g. [74], [13]) has been used. Hurd [13] defines R_1 with relationship (A.4) in chapter 5, but uses the definition (A.2) in the tables at the end of the book!

Table A.1: Relationships between cgs and SI definitions of quantities related to the anomalous Hall conductivity

symbol	name	SI	cgs
B	magnetic flux density	$\mu_0(H+M)$	$H+4\pi M$
H	magnetic field strength	$\mu_0 H$	H
M	magnetization	$\mu_0 M$	$4\pi M$
ρ_H	Hall resistivity	$R_0\mu_0 H + R_1\mu_0 M$	$R_0 H + R_1^\star M$
ρ_H	Hall resistivity	$R_0 B + R_1\mu_0 M$	$R_0 B + 4\pi R_s M$
R_1	extraordinary Hall coefficient	$R_1 = R_0 + R_s$	$R_1^\star = 4\pi(R_0 + R_s)$
R_s	anomalous Hall coefficient	$R_s = R_1 + R_0$	$R_s = R_1^\star/(4\pi) - R_0$

$$1\ \Omega\ \text{m/T} = 10^{-2}\ \Omega\ \text{cm/G} \tag{A.5}$$

$$1\ \Omega\ \text{cm/G} = 100\ \Omega\ \text{m/T} \tag{A.6}$$

A.2 Applied Fields

In this section we express the Hall resistivity in terms of the applied field H_a, rather than the internal field H. The two fields are related by the expression

$$H = H_a - NM \tag{A.7}$$

where N is the demagnetization factor of the sample. Since $M = (\mu_r - 1)H$, the internal field is related to the applied field by

$$H = \frac{H_a}{1 + N(\mu_r - 1)} \tag{A.8}$$

and we have

$$\rho_H = R_0\mu_0 H_a + (R_1 - NR_0)\,\mu_0 M. \tag{A.9}$$

For large applied fields, $M = M_s$, so that

$$\rho_H = R_0\mu_0 H_a + (R_1 - NR_0)\,\mu_0 M_s. \tag{A.10}$$

To understand what happens in small fields, we first use (A.8) to eliminate M from (A.9) that

$$\rho_H = \frac{R_0 + R_1(\mu_r - 1)}{1 + N(\mu_r - 1)}\mu_0 H_a. \tag{A.11}$$

Since μ_r is large for small applied fields, and $N \approx 1$ for a plate or rod in the usual geometry, (A.11) reduces to

$$\rho_H = \frac{R_1}{N}\mu_0 H_a. \tag{A.12}$$

Comparing relations (A.9), (A.10), and (A.12) with (1.5), (1.8) and (1.9) we see that the qualitative behavior of the Hall resistivity is the same in both cases, i.e. the ordinary Hall coefficient R_0 dominates in large fields. In small fields, we find that $\rho_H = (R_1/N)\mu_0 H_a$, rather than $\rho_H = R_1\mu_0 H$. For an infinite plane, the demagnetization factor $N = 1$ if H_a is normal to the plane, and there is no need to distinguish between $\mu_0 H_a$ from B, since the resulting Hall coefficients are identical. If N is on the order $1/\mu_r$, or $N = 0$, this argument no longer applies. For thin films, when the applied magnetic field is in the plane of the film, a separate analysis is necessary.

Appendix B

Symmetry of the Conductivity Tensor

B.1 Symmetries of the Conductivity Tensor

Birss [14] considers in detail the symmetries governing galvanomagnetic properties, including the anomalous Hall coefficient. The nonvanishing components of the conductivity tensor are determined by the relations:

$$\sigma_{ij\ldots p^m\ldots p^n\ldots} = \sigma_{ij\ldots p^n\ldots p^m\ldots} \tag{B.1}$$

$$\sigma_{ij}(\mathbf{M}) = \sigma_{ji}(-\mathbf{M}) \tag{B.2}$$

$$R\sigma_{ij}(\mathbf{M}) = (\det R)\sigma_{ij}(\mathbf{M}). \tag{B.3}$$

Despite early criticism that these results [75] do not properly account for microscopic reversibility in the presence of a magnetic field, the relationships above were later shown correct [16].

B.2 Direct Inspection Method

To motivate the direct inspection method, we begin with an example. Consider a fourfold rotational symmetry through the z-axis. This symmetry is generated by the operation R taking $x \to y$, $y \to -x$, $z \to z$. The action of R on a tensor of rank 1, i.e. a vector $\mathbf{A} = A_x\hat{x} + A_y\hat{y} + A_z\hat{z}$ shows that $R(\mathbf{A}) = -A_y\hat{x} + A_x\hat{y} + A_z\hat{z}$. The action of R on each component of A is given by $R(A_x) = -A_y$, $R(A_y) = A_x$, and $R(A_z) = A_z$. If $\mathbf{A}$ is invariant under R, then $R(A_i) = A_i$, and we find $A_x = A_y = 0$, while A_z remains free.

The direct inspection method formalizes the argument above, and relates it to the symmetries of tensors of arbitrary order. This method stems from the observation that the contraction of a rank n-tensor over n coordinates is invariant under general orthogonal transformations of those coordinates [76]. The direct inspection can be used to find the nonzero components of a tensor [77, 78, 17]. Direct inspection is applicable when the action of the symmetries on a tensor component can be represented as manipulations of the

indices and sign reversal. Therefore, unless the material contains a six-fold or three-fold axis, direct inspection can be used to determine all of the independent components of a high-order matter tensor. When three-fold or six-fold symmetries are present, one must consider the action of these symmetries separately, and direct inspection may still be used for the remaining symmetries.

Fumi describes the generators of the point groups for the applicable (non-hexagonal) crystal classes, and uses the direct inspection to derive the independent tensor components for some crystal classes [77]. Fumi derives expressions for third and fourth rank tensors in hexagonal crystals, using the general group theory arguments, and direct inspection in [79]. In [80] the authors derive results for general tensors of fifth and sixth rank in all of the crystal systems. Fumi and Ripamonti Later found another method for deriving symmetries of high-order tensors with hexagonal symmetry [81], [82], [83].

Birss discusses the symmetries relevant to magnetic systems in detail, and uses direct inspection applied to analyze the galvanomagnetic tensor for crystals of cubic symmetry (O_h) and hexagonal symmetry. Birss starts from the results for general tensors presented by Fumi, and imposes the additional constraints from the polynomial expansion in the magnetic field, and the generalized Onsager relations. In [78], Juretschke applies the same strategy in the A7 crystal structure, to derive similar results for antimony.

B.3 Implementation of the Direct Inspection Method

The high-order polynomials necessary for the description of the Hall conductivity make manually calculations of the unique nonvanishing components of the n-th order galvanomagnetic tensor both tedious and error prone. For example, the fifth order expansion in $\mathbf{M}$ requires us to apply the symmetry relations above to a seventh rank tensor with $3^7 = 2187$ coefficients. We describe here how to carry out such manipulations on a computer.

The tensor component symmetries are relationships of the form

$$T_{ijk\ldots} = \pm T_{i'j'k'\ldots}. \tag{B.4}$$

Imagine a graph formed by these relationships, where each node represents a component $\pm T_{ijk\ldots}$, and the sign is required to represent a possible change in sign of the component. An edge is drawn whenever two components are related by an equality. The connected nodes of any such graph are then identical, and each connected component represents a unique coefficient. An algorithm for finding the connected components of a graph is described in ref. [84].

Each tensor component $T_{ijk\ldots}$ is represented by a string S. The strings are of the form "$\pm$ $ijk\ldots$", where the length of the string is one more than the rank of the tensor, to accomodate the possible sign change. For each symmetry, the symmetry operation g is applied to the string to generate a new string S', and the new string S' is placed into the same set as S. The process is repeated over all components S of a given rank. We apply only the generators of the point groups, since the action of the generator over the entire allows us

to avoid needlessly considering products of group elements. Once the symmetries have been applied, the algorithm terminates with a list of connected nodes, and a representative element for each connected subgraph. The final step is to introduce a tensor component 0, and apply the condition that if $T_{ijk\ldots} = -T_{ijk\ldots}$, then $T_{ijk\ldots} = 0$.

At the end of the symmetry calculation, we are left with a pair of representative elements for each nonvanishing tensor component, and a single representative element for all of the vanishing tensor components. Since the nonvanishing terms of the polynomial expansion of σ_i (the $a_{ij\ldots}$) are now known, it is a simple matter to construct polynomials in α_i appearing in (1.11). Once the polynomials in α_i are known, the final step in the procedure is to express these polynomials in polar coordinates θ and ϕ.

B.4 Spherical Harmonics

The spherical harmonics are a convenient basis set for evaluating the orientation dependence of the Hall conductivity. The normalization and phase conventions for the spherical harmonics are described in this section. The definitions provided here are consistent with those of ref. [85]. The spherical harmonics, Y_l^m, in the Condon-Shortley phase convention, may be written as

$$Y_l^m(\theta,\phi) = \sqrt{\frac{2l+1}{4\pi}\frac{(l-m)!}{(l+m)!}} P_l^m(\cos\theta) e^{im\phi}, \tag{B.5}$$

where the Legendre polynomials, P_l^m are defined for $m >= 0$ by: [85]

$$P_l^m(x) = \frac{(-1)^m}{2^l l!}(1-x^2)^{m/2}\frac{d^{l+m}}{dx^{l+m}}(x^2-1)^l, \tag{B.6}$$

and for $m < 0$

$$P_l^{-m}(x) = (-1)^m \frac{(l-m)!}{(l+m)!} P_l^m(x). \tag{B.7}$$

We may expand a function over the sphere in terms of the Y_l^m

$$f(\theta,\phi) = \sum_{l=0}^{\infty}\sum_{m=-l}^{l} a_l^m Y_l^m(\theta,\phi), \tag{B.8}$$

where

$$a_l^m = \int_0^{2\pi}\int_0^{\pi} Y_l^m(l,m,\theta,\phi)^* f(\theta,\phi)\sin\theta\, d\theta\, d\phi. \tag{B.9}$$

The integral in (B.9) may be performed directly on the polynomial expansion (1.11) to relate the

B.5 Real Spherical Harmonics

We define the real spherical harmonics:

$$C_l^m(\theta,\phi) = \frac{1}{\sqrt{2}}\left[(Y_l^{-m}(\theta,\phi) + (-1)^m Y_l^m(\theta,\phi)\right] = (-1)^m\sqrt{2}\,\mathrm{Re}\,Y_l^m(\theta,\phi) \tag{B.10}$$

$$S_l^m(\theta,\phi) = \frac{i}{\sqrt{2}}\left[Y_l^{-m}(\theta,\phi) - (-1)^m Y_l^m(\theta,\phi)\right] = (-1)^m\sqrt{2}\,\mathrm{Im}\,Y_l^m(\theta,\phi), \tag{B.11}$$

where we have used the identity

$$Y_l^{-m}(\theta,\phi) = (-1)^m Y_l^m(\theta,\phi)^*. \tag{B.12}$$

In terms of the real spherical harmonics, the expansion (B.8) becomes

$$f(\theta,\phi) = \sum_{l=0}^{\infty}\sum_{m=0}^{l}\left[A_l^m C_l^m(\theta,\phi) + B_l^m S_l^m(\theta,\phi)\right]. \tag{B.13}$$

It is sometimes convenient to reorder the summation over l and m to isolate the angular dependence on ϕ:

$$f(\theta,\phi) = \sum_{m=0}^{\infty}\sum_{l=m}^{\infty}\left[A_l^m C_l^m(\theta,\phi) + B_l^m S_l^m(\theta,\phi)\right]. \tag{B.14}$$

The coefficients A_l^m and B_l^m are related to the a_l^m by

$$a_l^0 = \sqrt{2}A_l^0 \tag{B.15}$$

$$a_l^m = \frac{(-1)^m}{\sqrt{2}}\left[A_l^m - iB_l^m\right] \tag{B.16}$$

$$a_l^{-m} = \frac{1}{\sqrt{2}}\left[A_l^m + iB_l^m\right] \tag{B.17}$$

If the function $f(\theta,\phi)$ is real, then the coefficients A_l^m and B_l^m are also real. Then we may write for $m > 0$

$$A_l^m = \sqrt{2}\,\mathrm{Re}\,a_l^{-m} \tag{B.18}$$

$$B_l^m = \sqrt{2}\,\mathrm{Im}\,a_l^{-m} \tag{B.19}$$

and for $m = 0$

$$A_l^0 = \frac{a_l^0}{\sqrt{2}}. \tag{B.20}$$

B.6 Cubic Crystals

We begin by discussing crystals in the crystal class O_h. This class of crystals include the face-centered cubic and body-centered cubic systems.

B.6.1 Third-order relations

In a cubic crystal, we find that:

$$\sigma_{23} = a_{123}\alpha_1 + 3a_{12223}(\alpha_1\alpha_2^2 + \alpha_1\alpha_3^2) + a_{12333}\alpha_1^3 \tag{B.21}$$
$$\sigma_{31} = a_{123}\alpha_2 + 3a_{12223}(\alpha_2\alpha_1^2 + \alpha_2\alpha_3^2) + a_{12333}\alpha_2^3 \tag{B.22}$$
$$\sigma_{12} = a_{123}\alpha_3 + 3a_{12223}(\alpha_3\alpha_1^2 + \alpha_3\alpha_2^2) + a_{12333}\alpha_3^3 \tag{B.23}$$

There is one independent 3rd-order component: a_{123} and two independent 5th-order components: a_{12223} and a_{12333}.

$$\sigma_{23} = A_1^1 C_1^1(\theta,\phi) + A_3^1 C_3^1(\theta,\phi) + A_3^3 C_3^3(\theta,\phi) \tag{B.24}$$
$$\sigma_{31} = B_1^1 S_1^1(\theta,\phi) + B_3^1 S_3^1(\theta,\phi) + B_3^3 S_3^3(\theta,\phi) \tag{B.25}$$
$$\sigma_{12} = A_1^0 C_1^0(\theta,\phi) + A_3^0 C_3^0(\theta,\phi) \tag{B.26}$$

Relating the spherical harmonic coefficients back to the Cartesian tensor coefficients we find that

$$A_1^1 = 1/15\sqrt{12\pi}(5a_{123} + 6a_{12223} + 3a_{12333}) \tag{B.27}$$
$$A_3^1 = 1/35\sqrt{42\pi}(3a_{12223} - a_{12333}) \tag{B.28}$$
$$A_3^3 = -\sqrt{2\pi/35}(3a_{12223} - a_{12333}) = -\sqrt{5/3}A_3^1, \tag{B.29}$$

$$B_1^1 = 1/15\sqrt{6}\sqrt{2\pi}(3a_{12333} + 5a_{123} + 6a_{12223}) = A_1^1 \tag{B.30}$$
$$B_3^1 = 1/35\sqrt{42\pi}(3a_{12223} - a_{12333}) = A_3^1 \tag{B.31}$$
$$B_3^3 = \sqrt{2\pi/35}(3a_{12223} - a_{12333}) = -A_3^3, \tag{B.32}$$

and finally

$$A_1^0 = 1/15\ \sqrt{6\pi}(6a_{12223} + 3a_{12333} + 5a_{123}) = (1/2)\sqrt{2}A_1^1 \tag{B.33}$$
$$A_3^0 = -\tfrac{2}{35}\sqrt{14\pi}(3a_{12223} - a_{12333}) = -(2/3)\sqrt{3}A_3^1. \tag{B.34}$$

There are two linearly independent spherical harmonic coefficients: A_3^1 and A_1^1.

B.6.2 Fifth-order relations

Hiraoka [19] expands the resistivity tensor to fifth order in α, starting with the relationship

$$A_i(\alpha) = \alpha_i\left[e + e_1\alpha_i^2 + e_2\alpha_i^4 + e_3\left(\alpha_1^2\alpha_2^2 + \alpha_2^2\alpha_3^2 + \alpha_3^2\alpha_1^2\right)\right]. \tag{B.35}$$

Since this expansion applies to the conductivity tensor, we may use it directly. In terms of spherical harmonics, this relationship becomes:

$$\sigma_{23} = A_1^1 C_1^1(\theta,\phi) + A_3^1 C_3^1(\theta,\phi) + A_3^3 C_3^3(\theta,\phi) + A_5^1 C_5^1(\theta,\phi) + A_5^3 C_3^3(\theta,\phi) + A_5^5 C_5^5(\theta,\phi) \tag{B.36}$$

$$\sigma_{31} = B_1^1 S_1^1(\theta,\phi) + B_3^1 S_3^1(\theta,\phi) + B_3^3 S_3^3(\theta,\phi) + B_5^1 S_5^1(\theta,\phi) + B_5^3 S_3^3(\theta,\phi) + B_5^5 S_5^5(\theta,\phi) \tag{B.37}$$

$$\sigma_{12} = A_1^0 C_1^0(\theta,\phi) + A_3^0 C_3^0(\theta,\phi) + A_5^0 C_5^0(\theta,\phi) + A_5^4 C_5^4(\theta,\phi) \tag{B.38}$$

where the B_l^m and A_l^m are related by

$$B_1^1 = A_1^1 \tag{B.39}$$
$$B_3^1 = A_3^1 \tag{B.40}$$
$$B_3^3 = -A_3^3 \tag{B.41}$$
$$B_5^1 = A_5^1 \tag{B.42}$$
$$B_5^3 = -A_5^3 \tag{B.43}$$
$$B_5^4 = A_5^4 \tag{B.44}$$

Hiraoka does not use the coefficients e, e_1, e_2, and e_3 directly, but instead defines three coefficients

$$C = e + e_1 + e_2 \tag{B.45}$$
$$C_1 = -2e_1 - 3e_2 + e_3 \tag{B.46}$$
$$C_2 = 3e_2. \tag{B.47}$$

Aside from an overall constant of proportionality relating C, C_1 and C_2 to the conductivities, these coefficients are given in terms of the A_l^m by the relations:

$$C = \sqrt{\frac{1}{2\pi}}\left(\sqrt{3}A_1^0 + \sqrt{7}A_3^0 + \sqrt{11}A_5^0\right) \tag{B.48}$$
$$C_1 = -\frac{1}{16\sqrt{\pi}}\left(40\sqrt{14}A_3^0 + 49\sqrt{22}A_5^0 - 3\sqrt{385}A_5^4\right) \tag{B.49}$$
$$C_2 = \frac{63}{16}\sqrt{\frac{11}{\pi}}\left(3\sqrt{2}A_5^0 - \sqrt{35}A_5^4\right). \tag{B.50}$$

B.7 Tetragonal Crystals

In this section we discuss the symmetries of the conductivity in crystals with the point group D_{4h}. These systems include the face-centered tetragonal, body-centered tetragonal, and A3 crystal structures. To third order in the magnetic field direction, the AHC tensor in these crystals may be written as:

$$\sigma_{23} = a_{231}\alpha_1 + 3a_{23133}\alpha_1\alpha_3^2 + 3a_{23122}\alpha_1\alpha_2^2 + a_{23111}\alpha_1^3 \tag{B.51}$$
$$\sigma_{31} = a_{231}\alpha_2 + 3a_{23133}\alpha_2\alpha_3^2 + 3a_{23122}\alpha_2\alpha_1^2 + a_{23111}\alpha_2^3 \tag{B.52}$$
$$\sigma_{12} = a_{123}\alpha_3 + 3a_{12223}(\alpha_1^2\alpha_3 + \alpha_2^2\alpha_3) + a_{12333}\alpha_3^3. \tag{B.53}$$

There are 2 unique 3rd-order components a_{312} and a_{123} and 5 unique 5th-order components: a_{23111}, a_{23122}, a_{23133}, a_{12311} and a_{12333}.

If we express the relations above in terms of the (real) spherical harmonics, we find that these equations can be written in terms of the C_l^m and S_l^m:

$$\sigma_{23} = A_1^1 C_1^1(\theta,\phi) + A_3^1 C_3^1(\theta,\phi) + A_3^3 C_3^3(\theta,\phi) \quad \text{(B.54)}$$

$$\sigma_{31} = B_1^1 S_1^1(\theta,\phi) + B_3^1 S_3^1(\theta,\phi) + B_3^3 S_3^3(\theta,\phi) \quad \text{(B.55)}$$

$$\sigma_{12} = A_1^0 C_1^0(\theta,\phi) + A_3^0 C_3^0(\theta,\phi). \quad \text{(B.56)}$$

We can relate the coefficients of the spherical harmonic expansion to the components of the tensor a. Transforming σ_{23}, we find

$$A_1^1 = \tfrac{\sqrt{12\pi}}{15}(5a_{231} + 3a_{23111} + 3a_{23122} + 3a_{23133}) \quad \text{(B.57)}$$

$$A_3^1 = \tfrac{\sqrt{42\pi}}{35}(4a_{23133} - a_{23122} - a_{23111}) \quad \text{(B.58)}$$

$$A_3^3 = -\sqrt{2\pi/35}\,(3a_{23122} - a_{23111}). \quad \text{(B.59)}$$

Similarly for σ_{31},

$$B_1^1 = \tfrac{\sqrt{12\pi}}{15}(5a_{231} + 3a_{23111} + 3a_{23122} + 3a_{23133}) = A_1^1 \quad \text{(B.60)}$$

$$B_3^1 = \tfrac{\sqrt{42\pi}}{35}(4a_{23133} - a_{23122} - a_{23111}) = A_3^1 \quad \text{(B.61)}$$

$$B_3^3 = \sqrt{2\pi/35}\,(3a_{23122} - a_{23111}) = -A_3^3, \quad \text{(B.62)}$$

and finally for σ_{12}

$$A_1^0 = \frac{\sqrt{6\pi}}{15}(5a_{123} + 6a_{12223} + 3a_{12333}) \quad \text{(B.63)}$$

$$A_3^0 = -\frac{4}{35}\sqrt{7\pi/2}\,(3a_{12223} - a_{12333}). \quad \text{(B.64)}$$

There are 7 independent Cartesian coefficients, but only 5 independent spherical harmonic coefficients: A_1^1, A_3^1, A_3^3, A_1^0 and A_3^0. The spherical harmonics provide all of the information that is independent of the field magnitude. If we compare the results for cubic crystals with those of tetragonal crystals, we find that in the tetragonal crystals, A_3^1 and A_3^3 are independent, but they are related in the cubic systems. Similar relationships are seen in (B.34) and (B.33). See section 2.1 for a related discussion of hcp crystals.